Spectroscopic and Kinetic Studies of Histidine-Methionine containing Copper Enzymes and Proteins

by

Katherine Brannen Alwan, M.S.

A DISSERTATION

Presented to the Oregon Health & Science University
School of Medicine
in partial fulfillment of the requirements for the degree of

Doctor of Philosophy

October 2020

CERTIFICATE OF APPROVAL

This is to certify that the PhD dissertation of

Katherine Brannen Alwan, M.S.

has been approved by

Ninian Blackburn, PhD, Advisor

Pierre Moënne-Loccoz, PhD, Chair

Kelly Chacón, PhD, member

Francis Valiyaveetil, PhD, member

Martina Ralle, PhD, member

Table of Contents

Acknowledgements

I would like first to acknowledge and thank my research advisor, Professor Ninian J. Blackburn, for allowing me to be an independent scientist while providing constant support, advice, and opportunities during my graduate studies. Above all, thank you for sharing your expertise of and love for the beamline. I am grateful to have you as a lifelong mentor. I would also like to thank my committee members, Professors Pierre Moënne-Loccoz, Kelly Chacón, Francis Valiyaveetil, and Martina Ralle for guiding my research goals and carefully reviewing my dissertation. I would like to acknowledge my lab mates past and present, especially Evan Welch, Renee Arias, Katie Rush and their dogs Pan, Konrad, and Ferdinand/Derby, respectively, for their friendship and endless support inside and out of the lab. Finally, I wish to thank my family and friends for their constant support. Love knows no distance; pursuing my graduate studies without them would have been impossible.

List of Tables

List of Figures

Abstract

Spectroscopic and Kinetic Studies of Histidine-Methionine containing Copper Enzymes and Proteins

Katherine Brannen Alwan, M.S.

Doctor of Philosophy

Oregon Health & Science University School of Medicine

October, 2020

Thesis Advisor: Ninian J. Blackburn, PhD.

The Blackburn Lab studies biological copper chemistry using biochemical, biophysical, and advanced spectroscopic techniques. Our research aims are two-pronged, which is reflected in this dissertation.

First, we aim to elucidate the mechanism of mononuclear copper monooxygenases, specifically peptidylglycine α-hydroxylating monooxygenase (PHM) and dopamine β-monooxygenase (DβM), both of which catalyze the hydroxylation of high energy C-H bonds utilizing a pair of chemically distinct copper sites (referred to as the M- and H- center) separated by 11 Å. The Blackburn Lab has previously constructed single-site PHM variants that were designed to allow study of the M- and H-centers independently in order to place their reactivity sequentially along the catalytic pathway. However, more recent crystallographic studies suggest that these single-site variants may not be truly representative of the individual active sites.

In Chapter 3, an alternative approach is described where rational design is used to construct an

artificial PHM model in a small metallochaperone scaffold. Using site-directed mutagenesis, we constructed variants that provide a His_2Met copper-binding ligand set that mimics the M-center of PHM. The results showed that the model accurately reproduces the chemical and spectroscopic properties of the M-center, including details of the methionine coordination and the properties of Cu(I) and Cu(II) states in the presence of endogenous ligands such as CO and azide. The rate of reduction of the Cu(II) form of the model by the chromophoric reductant N,N'-dimethyl phenylenediamine (DMPD) has been compared with that of the PHM M-center, and the reaction chemistry of the Cu(I) forms with molecular oxygen has also been explored, revealing an unusually low reactivity towards molecular oxygen. The latter finding emphasizes the importance of substrate triggering of oxygen reactivity and implies that the His_2Met ligand set, while necessary, is insufficient on its own to activate oxygen in these enzyme systems. The PHM M-site also exhibits a number of unusual attributes, including a His_2Met ligand set; a fluxional Cu(I)-S(Met) bond; tight binding of exogenous ligands CO and N_3^-; and complete coupling of oxygen reduction to substrate hydroxylation even at extremely low turnover rates. In particular, mutation of the Met ligand to His completely eliminates the catalytic activity despite the propensity of Cu(I)-His_3 centers to bind and activate dioxygen in other metalloenzyme systems.

In Chapter 4 we further developed the previously-characterized CusF protein-based model to explore methionine variants in which Met is replaced by selenomethionine and histidine. We examined the effects on coordinate structure and exogenous ligand binding via X-ray absorption spectroscopy and electron paramagnetic resonance, and probed the consequences of mutations on redox chemistry via studies of the reduction by ascorbate and oxidation via molecular oxygen. We found that the M-site model is three-coordinate in the Cu(I) state and binds CO to form a four-coordinate carbonyl. In the oxidized forms, the coordination changes to tetragonal five-coordinate with a long axial Met ligand that, like the enzymes, is undetectable at either the Cu or Se K edges. The EXAFS data at the Se K edge of the selenomethionine-labeled variant provide unique information about the nature of the Cu-methionine bond that is likewise weak and fluxional. Kinetic studies document the sluggish reactivity of the Cu(I) complexes with molecular oxygen and rapid rates of reduction of the Cu(II) complexes by ascorbate, indicating a remarkable stability of the Cu(I) state in all three derivatives. The results show little difference between the Met ligand and its Se-Met and His congeners and suggest that the Met contributes to catalysis in ways that are more complex than simple perturbation of the redox chemistry. Overall, the results stimulate a critical re-examination of the canonical reaction mechanisms of the mononuclear copper monooxygenases.

The second research aim is to develop an understanding of the molecular basis of cuprous transport and export in the bacterial periplasmic efflux pump CusCBA and its metallochaperone CusF, which are vital to the detoxification of copper and silver ions in the periplasm of *Escherichia coli*. Metallochaperone CusF binds a single Cu(I) in a Met_2His binding environment with a unique a Cu(I)–π interaction between the metal ion and W44, a nearby tryptophan. Our lab has previously used selenomethionine labeling in combination with X-ray absorption spectroscopy to show that CusF directly transfers Cu(I) ions to CusB and is required for CusCBA export of Cu(I) ions. However, the function of the Cu(I)–π interaction remains elusive, suggesting the inclusion of the Cu(I) from O_2 oxidation and/or the increase in selectivity for Cu(I)/Ag(I), although a role in assisting metal transfer reactivity is also possible.

In order to understand the function of the tryptophan ligand (W44) we performed a mutagenesis study, described in Chapter 5, to characterize changes to structure, site accessibility, and reactivity in response to changes in the capping ligand. We also used selenomethionine labeling combined to rapid freeze-quench sample preparation to compare rates of transfer between CusF and CusB. The results show that the Cu(I)-W44 cation-π interaction in the metal binding site of CusF functions to protect the site from exogenous ligands, with the presence of a capping ligand at position 44 blocking the formation of a Cu(I)carbonyl, monitored by Fourier transform infrared spectroscopy. Additionally, the removal of the W44 capping ligand resulted in a significantly slower rate of reduction, indicating that the W44 ligand functions to increase Cu(I) sensitivity. The Cu(I)-W44 interaction may be also important for Cu(I) transfer between CusF and CusB. While this study was useful in understanding the function of the Cu(I)–π interaction it lacked a direct probe for the ligand at position 44. Described in Chapter 6 we have begun the development of unnatural amino acid incorporation at position 44 of CusF with the goal of adding a unique spectroscopic probe for W44.

CHAPTER 1: Introduction

1.1 Copper in biology

Since the introduction of oxygen into the atmosphere about 2 billion years ago, (Dupont et al., 2011) the bioavailability of copper has allowed it to serve as a redox-active transition metal cofactor for a diverse array of essential metabolic enzymes and proteins in all aerobic organisms. Cuproenzymes are widely distributed throughout all kingdoms of life, generally working between +0.25 and +0.75 V, and are involved in electron transport; dioxygen transport and activation; and denitrification. In humans, cuproenzymes are involved in many physiological functions including cellular respiration, iron metabolism, pigment formation, neurotransmitter biosynthesis, antioxidant defense, and connective tissue formation. Putative copper binding proteins compose ∼1% of the total eukaryotic proteome, suggesting that known cuproproteins represent only a minor fraction of the total (Andreini et al., 2008).

While cuproenzyme-active sites can provide high redox potentials of 0-0.8 V at a lower cost of oxidation compared to iron (Boal & Rosenzweig, 2009), the same redox activity makes unbound copper ions cytotoxic. Human harnessing of the antimicrobial properties of copper can be traced back to the Smith Papyrus, an ancient Egyptian medical text dated to 2400 BC, which records the earliest medicinal recommendation of copper sulfate to sterilize water and treat infections (Dollwet, & Sorenson, 1985). Early Mesoamerican and Greek civilizations used copper to treat a broad variety of physical ailments, including microbial and parasitic infections. In 400 BC, Hippocrates prescribed copper salts to treat leg ulcers. In the nineteenth century, Victor Burq observed that copper workers in Paris appeared immune to recurrent cholera epidemics (Chaturvedi & Henderson, 2014). These observations led to rapid developments in the field of metallotherapy, and medically-employed copper salts, amulets, and belts were widely used to treat dermatologic, gastrointestinal, and tubercular infections (Borkow & Gabbay, 2005; Dollwet & Sorenson, 1985) until the advent of commercially available antibiotics in 1932 (Chaturvedi & Henderson, 2014). Today, copper alloy surfaces are used in hospitals to prevent hospital-transmitted infections (Casey et al., 2010; Gregor Grass et al., 2011; Michels et al., 2015) and copper-based compounds are being developed to treat human fungal infections (Cavet et al., 2014; Festa et al., 2014) as well as to protect crops against the damage of both fungal and bacterial pathogens (Cha & Cooksey, 1991).

Today, two main mechanisms of copper toxicity are known: reactive oxygen species (ROS) generation and enzyme inactivation (Figure 1.1). Under aerobic conditions unbound copper ions can participate in Fenton and Haber-Weiss chemistry, generating hydroxyl radicals (Bremner, 1998) which damage proteins (Kadiiska & Mason, 2002), lipids (Bruska et al., 2015; Bremner, 1998) and nucleic acids (Halliwell & Gutteridge, 1984; Stadtman & Levine, 2003), often referred to as oxidative damage. In bacteria, ROS can also oxidize cysteines (Stohs & Bagchi, 1995) involved in iron binding and iron-sulfur clusters, which leads to an increase in free iron ions able to participate in additional Fenton chemistry (Keyer & Imlay, 1996). There is also evidence that thiol-mediated reduction of Cu(II) can lead to the generation of ROS through intermediate sulfur radical chemistry. Additionally, studies of *E. coli* on copper alloy surfaces suggest that nonenzymatic oxidative damage of membrane phospholipids ultimately results in the loss of membrane integrity and cell death (Hong et al., 2012).

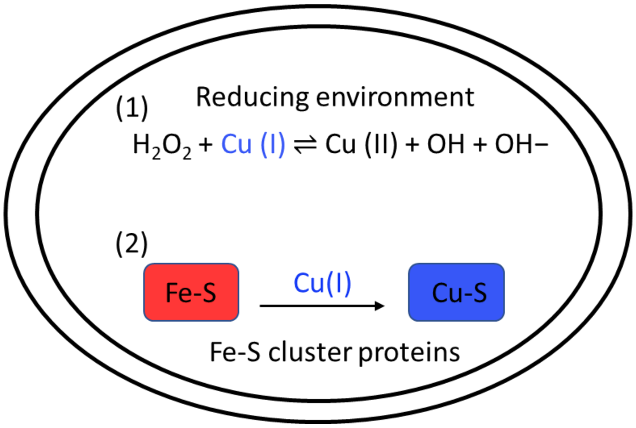

Figure 1.1 Mechanisms of copper toxicity. (1) Free copper ion can patriciate in Fenton-like chemistry, producing hydroxyl radicals which cause oxidative damage. (2) Free copper ions can disrupt other metal-binding active sites; those shown here are particularly vulnerable Fe-S clusters.

The high affinity of copper ions leads to the second toxicity mechanism: enzyme inhibition, due to the disruption of other metal-based active sites (Imlay, 2014; Waldron & Robinson, 2009). Based on the Irving-Williams series, which states that affinities of metal binding ligands to essential metals in the +2 state follow a universal order of preference of [Mg^{2+} and $Ca^{2+} < Mn^{2+} < Fe^{2+} < Co^{2+} < Ni^{2+} < Cu^{2+} > Zn^{2+}$], copper ions have a higher affinity for metal binding ligands (S, N/O) than any other divalent metal (Irving & Williams, 1953). In particular, solvent-exposed iron-sulfur clusters are vulnerable to copper toxicity. For example, citric acid cycle enzymes fumarase-A and aconitase, required for single-electron transfer, (Murakami & Yoshino, 1997) as well as dehydratases that are responsible for branched-chain amino acid biosynthesis, are all highly vulnerable to copper toxicity (Macomber & Imlay, 2009).

As a result, organisms evolved protein-based copper homeostasis machinery allowing for the import and delivery of copper ions to essential cuproenzymes without exposing the cell to free copper. Copper homeostasis proteins exist in all organisms, even those without cuproenzymes. Genetic studies of prokaryotic organisms and yeast have shown that copper homeostasis proteins are highly conserved, and have identified homologous membrane-associated importers and exporters as well as small cytosolic delivery proteins, referred to as metallochaperones. Together, copper homeostasis proteins, including membrane transporters, metallochaperones, and metalloregulatory proteins, function to (1) ensure that copper ions are provided to the correct enzymes and cellular compartments for necessary activities while (2) maintaining a cellular milieu free of unbound copper ions (Finney & O'Halloran, 2003).

Within the cell, copper primarily exists in two oxidation states, the oxidized Cu(II) cupric form and the reduced Cu(I) cuprous form. Both cuproenzymes and copper homeostasis proteins combine unique structural folds to create unique metal binding sites using a limited set of amino acid-derived ligands, most commonly the thiolate of cysteine, the methyl thioether of methionine, the imidazole of histidine, the carboxylates of aspartate and glutamate, and the phenolate of tyrosine. The differences in Cu(I) and Cu(II) chemistry can be described using the Hard-Soft Acid Base (HSAB) theory. As a soft Lewis acid, Cu(I) forms strong bonds with sulfur (S)-based ligands, such as cysteine and methionine, and prefers low coordinate metal binding sites with 2, 3 or 4 ligands often in linear, trigonal planar, or tetrahedral geometries. In contrast, Cu(II) (an intermediate Lewis acid) prefers nitrogen (N), hydroxyl (ROH), carboxyl (ROOH) or primary amine (RNH_2) side chains and prefers a higher coordination number with 4, 5 or 6 ligands in square planar, square pyramidal, or axially distorted octahedral geometries, respectively, the latter being the result of Jahn-Teller distortion. Many cuproenzymes have evolved highly tuned metal binding sites able to quickly cycle between Cu(I) and Cu(II) ions despite drastic differences in preferred binding environments. These labile active sites facilitate redox chemistry by rapidly cycling between the Cu(I) and Cu(II) redox states. Copper homeostasis proteins generally bind and transport reduced Cu(I) ions bound in a sulfur dominated metal binding site.

Due to the cytotoxicity of free copper ions, cells employ many strategies to minimize copper toxicity. An important global strategy employed by all organisms is the confinement of copper ions to specific intracellular spaces within the cell. In eukaryotes, copper ions are confined to the cytosol where they are bound and transported by metallochaperones to their target cuproenzymes. Unlike eukaryotic cells, prokaryotes do not require copper for cytoplasmic enzymes, but instead isolate copper to the periplasmic or inner membrane space (Stewart et al., 1998). Cells also use different metal binding ligands based on intracellular location. For example, due to its pKA of ~8.5, the Cys(S) atom is more sensitive to oxidation and is found mostly in the cytosol, while the Met(S) is less sensitive to oxidation and is more often found in the oxidizing environment of the bacterial periplasm.

1.2 O_2-activating cuproenzymes

A large number of essential cuproenzymes are involved in dioxygen activation and transport. Cuproenzymes are involved in reversible dioxygen binding (hemocyanin) (Solomon et al., 1994); two-electron reduction to peroxide coupled to oxidation of substrates (amine, galactose, and catechol oxidases) (Klinman, 1996); activation for hydroxylation (DβM, PHM, tyrosinase, and particulate-methane monooxygenase (pMMO)) (Klinman, 1996; Solomon et al., 1996); and the four-electron reduction to water coupled to substrate oxidation (laccase, ascorbate oxidase, ceruloplasmin and Fet3p) (Solomon et al., 1996) or proton pumping (cytochrome c oxidase (CCO)), which also contains heme iron centers) (Ferguson-Miller & Babcock, 1996).

Non-coupled binuclear copper monooxygenases use two non-coupled mononuclear copper centers to facilitate chemically challenging substrate oxidation. In the brain, DβM catalyzes the conversion of dopamine to norepinephrine, while PHM is the only known enzyme to convert neuropeptide hormones into their active C-terminally amidated forms. In the environment, lytic polysaccharide monooxygenases (LPMOs) contain functional mononuclear copper centers which catalyze the chemically challenging oxidation at hexose C1 and/or C4, making them important enzymes in biomass degradation. Recently, new studies investigating the structure and function of pMMO suggest the possibility of a mononuclear copper site as the catalytic center for alkane hydroxylation (Ross & Rosenzweig, 2017).

Neuropeptides activated by PHM regulate many essential endocrine processes, including embryonic development, pain, digestion, bone mineralization, sexual response, blood volume, stress response, circadian rhythms, and thyroid function (Kumar et al., 2016). Many of the same neuropeptides have been implicated in Type-2 diabetes including glucagon-like peptide-1 (GLP-1), which regulates appetite, and, via the secretion of insulin, decreases blood sugar levels. Overexpression of PHM has been detected in many endocrine tumors, as well as medullary thyroid carcinoma, pancreatic tumors, glioblastomas, human pituitary tumors, prostate cancers, and small cell lung cancer (Kumar et al., 2016). Despite differing structures and substrate specificities, both DβM and PHM utilize two copper sites separated by an 11Å solvent-filled cleft and react via an identical mechanism. The first step of neuropeptide amidation occurs in the catalytic core of PHM (PHMcc, residues 42-356) via a copper-dependent hydroxylation of the α-C atom of the glycine-extended pro-peptide C-terminus. The reaction involves the transfer of four electrons to O_2, two from the C-H bond and two from an external reductant. To achieve this conversion, the enzyme stores the external electrons on a pair of copper atoms which are thought to be reduced to Cu(I) by ascorbate. Further insights into the structure and catalytic mechanism of PHM are discussed further in section 1.4.

1.3 Copper homeostasis

Disruption to copper homeostasis leads either to an excess or a deficiency of copper ions, both of which are harmful to the cell. The need for copper homeostasis is exemplified by inherited disorders of copper homeostasis such as Menkes syndrome and Wilson's disease, both of which result from the absence or dysfunction of homologous copper-transporting ATPases that reside in the trans-Golgi network of all cells. Despite striking differences in the clinical presentation of these two diseases, the respective ATPases have the same function, and the unique clinical features of each disease are entirely the result of the tissue-specific expression of each protein. Menkes syndrome is an X-linked disorder caused by mutations in ATP7A, expressed in all tissues with high levels in the intestine. The mutation causes a buildup of copper in the small intestine while the brain and other tissues are starved of copper ions, resulting in lethal growth failure and severe neurodegeneration within the first three years of life (Zanni & Bertini, 2018). In Wilson's disease, ATP7B enzyme mutations cause excess accumulation of copper – most dramatically in the liver and brain – resulting in cirrhosis and neuronal degeneration from free radical-induced oxidative damage (Mercer, 2001). Other human copper deficiency studies have found impaired phagocytic indices, decreased antibody response, impaired peripheral mononuclear cell proliferation, lower early T-cell activation and proliferation, and lower cytokine expression (Prohaska & Lukasewycz, 1990) (Sullivan & Ochs, 1978).

While, in general, copper ions are more stable in the oxidized Cu(II) state, proteins involved in copper homeostasis have metal binding sites dominated by Met(S) and Cys(S) residues and are highly tuned to bind and transfer Cu(I). Copper-binding P-type ATPases couple the energy of ATP hydrolysis to move Cu(I) cations across membranes, responsible for Cu(I) import in eukaryotes and export in prokaryotes. Once carried into the cellular compartment, metallochaperones, generally small soluble Cu(I) binding proteins, then transport Cu(I) ions to their partner cuproenzymes through direct protein-protein interactions.

Eukaryotic copper homeostasis. In eukaryotes, the main function of copper homeostasis proteins is to deliver copper to the secretory pathway for cuproenzyme loading without exposing the cell to free copper ions. Intracellular eukaryotic copper homeostasis is best studied in *Saccharomyces cerevisiae* (Figure 1.2). Cell-surface reductases must first reduce dietary Cu(II) to Cu(I) before it can be transported by copper importer, CTR1 (Kim et al., 2008). Members of the Ctr membrane transporter family have been identified in yeast, plants, humans, and other mammals, and contain several methionine-rich motifs at the N-terminus, and conserved cysteine and histidine residues at the C-terminus, where both sets of motifs are used to specifically bind and import Cu(I) ions. Once in the cytosol, Cu(I) ions are bound and transported by three distinct metallochaperones. Antioxidant protein 1 (ATOX1) carries copper ions to Cu(I)-transporting P-type ATPase (CCC2) which is located in the trans-Golgi where copper ions are incorporated into nascent cuproenzymes. The copper chaperone for SOD1, CCS, shuttles copper ions to SOD1 in the cytosol. The CCO copper chaperone, COX, brings copper ions to the mitochondria for CCO. In the mitochondria COX17/11 delivers copper ions to CCO. CCO, located in the mitochondrial inner membrane, requires moving copper across the outer membrane of mitochondria and the subsequent incorporation of copper into two different sites of CCO. This process requires both soluble (COX17 and COX11) and membrane bound proteins (SCO1, SCO2) and involves redox reactions coupled with the transfer of copper between the chaperones (Nevitt et al., 2012).

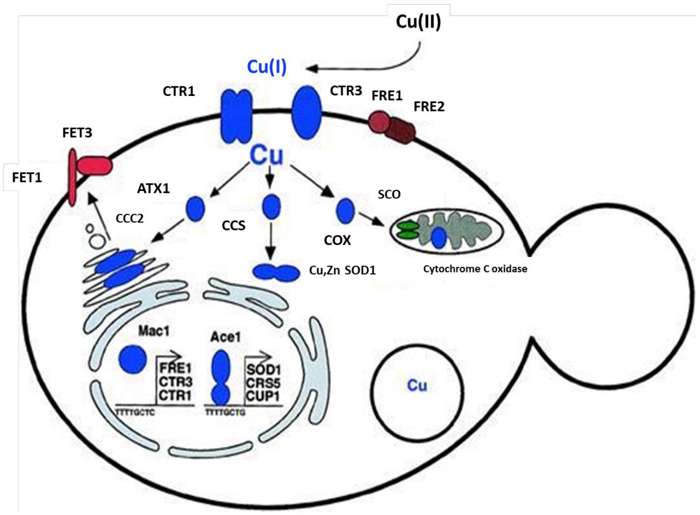

Figure 1.2 Copper homeostasis systems in *Saccharomyces cerevisiae.* Cell-surface reductases reduce dietary Cu(II) to Cu(I) for import by copper importer, CTR1. Cytosolic Cu(I) ions are bound by copper chaperone for SOD1 (CCS), CCO copper chaperones (COX) and antioxidant protein 1 (ATX1). The Cu(I) ions are then delivered to SOD1, CCC2 and COO, respectively. Copper-binding proteins shown in blue and iron-binding proteins shown in red. (Adapted from Peña et al., 1999)

Copper homeostasis at the host-pathogen interface. As discussed above in section 1.1, the reactivity of copper can be harnessed for its antimicrobial properties. Those same properties have also been exploited by eukaryotic hosts as a defense against bacterial pathogens at the host-pathogen interface. As part of the innate immune system, macrophages engulf and contain the microbe within a compartment known as the phagolysosome. Here the pathogen is exposed to high levels of ROS and reactive nitrogen, low pH and proteases, all of which function to kill the microbe. Additionally, phagolysosome can accumulate high copper which, together with phagolysosomal ROS, causes lethal oxidative damage. High levels of copper in macrophage phagolysosomes was first described during infection with Mycobacterium species including the *M. tuberculosis* pathogen for tuberculosis (Wagner et al., 2005). Since then, macrophage copper has been shown to be important in killing *E. coli* (White et al., 2009) and inducing copper toxicity stress for *Salmonella* (Achard et al., 2012; Osman et al., 2010). Even fungi such as *Candida albicans* show symptoms of high copper exposure during encounters with macrophages (Douglas et al., 2012). The mechanism by which macrophages accumulate this high copper is believed to involve a combination of increasing copper uptake by the high affinity copper transporter CTR1 and by activating the copper ATPase ATP7A, which can directly pump copper into the phagolysosome (Achard et al., 2012; Ding et al., 2013; White et al., 2009). Studies using macrophage-like RAW264.7 cells showed that hypoxia, often experienced during macrophage activation, increases expression of Ctr and ATPase proteins causing an increase in free Cu(I) level within the macrophage. The observed reduction in CCS, SOD1 and CCO suggests a change in intracellular copper distribution within the macrophage, not observed in other cell types. The killing of *E. coli* within the phagosome has been shown to be greatly affected by growth media copper concentrations thought to be linked to ATP7A-mediated copper trafficking from the Golgi apparatus to *E. coli*-containing phagolysosomes (Chaturvedi & Henderson, 2014).

Prokaryotic copper homeostasis. As expected, the copper-mediated killing by the innate immune system has exerted selective pressure on copper resistance in pathogenic bacteria. As a result, prokaryotic pathogens have many mechanisms of copper tolerance, including ATPases, oxidases, and efflux pumps, which work together to protect their macromolecules from copper-mediated damage. Unlike eukaryotes, bacteria do not have many copper-requiring enzymes in the cytoplasm and work hard to detoxify any copper ions that leak through. Perhaps as a result, no homologs of eukaryotic Ctr proteins or CCS have been identified in prokaryotes. However, both Cu(I) and Cu(II) can permeate the outer membrane of *E. coli* and enter the periplasm, but only Cu(I) is able to cross the inner membrane and reach the cytoplasm by a currently unknown mechanism. Prokaryotes have diverse copper-tolerance machinery including copper efflux (Cue, Cus, and extrachromosomal efflux systems), copper sequestration (CusF and siderophores), and copper oxidation (mixed copper oxidases and SOD1 mimics) (Figure 1.3).

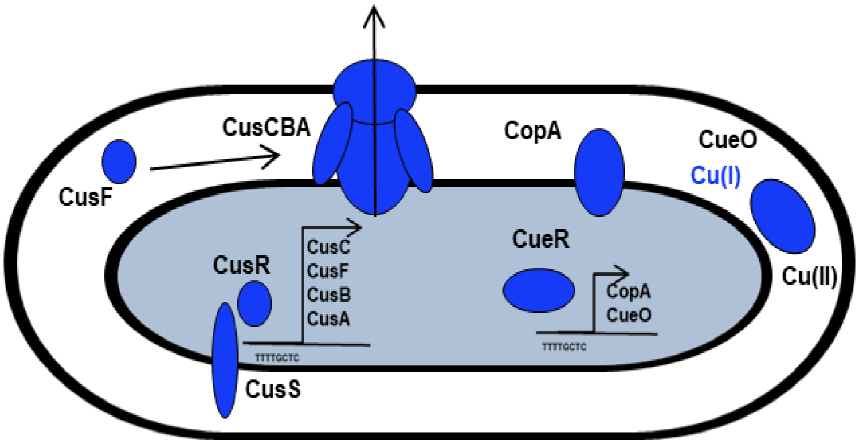

Figure 1.3 Copper homeostasis systems in *Escherichia coli.* Copper-binding proteins shown in blue.

Like eukaryotes, Cu(I) binding P1B-type ATPases are widespread and required for intrinsic prokaryotic copper resistance. In many prokaryotes, the P1B-ATPase, CopA, exports Cu(I) from the cytoplasm to the periplasm during times of high copper stress (Fan & Rosen, 2002; Outten et al., 2000; Petersen & Møller, 2000). Sensed by regulator CueR and possibly influenced by cell envelope stress sensed by CpxR, CopA binds two Cu(I) ions per monomer which are transported into the periplasm upon ATP hydrolysis (Rensing et al., 2000). CueR coordinates one Cu(I) ion per monomer in linear S–Cu(I)–S coordination with 2 Cys(S) ligands located at the dimer interface. (Changela et al., 2003; Chen et al., 2003). In *E. coli* multi-copper oxidase, CueO, is also regulated by CueR and thought to oxidize Cu(I) to less toxic Cu(II). However, CopA is known to bind Cu(I) so the function of copper oxidation by CueO is still somewhat ambiguous (Grass & Rensing, 2001).

In addition to the chromosomally-encoded copper resistance machinery, many bacteria have additional copper resistance plasmids, only used during times of high copper stress. The *pco* plasmid is found in copper resistant *E. coli*, isolated from the discharge of an Australian pig farm where the diet of the animals had been supplemented with $CuSO_4$. The seven gene operon *pco*ABCDRSE is expressed from the upstream, copper-inducible promoter P*pco* (Bryson et al., 1993; Munson et al., 2000; Rouch & Brown, 1997; Tetaz & Luke, 1983). PcoA is a periplasmic multicopper oxidase, PcoB and PcoD are outer and inner membrane proteins, respectively, and PcoR and PcoS are regulatory proteins. PcoC and PcoE are soluble periplasmic proteins. PcoC has been structurally characterized and is hypothesized to interact with PcoA. Spectroscopic studies of PcoC report a cupredoxin-like fold and a Cu(I) ion coordinated by two Mets, a N/O-donating ligand and Cu(II) at separate metal binding site, coordinated by two His ligands, N/O-donating ligands, and water. (Peariso et al., 2003). Pco proteins can bind both Cu(I) and Cu(II) ions within conserved methionine and histidine-rich metal binding sites.

The Cus system. Gram-negative bacteria, including *E. coli*, also require periplasmic copper protection. The *cus*CFBA operon encodes for CusA, CusB, and CusC proteins which resemble multidrug resistance systems, and unique soluble metallochaperone CusF. Regulated by the two-component system CusRS, made up of histidine kinase CusS and transcription regulator CusR, the tripartite CusCBA efflux pump spans the periplasm requiring RND-pump CusA, adapter protein CusB and channel-forming CusC (Figure 1.4). CusA has been characterized by X-ray crystallography, and shown to bind Cu(I) and Ag(I) in a Met(S)$_3$ binding environment (Long et al., 2010). The structure of CusA together with CusB revealed that 6 monomers of CusB form a channel-like complex with a trimer of CusA (Su et al., 2011). CusB also contains a Met(S)$_3$ binding site for Cu(I) and Ag(I) that has been characterized by biochemical and EXAFS studies (Bagai et al., 2007). A crystal structure of CusC does not reveal any obvious metal binding features, supporting its function as a pore and suggesting that the Cu(I)/Ag(I) specificity of the Cus system likely comes from CusA and CusB (Kulathila et al., 2011). Unlike other RND efflux pumps, the Cus system adapter protein CusB has regulatory function and requires novel metallochaperone CusF (Franke et al., 2003).

The 1.5 Å resolution crystal structure of apo and Cu(I)-loaded CusF reports a small five stranded β-barrel resembling an unusual oligonucleotide/oligosaccharide binding (OB) fold (Xue et al., 2008). CusF binds one Cu(I) ion in the Met(S)$_2$His(N) metal-binding site, oriented towards the interior of the β-barrel, and exhibits trigonal planar geometry, with capping tryptophan ligand shown to interact in a novel cation-π interaction with the bound metal (Loftin et al., 2007) (Figure 1.4). Functional studies have implicated CusF in the regulation of metal ion efflux, suggesting that it may deliver Cu(I) and Ag(I) to CusB (Bagai et al., 2008), which may induce a conformational change in CusB triggering metal efflux via an unknown mechanism. The process may be like a ‘funnel,’ where metals bound to CusB are transferred to CusA and then ejected out of the cell, or the CusF to CusB metal transfer may act as a ‘switch’ for the CBA complex, allowing efflux of free periplasmic metals (Kim et al., 2011). EXAFS studies from the Blackburn Lab support the “switch” model where the Cu(I) transfer from CusF to CusB activates CusA and the back transfer from CusB to CusF deactivates CusA, discussed further in Section 1.6 (Chacón et al., 2014). There is also evidence that Cu(I) ions transported by CopA are bound by CusF for efflux by the CusCBA pump (Padilla-Benavides et al., 2014). However, the function of the Cu(I)–π interaction remains elusive, with suggestions including protection of the Cu(I) from O_2 oxidation and/or increase in selectivity for Cu(I)/Ag(I), although a role in assisting metal transfer reactivity is also possible. In Chapter 5, we present a mutagenesis study of W44 in order to characterize changes to structure, site accessibility, reactivity, and Cu(I) transfer in response to changes in the capping ligand.

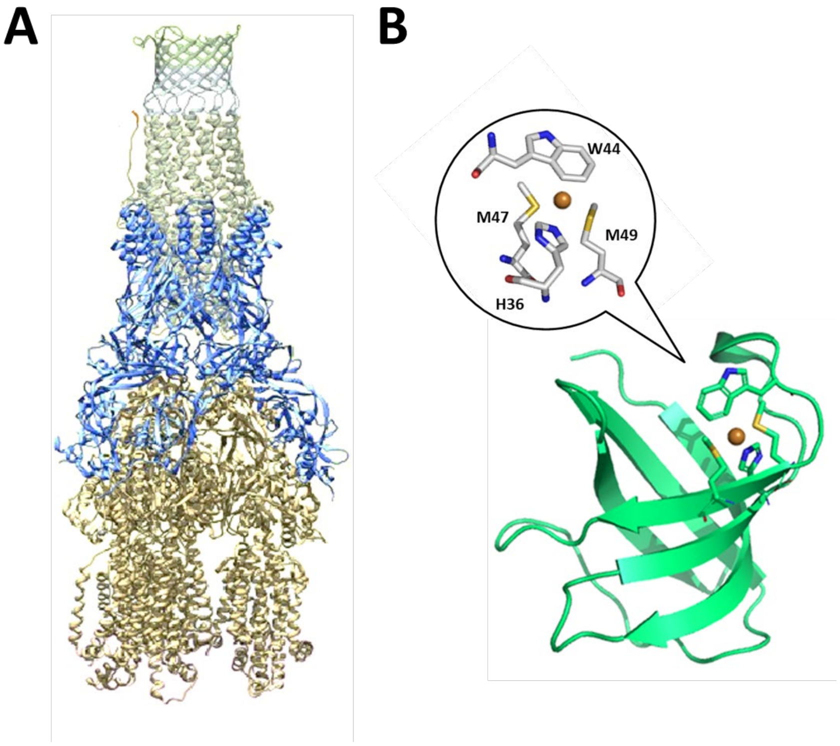

Figure 1.4 (A) Proposed structure of CusCBA efflux pump. (CusA shown in olive, CusB shown in blue and CusC shown in pale green) (B) crystal structure of metallochaperone CusF. (PDB 2VB2)

1.4 PHM structure and mechanism

Extensive crystallographic (Prigge et al., 1997, 1999, 2000; Vendelboe et al., 2016), spectroscopic (Bauman et al., 2011; Boswell et al., 1996; Chauhan et al., 2014; Jaron & Blackburn, 2001), kinetic (Evans et al., 2003; Klinman, 1996, 2006a; Osborne et al., 2013) and computational (Chen et al., 2003; Chen & Solomon, 2004; Crespo et al., 2006) work on PHM suggests as shown in Figure 1.5 that the M-center is the catalytic center, coordinated by a unique His_2Met ligand set, while a His_3, H-center, is responsible for electron storage and transport. Initial oxygen binding and the following catalytic chemistry occurs at the M-center with a copper ion coordinated by H242, H244, and a weak, yet catalytically essential interaction with the thioether of M314 (Bauman et al., 2011). The two reducing electrons provided to the M-site are hypothesized to be supplied by the H-center via long range electron transfer (ET). The H-site is coordinated by three essential His residues H107, H108, and H172, in an unusual T-shaped geometry with the mutation of any one histidine eliminating catalytic activity. A conformational change of the CuH sites has also been observed at low pH where M109 binds the Cu ions, replacing H242 and eliminating catalytic activity (Kline et al., 2013). It has also been shown that exogenous ligands (O_2, CO, peroxide, and azide) can bind to the catalytic M-center but are excluded from the H-center by electronic or steric factors which are incompletely understood (Chauhan et al., 2014; Chufán et al., 2009; Jaron & Blackburn, 2001).

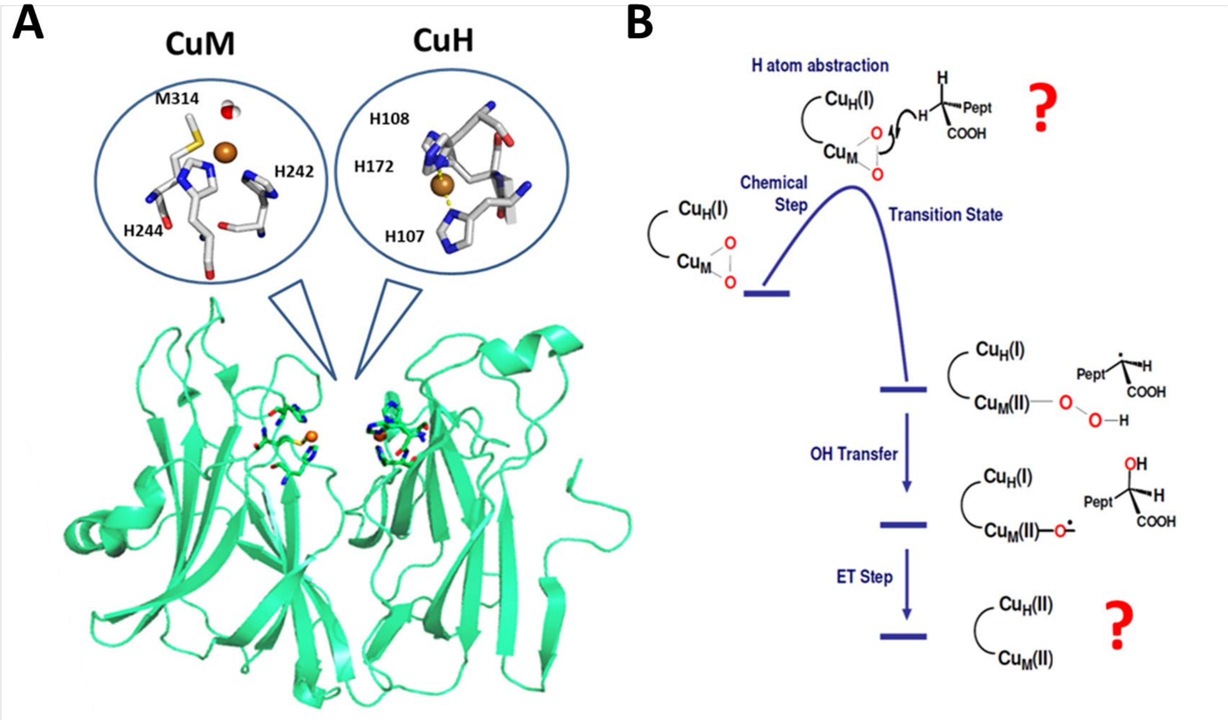

Figure 1.5 (A) Crystal structure of PHM (PDB 1PHM) and (B) its proposed catalytic mechanism.

In a proposed canonical mechanism, the Cu(I)M - substrate complex reacts with oxygen to form a Cu(II)-superoxo intermediate with sufficient electrophilicity to abstract a hydrogen atom from the nearby peptide substrate (Bauman et al., 2006; Chen & Solomon, 2004; Evans et al., 2003). Many questions remain about the structure and function of the proposed 1:1 Cu/O_2 adduct as it is short-lived and challenging to capture within a cuproenzyme. A large effort has been put forth to produce synthetic active site analogs able to produce more stable Cu-oxo intermediates for characterization using low molecular weight complexes that resemble the targeted metalloprotein active site, either in a resting state or as a reactive intermediate (Chen et al., 2003, 2004; Evans et al., 2003). Stability has been increased by using low temperatures (200K) and aprotic solvents (CH_2Cl_2, THF, acetone). Cu(II)-superoxo intermediates produced in model compounds have been shown to have the required potent electrophilic reactivity to perform H-atom abstraction (HAT) from the substrate to form a mononuclear hydro-peroxo species (Cu(II)-O-O-H) at the CuM site, along with a substrate radical (Chen et al., 2003, 2004; Evans et al., 2003). An X-ray structure of an "oxy-PHM complex," where a dioxygen molecule is bound at the reduced M-center site, produced a close structural analogue for the predicted reactive superoxo species with a four-coordinate, distorted tetrahedral coordination environment (Prigge et al., 2004). Enzyme-bound cupric superoxo species have also been proposed as intermediates in LPMO catalysis, where rapid re-oxidation of the mononuclear Cu(I) center by O_2 is suggestive of the formation of an unstable Cu-superoxo species (Kjaergaard et al., 2014), but spectroscopic characterization of either intermediate has yet to be achieved.

Additional questions remain regarding long ET since HAT chemistry via a cupric-superoxo species would generate an intermediate, thought to be a Cu(II)-hydroperoxo coupled to a C-α-based substrate radical, requiring a second electron to break the O-O bond and generate a metal-based oxyl radical, followed by radical rebound to the products (Figure 1.5B). The second electron could either be supplied via long-range ET from the H-center, or by formal oxidation of the M-center to Cu(III) to generate a Cu(III)-OH intermediate. Previous studies suggest that ET occurs in a bifurcated manner in which H108 and the substrate are important for the reductive pathway, while H172 and Y79 are involved in the catalytic pathway (Chauhan et al., 2014).

Recently, the first crystal structure of PHM homolog DβM was published (Vendelboe et al., 2016). Two different conformations of the enzyme were observed: in the "open" conformation, similar to PHM, the two copper sites of DβM are ~14 Å apart, while in the other, "closed" conformation, the binding sites are only ~4 to 5 Å apart. This finding is also supported by spectroscopic FTIR data from the Blackburn Lab which suggests the possibility for multiple conformational states of PHM, one of which could bring the two copper sites closer together for the required ET. Data from the Blackburn Lab has shown that carbon monoxide (CO) forms a Cu(I)carbonyl complex at the reduced M-center with a C≡O stretching frequency (v(CO)) of 2092 cm^{-1}. The decrease in v(CO) from that of free CO (2143 cm-1) to bound CO is consistent with back-bonding from the filled d-electron manifold into the empty π^* CO antibonding orbitals and is assisted by electron-rich imidazole ligands. In the presence of substrate an additional v(CO) is observed with a frequency to 2063 cm^{-1}. The ~30 cm^{-1} decrease in v(CO) suggests that the substrate causes an increase in the electron-donating power of the M-center ligand set. However, both v(CO) (2092 cm^{-1} and 2063 cm^{-1}) are present, suggesting two forms of the enzyme (Kline & Blackburn, 2016). The crystallographic data together with the FTIR data suggests it is possible that the closed conformation could be the catalytically active conformer, similar to binuclear enzymes such as tyrosinase and catechol oxidase.

To understand the complex mechanism of PHM, both copper sites must be studied individually, as each site has its own unique function. However, the similarity in ligand sets, proximity, and lack of unique spectroscopic signatures makes distinguishing the two copper sites challenging. The Blackburn Lab produced and characterized single site mutants of PHM. Structural characterization of PHM H242H (M-center only) and PHM H107AH108A (H-center only) mutants supported the His_2Met and His_3 ligand sites observed in WT, respectively (Chauhan et al., 2014). While attempts at producing single M-center- and H-center-only PHM have been successful, crystallographic data suggests both metal sites are required for native structure.

1.5 Modeling cuproenzymes

As discussed above, synthetic active site analogs have been integral in understanding the structure and function of the proposed 1:1 Cu/O_2 adduct. However, while there has been success in this field, these model compounds have failed to create exact structure mimics and lack the properties provided by protein folds, including second sphere ligand interactions (Mann et al., 2018). In order to study copper containing active sites within a protein backbone, artificial metalloproteins (ArMs) have been developed using de novo design (DeGrado et al., 1999) or by redesigning existing metalloproteins (Lu et al., 2001). Much of de novo design of metalloproteins has centered around α-helical bundles, a common scaffold for several native heme-binding proteins. Four-helix bundles containing a $His(N)_2Cys(S)$ copper binding site have been successfully produced and characterized by the Hildebrandt Lab. They have also added a second metal-binding site to the four-helix bundle scaffold, via the addition of two Met(S) residues above the histidine ligands, to create a mixed-valent dinuclear copper binding site which generated very similar spectroscopic properties to those of Cu(A) sites in natural proteins (Schnepf et al., 2004). The Pecoraro Lab has produced a three-helix bundle, made up of TRI coils (Dieckmann et al., 1998), containing the $His(N)_3$ type 2 copper center found in native copper nitrite reductase, which is able to catalyze the reduction of nitrite with at least five turnovers and no loss of catalytic efficiency after 3.7 hours (Tegoni et al., 2012).

There has also been a wide array of success redesigning copper binding sites of existing metalloproteins. The Borovik Lab has successfully redesigned and characterized a host protein, streptavidin (Sav), to model the structure and properties of the Type 1 cupredoxin site, using optical and EPR spectra in combination with XRD to detect the desired Cu(I)-Cys(S) bond (Mann et al., 2016). Additionally, they showed that modulation of the biotin-Sav linker length allows for small changes in the copper site location which has a large effect on the structural and physical properties of the resulting artificial metalloproteins. In subsequent work, the Borovick Lab was able to stabilize a Cu/OOH adduct, both in solution and *in crystallo*, by changing the hydrogen bonding network around the local copper-binding environment (Mann et al., 2017). The Lu Lab has extensively repurposed the type 1 blue copper binding protein, azurin, involved in ET. Like all type 1 copper proteins, azurin binds a single Cu(II) ion using a His(N)$_2$Cys(S) ligand set with a unique methionine and main chain carbonyl in the axial positions in a bipyrimidal geometry. The Lu Lab has engineered the copper binding site to produce azurin with red (based on nitrosocyanin) (Clark et al., 2010) and purple (mimic of CCO) (Hay et al., 1996)(Wilson et al., 2013) copper binding sites. To further investigate the structure, reactivity, and kinetics of the CuM and CuH-sites, we developed a small protein-based scaffold with a single copper binding site. In Chapter 3 we describe the rational design and characterization of an artificial PHM M-center model using a small metallochaperone scaffold. As described in Chapter 4, we further developed the previously characterized CusF protein-based model to explore methionine variants in which Met is replaced by selenomethionine and histidine.

Chapter 2: Spectroscopic methods

2.1 UV-visible spectroscopy of cupric-containing proteins

Optical spectroscopy can be used to classify cupric-containing proteins, as cupric ions have an unfilled d-shell with a $3d^9$ electronic configuration allowing for the excitation and observation of d-d transitions within the visible spectrum. Ligand-to-metal charge transfer (LMCT) transitions, which arise from the interaction of high-valent metal ions and electron-rich ligands, can also produce bands within the visible spectrum. Within cupric-binding proteins the coordination environment has a major influence on the intensity and shift in observed energy; therefore, monitoring absorption via the ultraviolet/visible spectrum (UV/Vis) is ideal for probing the electronic structure of cupric protein sites. Type 1 "blue" copper proteins have been highly characterized as containing a single copper ion coordinated by two His(N) and one Cys(S) in a trigonal planar geometry; their intense blue color results from a strong Cys(S)-Cu LMCT band around 600 nanometers.

However, as discussed in section 1.2, type 2 copper centers are dominated by histidine residues in a distorted square planar geometry with room for a water or substrate molecule, but they do not have a required sulfur atom for the 600 nm LMCT band. Type 2 "non-blue" copper centers require additional small ligands, including azide (N_3^-), to produce visible LMCT bands. Cu(II)-azide complexes are known to exhibit strong azide-to-Cu(II) LMCT bands at around 400 nm, which can be used as a reporter for N_3^- binding in solution. Examples of Cu(II) characterization by azide titration can be found in sections 3.3 and 4.3 of this dissertation. Binuclear, type 3 copper centers are also His(N) dominated and produce strong LMCT bands between 350 and 580 nm when loaded with small ligands including O_2 and N_3^-.

Besides steady-state azide-binding assays, the same LMCT band can be tracked using UV/Vis stopped-flow spectroscopy for kinetic experiments on a millisecond time scale. Stopped-flow measurements can be made by rapidly mixing two components, such as an apo protein and a metal ion, or a cupric ion and a reductant. Once mixed, UV/Vis spectra are measured on the millisecond timescale via high sensitivity photodiode array detectors. The spectra can then be fit and used to derive kinetic data including the rate of oxidation and reduction, which can help to understand redox potentials of different copper-containing active sites. An example monitoring the LMCT band of an azide-Cu(II) species will be shown in sections 3.3 and 4.3 of this dissertation.

2.2 Electron Paramagnetic Spectroscopy of cupric-containing proteins

Electron paramagnetic spectroscopy (EPR) can be applied to any species containing one or more unpaired electrons, including cupric ions and cupric-containing proteins. The basic concept of EPR is analogous to nuclear magnetic resonance (NMR), but instead of exciting the spin of an atomic nucleus (like a proton), it is the electron spins in the material that are excited. EPR can be a very useful tool in understanding the structure and reactivity of cupric-binding proteins, as well as in quantifying the amount of paramagnetic material in samples. The unpaired electron is excited using a constant magnetic field, generally in the microwave region (2-36 GHz). Many spectrometers operate at frequency of 9 GHz (X band), which provides a balance between sensitivity and ease of sample handling, often run at very low liquid nitrogen temperatures (-180°C) to reduce background microwave noise.

The constant magnetic field causes an energy difference between the two spin states, $m_s = +½$ and $m_s = - ½$, where +½ is parallel to the z-axis of the magnetic field and - ½ is antiparallel. The spin state on the electron can flip when electromagnetic radiation is applied. The energy difference between the two spin states can be described in the equation below (1) and in Figure 2.1a where h is Planck's constant (6.626×10^{-34} J s^{-1}), υ is the frequency of radiation, ß is the Bohr magneton (9.274×10^{-24} J T^{-1}), B_0 is the strength of the magnetic field in Tesla, and *g* is the g-factor.

$$\Delta E = g_e \beta B_0 \text{ or } h\upsilon = g_e \beta B_0 \qquad (1)$$

The g-factor (g) is a unitless measurement of the intrinsic magnetic moment of the electron; its value for a free electron (g_e) is 2.0023 but in metal complexes it takes different values, as a consequence of the coupling of spin and orbital angular momentum moments. While low symmetry molecules have very little or no orbital magnetic moment contribution, spin-orbit coupling is able to restore some of the orbital contribution and leads to deviation of the g-value of the free electron. The g-factor can roughly be equated to that of chemical shift in NMR, revealing information about the electronic nature as well as the chemical nature of the paramagnetic molecule. Since the frequency of the instrument is known, the magnetic field required for the resonance condition can be used to calculate *g*. The value of *g* is characteristic of electronic properties of the unpaired electron and can be calculated by rearrangement of this equation:

$$g=h\nu/\beta B_0 \tag{2}$$

Additionally, the g-factor of many paramagnetic species, including Cu(II), is anisotropic, meaning that it depends on the orientation of the molecular species in the magnetic field. As a result, the g-factor can report on the orbital occupancy of the metal center. For anisotropic molecules the g-factor is measured along each axis, g_x, g_y and g_z. Based on their values, the type of anisotropy can be determined. When $g_x = g_y = g_z$ the spectrum is considered to be isotropic, and is not dependent on orientation in the magnetic field. When $g_x = g_y > g_z$, as often observed in Cu(II) systems, the spectrum is considered to be axial with elongation along the z-axis. The two equivalent g values are known as $g\perp$ while the singular value is known as $g\parallel$. It exhibits a small peak at low field and a large peak at high field. When $g_x = g_y < g_z$ the spectrum is also said to be axial, but shortened in the xy plane. It exhibits a large peak at low field and a small peak at high field. When $g_x \neq g_y \neq g_z$ the spectrum is said to be rhombic, and shows three large peaks corresponding to the different components of g.

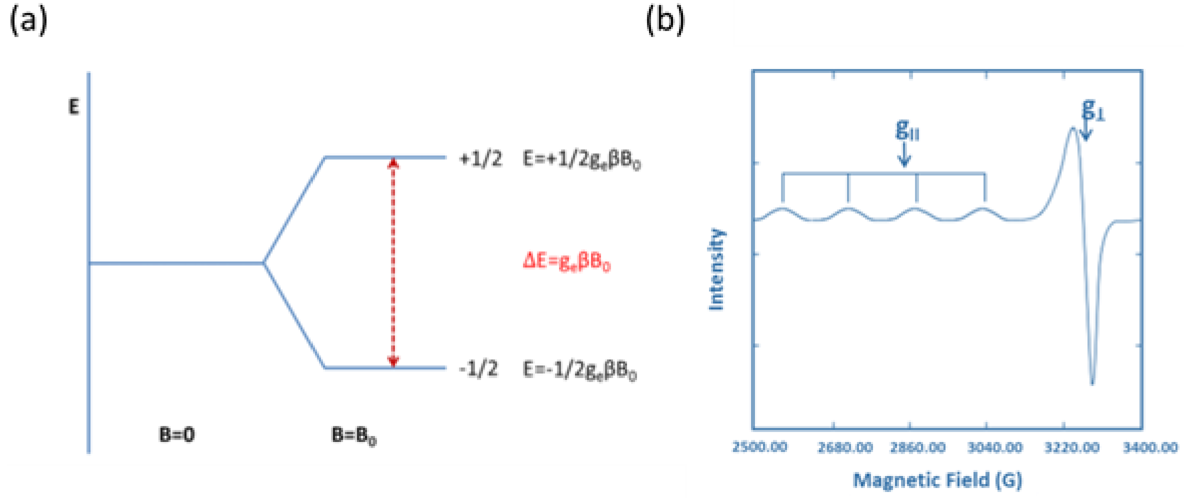

Figure 2.1 (a) Splitting of the electron energy levels in an applied magnetic field and (b) a typical axial spectrum of a powder Cu(II) compound.

An EPR spectrum also contains hyperfine splitting, resulting from the coupling of the electron magnetic moment to the magnetic moment of its own nucleus, and superhyperfine splitting when the electron is coupled to a nucleus of a different atom. The resonance is split into a multiple line pattern with the number of lines given by 2nI+1. In Figure 2.1b hyperfine interactions for a cupric ion can be observed for the peak at $g_\parallel$, which has been split into four lines of equal intensity. This implies the presence of a nuclear spin of 3/2 which is characteristic of Cu(II) metal. Coordination geometry of the Cu(II) compounds can also be determined from the EPR spectra, making this a very useful technique. An example of using EPR to characterize and quantify a Cu(II) center will be shown in sections 3.3 and 4.3 of this dissertation.

2.3 X-ray absorption spectroscopy of copper-containing proteins

While UV/Vis and EPR spectroscopy are useful for cupric ions, they provide little information for cuprous species, a 10d system which lacks both d-d optical transitions and paramagnetism. Studying cuprous ions is feasible by using extremely high energies, made possible by synchrotron radiation. Tuned X-rays can be harnessed to eject a core electron from an element and produce scattering interactions between ligands and the metal ion, in a technique known as X-ray absorption spectroscopy (XAS). XAS takes advantage of the photoelectric effect, in which an X-ray is absorbed and a core-level electron is promoted out of the atom into the continuum. The absorbance can be measured as the energy-dependent absorption coefficient, μ, defined as the probability that X-rays will be absorbed by the sample according to Beer's law (3), where I_0 is the intensity of the incident radiation, t is the sample thickness, and I is the intensity of the transmitted radiation.

$$I = I_0 e^{-\mu t} \tag{3}$$

A typical X-ray absorption spectrum is obtained by plotting absorption on the y-axis versus the energy of the incident radiation on the x-axis, for a range of energies. The resulting XAS spectra are sensitive to the formal oxidation state, the coordination chemistry, and the distances, coordination number and species of the atoms immediately surrounding the selected element. The high-energy X-ray beam must be tuned to order to produce the required energy to eject the core electron. Each element requires different known energies. Figure 2.2 shows the X-ray beam as it is tuned to a specific energy using a double crystal monochromator made up of two parallel crystals which can be rotated relative to the direction of the beam. The desired energy X-rays are selected by varying the Bragg's angle ($n\lambda = 2d\sin\theta$). The monochromator selects multiple wavelengths for each value of n, which are termed the fundamental (n=1) and harmonics (n=2,3,4…). The higher harmonics interfere with the quality of the data and the ability to perform accurate analysis and must be removed. This is achieved by the incorporation of an Rh mirror downstream from the monochromator which limits the energy of the selected X-ray. A 12.5 KeV energy cut-off is used for Cu, while a 15 KeV cut-off is used for Se. To calibrate the energy, the beam is passed through a "foil" of the selected element placed between the first and second ionization chamber.

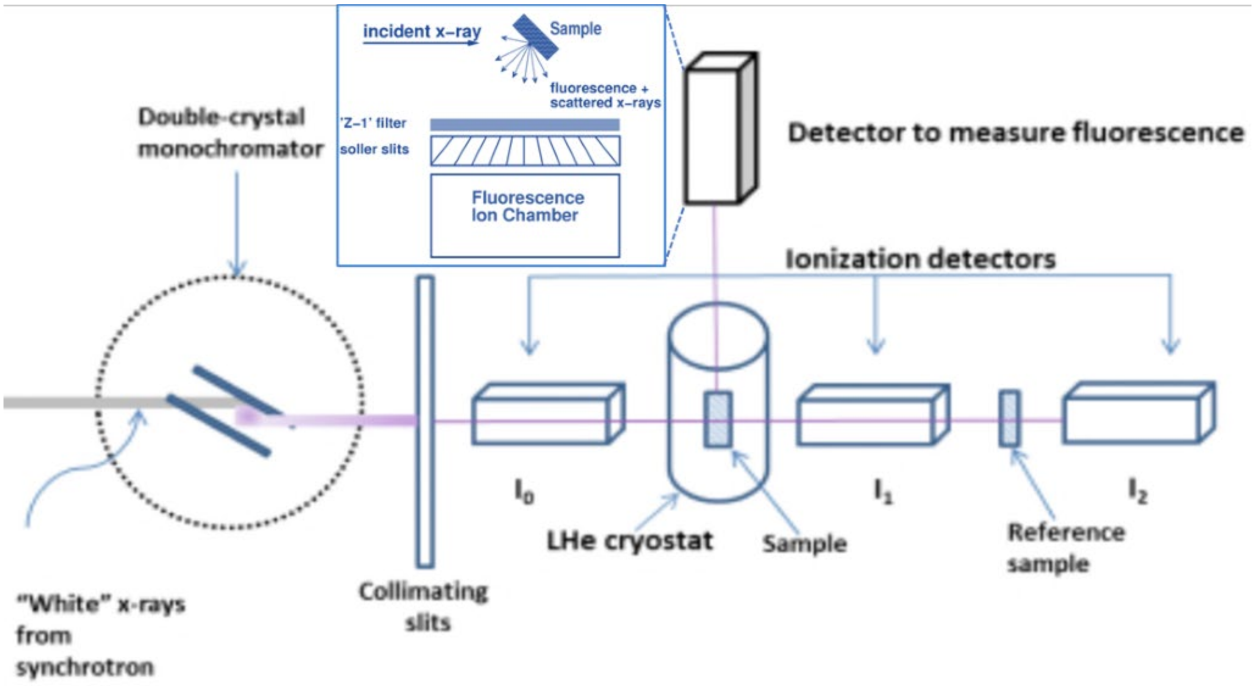

Fig. 2.2 Simple schematic of a typical X-ray absorption spectroscopy instrumental setup. Inset of Ge detector setup for fluorescence mode XAS.

As the tuned X-ray reaches the required energy, the core electron is ejected, producing a photoelectron. This results in a large observable change in measured absorption, referred to as “the edge”, representing the energy of the incident radiation required to eject an electron from the 1s orbital of the metal. Following an absorption event, that atom is in an excited state with an empty core hole. The core hole is then filled by an electron from the n=2 level, which results in an emission of an intense X-ray emission photon. The X-ray emission contains the fluorescence line of interest, fluorescence lines from other elements in the sample, and both elastically and inelastically scattered X-rays. In order to collect only the fluorescence line of interest, a Z-1 filter (nickel for Cu and arsenic for Se) and a Soller slit assembly are placed in front of the Ge detector to block Kβ fluorescence, produce a flat pre-edge baseline and reduce elastic scattering, respectively. Additionally, all emission energies are known for each metal. which allows for “windowing” of the detector in the Kα fluorescence and helps to eliminate background noise. For biological XAS, the samples are often low in concentration and must be frozen as aqueous glass and measured at 4K to avoid radiation damage. The 1s core electron of Cu(I) is ejected when the X-ray energy reaches 8980 eV producing a core hole which is then filled by an L shell electron dropping into the K level and giving the Kα fluorescence line. The precise ionization energy required by the absorbing metal atom is affected by the valence and oxidation state. This can be useful in assigning oxidation states of copper atoms, as the Cu(II) atoms are more difficult to ionize compared to Cu(I), shifting the K-edge to a slightly higher energy. Studies of the edge regions, referred to as X-ray absorption near-edge structure (XANES), provides information about the local geometry and oxidation state of the atom based on the appearance and energy location (Figure 2.3).

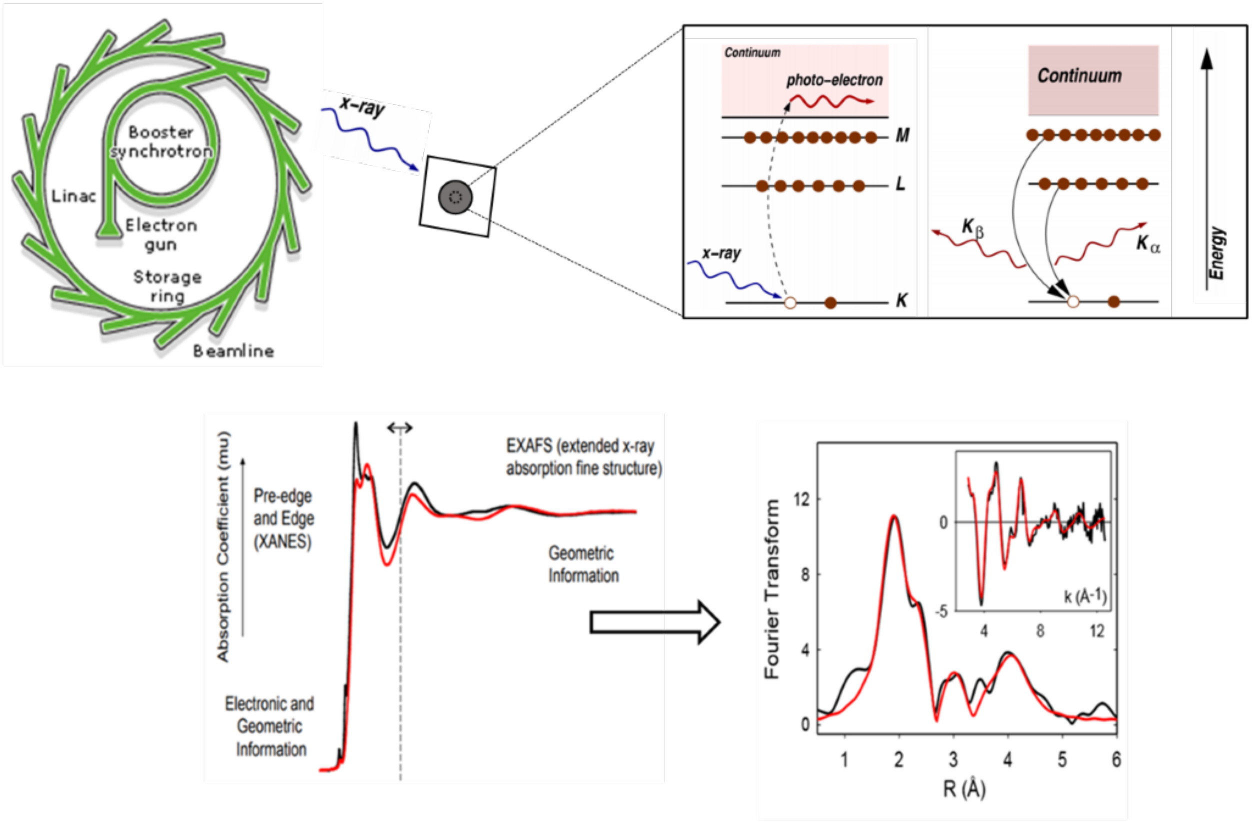

Figure 2.3 Schematic of XAS (top) and examples of XAS spectra showing both XANES and EXAFS regions and resulting Fourier-transform (bottom).

Spectra can also be collected at higher energies, past the edge, referred to as extended X-ray absorption fine structure (EXAFS) (Figure 2.3). These spectra are quasiperiodic modulations produced by the interactions between the emitted photoelectron with the backscattered waves from the immediate neighbors of the absorbing atom. As the modulations are the results of the photoelectron scattering from the surrounding ligands of the metal center, they carry information about the local environment, namely the number, type and the distance from the metal center. The overall description of all factors that contribute to an EXAFS spectrum has been described using the EXAFS equation:

$$\chi(k) = \sum_{s} \frac{N_s\,[f_s(\pi,k)]}{kR_{as}^{2}} \exp(-2\sigma_{as}^{2}k^{2}) \sin[2kR_{as} + \alpha_{as}(k)] \tag{4}$$

The equation comprises terms representing amplitudes, frequencies, and phase shifts from the shells of the absorbing (a) and scattering (s) atoms described above. The summation of waves is proportional to the number of scattering atoms (N_s) and their backscattering amplitudes [$f_s(\pi,k)$], with long-distance shells causing much weaker EXAFS compared to nearby atoms (R_{as}^{-2}). The Debye-Waller factor is described by σ_{as}^2 and can be thought of as a stretching vibration (or disorder) between the a-s bond, which can be static or dynamic. These variations have characteristic temperature dependencies and can dampen the EXAFS signals. The sine function describes the frequency ($2R_{as}$) and phase shift ($\alpha_{as}(k)$) which are proportional to the a-s distance and nature of both atoms, respectively.

Once collected, EXAFS spectra must be processed; the Fourier function is then applied to generate a Fourier transform (FT). The FT preforms a frequency analysis of the EXAFS, yielding a peak at the frequency of each sine wave component in EXAFS (Figure 2.3). The sine wave frequency is directly proportional to the metal-ligand separation distance; the FT generates a set of peaks where the x-axis represents the distance from the absorbing atom in Ångstroms (Å) in radial distance space, with each peak representing a particular shell of atoms and the unitless y-axis representing wave intensity. At this point, these frequencies can be simulated by computational methods and the distance and identity of these contributions can be resolved. Once deconvoluted into a FT, EXAFS can provide direct structural information regarding the radial distance from the absorbing atom to its neighboring atoms, as well as the identity of those atoms. XAS provides extremely accurate interatomic distances (± 0.02 Å), and as such can be used to refine crystal structure interatomic distances, for example. Coordination numbers are less defined (± 20%), and distinguishing the identity of a scattering atom is generally only possible between different rows of the periodic table. For example, N can be distinguished from S but not from O.

2.4 Rapid freeze quench

Rapid freeze quench (RFQ) is the process of arresting a rapidly mixed chemical reaction by extreme cold temperatures. It was pioneered by the Bray Lab in 1961 and has been used increasingly in spectroscopy as a means to trap chemical intermediates for spectroscopic study without the need to alter the reaction conditions, which would alter the phenomenon one wishes to study (Bray, 1961; George et al., 1986). RFQ has been used in Resonance Raman, EPR, and XAS, and in other techniques where it would ordinarily be difficult to monitor a reaction in real time and native temperature (George et al., 1986; Matsumura et al., 2014). Like stopped-flow, RFQ uses two drive syringes to displace a set amount of solution A and solution B. Once mixed, the mixture is aged for a set time (minimum 13 milliseconds) and then the shot is ejected into a glass funnel attached to a custom XAS cuvette filled with liquid ethane at ≤ -140° C. The frozen sample is packed into the cuvette with the whole assembly sitting within a Teflon block cooled with liquid nitrogen to ≤ -100° C. Once packed, the frozen samples are stored in liquid nitrogen until analysis (Figure 2.4).

Figure 2.4 RFQ setup using Quench Flow-3 apparatus configured and manufactured by Kintek at Reed College (left) and schematic (right).

2.5 Fourier transform infrared spectroscopy (FTIR) of Cu(I)CO

Fourier transform infrared spectroscopy (FTIR) measures the interaction of molecules with electromagnetic radiation in the infra-red (IR) region. Lower energy IR radiation can interact with the molecular vibrations of the molecule and excite them to a higher vibrational level. When an IR active sample is exposed to IR radiation, some of the radiation will be absorbed. An FTIR spectrometer measures how much light is absorbed by the sample. Unlike a UV/Vis spectrometer, where the sample is exposed to one wavelength of radiation at a time, FTIR spectrometers expose the sample to a beam of radiation containing many wavelengths. During an FTIR scan the beam changes to many different combinations of frequencies. In a standard FTIR spectrophotometer the light from the source is directed towards the beam splitter, which reflects half of the light to the fixed mirror and transmits the other half to the moving mirror (Figure 2.6). The reflected beams from both the mirrors pass through the beam splitter to the detector. The signal recorded is sinusoidal and is called an interferogram.

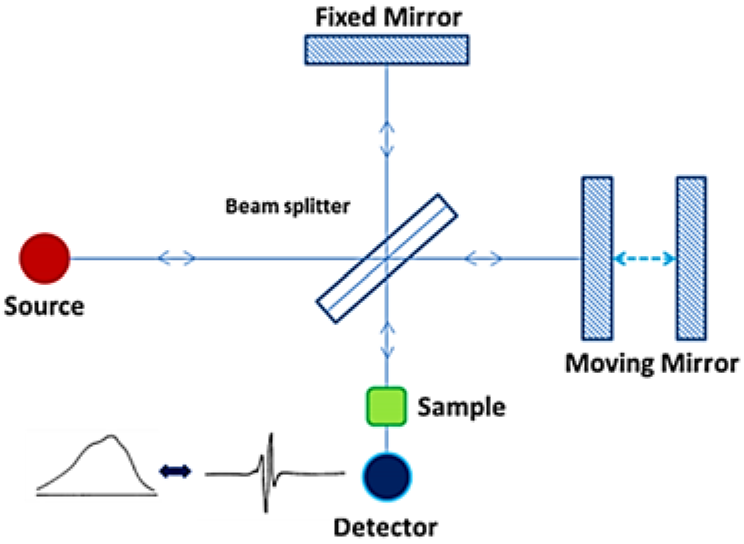

Figure 2.6 Typical setup of an FTIR experiment.

The interferogram must be converted using the Fourier transform (FT) equation (5). The Fourier transform converts one domain (displacement of the mirror in cm) into its inverse domain (wavenumbers in cm^{-1}). The mathematical expression of FT can be expressed in the following equation, where ω is the angular frequency and x is the optical path difference. F(ω) is called the FT and f(x) is the interferogram.

$$F(\omega) = \int_{-\infty}^{+\infty} f(x)e^{i\omega x}dx \tag{5}$$

The equation for the inverse FT is below:

$$f(x) = \frac{1}{2\pi}\int_{-\infty}^{+\infty} F(\omega)e^{-i\omega x}\, d\omega \tag{6}$$

The resulting spectrum contains peaks, also called absorbance bands, which correspond with specific vibrations produced by exposure to IR radiation of atoms within the sample. IR active molecules must produce vibrations and have a change in dipole moment with respect to distance that is non-zero. This requires that the change in dipole moment divided by change in bond distance produces a non-zero number. If the resulting vibrations satisfy this requirement, the molecule is considered to be IR active and will produce the bands seen in the resulting spectrum. The spectrum is plotted as infrared intensity versus wavelength (or frequency) of light. The intensity, plotted on the y-axis, is correlated to the concentration of molecules in the sample. The x-axis is generally reported as wavenumber (cm^{-1}). The relationship of frequency to wavelength and then to wavenumber is described in equations 7 and 8, where c is the speed of light (cm/sec), v is frequency in Hertz (sec^{-1}), λ is wavelength in cm and W is wavenumber (cm^{-1}).

$$c = v\lambda \tag{7}$$

$$W = 1/\lambda \tag{8}$$

The IR spectrum is often split into two regions: the functional group region (4000-1500 cm^{-1}) and the fingerprint region (1500-400 cm^{-1}). Bands in the functional group region are characteristic of specific kinds of bonds and can be used to identify whether a specific functional group is present, including CH, OH, and C=O. The wavenumber of these bands directly correlates to unique vibrations of each functional group. The width of the bands can also yield information on the number of functional groups, as higher numbers result in wider bands. Bands in the fingerprint region are highly characteristic of the molecule as a whole, and are often characteristic of molecular symmetry, or combination bands arising from multiple bonds deforming simultaneously.

The absorbance band for free carbon monoxide (CO) at 2143 cm^{-1} has been extensively characterized and shown to shift to a lower frequency when bound to most metal compounds. Briefly, molecular orbital theory explains that a synergic process occurs, whereby the σ- bond causes electron donation from CO to the metal's empty orbital, while additionally inducing π-back-donation from the d π-electrons of the metal to the antibonding orbitals of CO as shown in Figure 2.5 (Nakamoto, 2008). Ultimately, the electrons flow from the metal to a CO antibonding orbital, which weakens the CO bond and shifts the ν(CO) to lower frequencies. This allows for the monitoring of ν(CO) stretching frequency to serve as a reporter for the local metal environment.

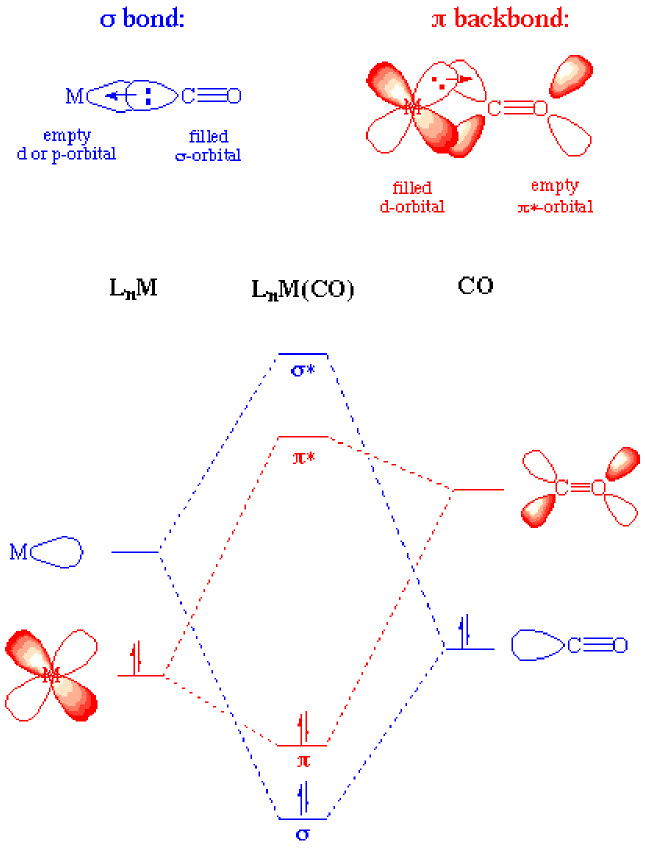

Figure 2.5 The σ- and π- bonding in metal carbonyls (Adapted from (Nakamoto, 2008))

2.6 Selenomethionine labeling as a probe for tracking copper loading and transfer

As discussed above, XAS is a bulk technique which makes analyzing copper-containing proteins with more than one metal binding site or multiple copper-containing proteins challenging. To combat this challenge, the Blackburn Lab uses selenomethionine (Se-Met) labeling of active site methionine Met(S) and cysteine Cys(S) residues in order to add a second probe, able to report copper occupancy and transfer. Specific holo and apo metal binding sites within a given protein can be clearly distinguished in the Fourier transform (FT) spectra derived from the Se EXAFS. Se-Met labeling allows a metal ion transfer to be tracked from the vantage point of Se as well as from the vantage point of the bound metal ion. The use of Se-Met labeling is extremely useful in improving the accuracy of a simulation. The parameters of the Se edge data must mirror that of the bound metal ion’s edge data, allowing some parameters to be fixed, such as scattering atom distances and coordination numbers.

This technique was first used by the Blackburn Lab in the CuA center of *Thermus thermophilus*, in order to assign Se−S(thioether) distances and thereby gain information on the Se−Cu−Cu and Se−Cu−S(thioether) angles (Blackburn et al., 1999). It was then used in collaboration with the Lu lab to determine the role of the axial Se-Met in the blue copper center of azurin (Berry et al., 2003).

As discussed above, XAS has been useful in determining the metal binding sites of Cus proteins: Met_2His with a weakly coordinating tryptophan for CusF and Met_3 for both CusB and CusA. Understanding the mechanism of metal efflux is more challenging to study, as all Cus proteins have similar metal binding sites and XAS is a bulk technique. This also makes the Cus system an excellent candidate for Se-Met labeling, because all three of the Cus proteins under investigation contain at least two ligating S-Met residues. The Blackburn Lab first used this technique to show the direct Cu(I) transfer between Se-Met labeled CusF and S-Met CusB (Bagai et al., 2008). However, this transfer only occurs when one protein is apo; no metal transfer is observed when both proteins are metal loaded. This study also shows that metal transfer occurs in both directions between CusF and CusB and proceeds to a 50% equilibrium distribution *in vitro*, suggesting a regulatory role. More recently in 2014 (Chacón et al., 2014b), the Blackburn Lab used Se-Met labeling in combination with Cu(I)/Ag(I) binding Cus proteins to establish a "switch" role for the membrane fusion protein CusB. Tracking of metal occupancy was achieved by Se-Met labeling CusB or CusF and then loading proteins with Cu(I) or Ag(I), which produced Cu(I)-loaded CusF, Ag(I)-loaded CusB, and apo CusA in the same reaction and allowed for a full account of metal transfer by a series of trimetal (Cu, Se, and Ag) XAS experiments. Firstly, this study showed that CusB and CusA cannot transfer copper ions, indicating that metal-loaded CusB does not act as a metal relay to CusA but instead functions as an "on/off switch". This result is supported by further XAS experiments which showed metal back-transfer between CusB and CusF. While these are applications of Se-Met labeling on static structures or end points of transfer experiments, XAS of Se-Met labeled proteins can be combined with RFQ sample preparation for time-resolved tracking of metal ion transfer for structural and kinetic information.

In 2018 I and others in the Blackburn Lab successfully investigated the mechanism of metal transfer between CusF and CusB by coupling Se-Met labeling of the Cu(I)-binding residues to RFQ XAS (Chacón et al., 2018). Here we labeled the two Met(S) in the metal binding site of CusF with Se-Met while CusB was unlabeled, allowing metal transfer to be determined by the decrease in the Se-Cu signal at the Se edge (Figure 2.8). As part of this study, I constructed and characterized CusF$_{(M8IM59I)}$ where the two noncoordinating Met(S) residues (M8 and M59) were mutated to isoleucine so that all Se-Met labeled ligands are metal binding, increasing Se sensitivity (Figure 2.7).

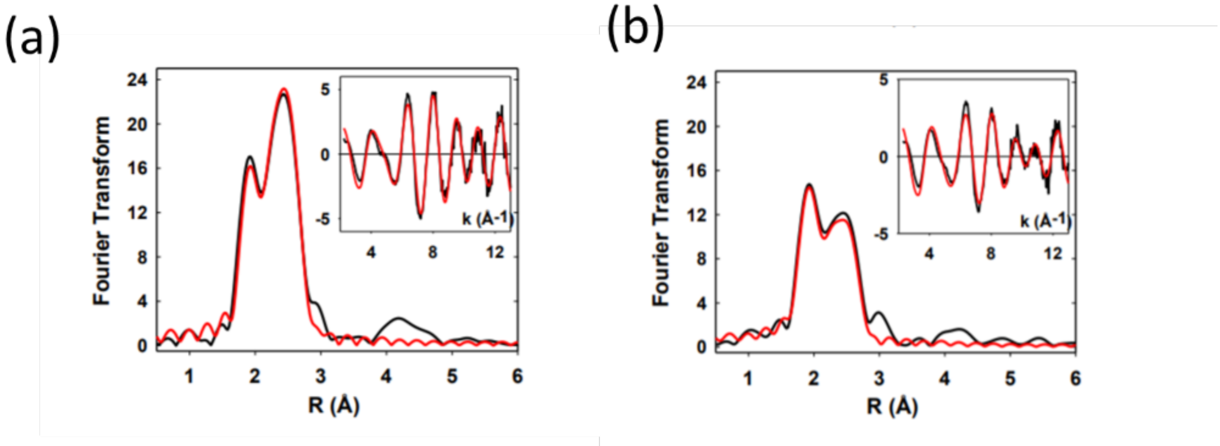

Figure 2.7 Fourier transform and EXAFS (inset) for Se K-edges for Se-Met labeled Cu(I)-loaded CusF$_{(M8IM59I)}$ (a) and Se-Met labled Cu(I)-loaded CusF$_{WT}$ (b) (Chacón et al., 2018).

The use of RFQ sample preparation at room temperature made it possible to measure copper occupancy on a millisecond timescale (15 ms to 30 s) and track the rapid copper transfer between CusF and CusB. The reaction was found to be biphasic, with a fast phase complete within 20–50 ms and a slow phase occurring on the 500 ms to 10 s time scale. The kinetic profile could be fit to a mechanism in which CusF and CusB react in a rapid step ($k \sim 1 \times 10^6$ M^{-1} s^{-1}) to form a protein-protein complex, with the Fourier transform amplitude indicating that the Cu atom is bound to one of the two Se-Met ligands in CusF. The protein-protein complex subsequently rearranges ($k = 0.3$ s^{-1}) to the final product, fully loaded CusF, with copper bound to both of the Se-Met ligands (Figure 2.8). This strongly suggested the formation of a shared ligand intermediate with Cu(I) bound to coordinating residues of both CusF and CusB.

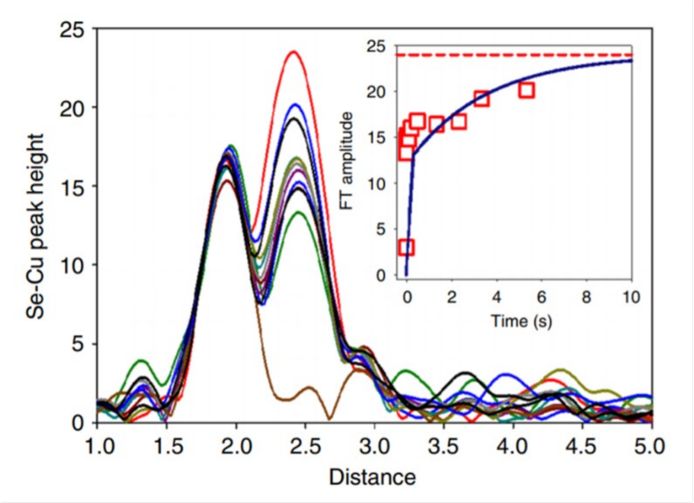

$$\mathrm{Cu(I)CusF + apoCusBNT \xleftrightarrow{k_{fast}} [CusF - Cu(I) - CusBNT]}$$

$$\mathrm{[CusF - Cu(I) - CusBNT] \xleftrightarrow{k_{slow}} apoCusF + Cu(I)CusBNT}$$

Figure 2.8 Time course of the transfer of copper from Cu(I)-loaded CusB to Se Met labeled CusF showing the increase in Se−Cu peak height in the Fourier transform of the Se K EXAFS, as Cu(I) transfers to CusF and binds to the Se atom of the Se-Met ligands. Traces from the bottom are for time points (in milliseconds) 15, 46, 114, 216, 1340, 2340, and 3340, with the final trace (red) representing the reaction end point at 30 seconds. The inset shows the Se−Cu peak height data plotted against time and fitted to a kinetic model involving initial rapid protein-protein complex formation followed by rate-limiting intramolecular metal transfer to form products as shown in equation below (Chacón et al., 2018).

In order to capture the proposed CusF/CusB shared ligand intermediate, two sets of RFQ samples were prepared at 4°C, one set mirroring a room temperature experiment (Se-Met CusF + Cu(I)-loaded CusB) and a second with the label switched to CusB Se-Met CusB + Cu(I)-loaded CusF). The proposed mechanism predicts that the shared ligand intermediate should produce an XAS spectrum which simulates a Se−Cu intensity of 0.5 Se per Cu when the label is on CusF (one out of two Se-Met ligands bound to Cu), but increases to 0.67 when the label is switched to CusB (two out of three Se-Met ligands bound to Cu). Even at 4°C the initial phase is still too fast to resolve, but the slower phase has been slowed significantly, allowing full formation of the intermediate supported by the Se-Cu amplitudes in the FT remaining constant between 26 ms and 1 s. The 100 ms intermediate complex shows a higher Se−Cu occupation when the label is on CusB and lower when the label is on CusF, as predicted by the model, where the Se-Met labeled CusF generated an intermediate involving two CusF residues (Met(S) and His(N)) and one CusB residue (Met(S)), and Se-Met labeling CusB generates a Met(S)$_3$ species, one from CusF and two from CusB (Figure 2.9).

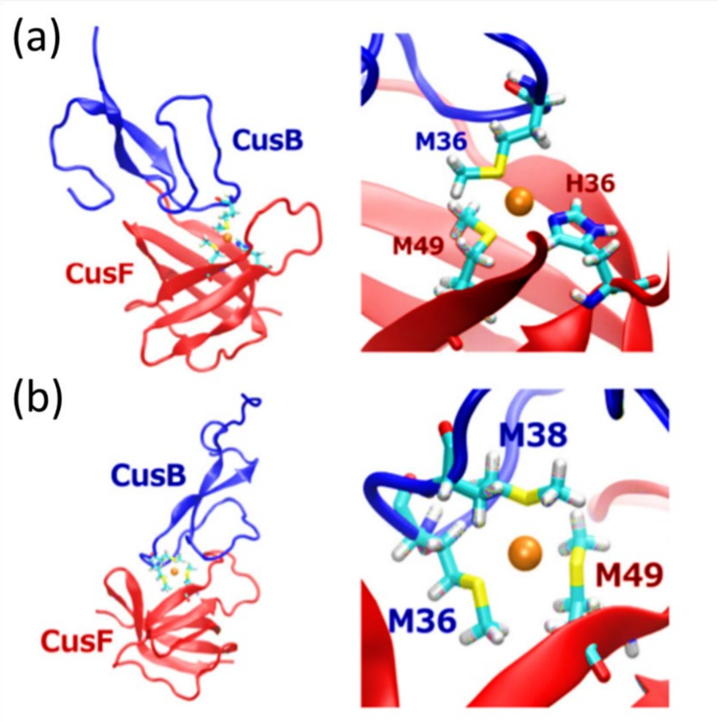

Figure 2.9 Models for the structure of the shared-ligand intermediates. (a) The MMM intermediate involving two Mets from CusB and one Met from CusF. (b) The HMM model involving one Met from CusB and a Met and a His from CusF. Structures on the left are *in silico* models of the protein-protein interactions between CusB and CusF showing the protein interface, while those on the right depict the proposed active site structures of the intermediates. The models are reproduced from coordinates determined from the QMMM studies reported in (Chacón et al., 2018; Ucisik et al., 2015).

2.7 Unnatural amino acid incorporation

Pioneered by the Schultz group and others, site-specific genetic incorporation of unnatural amino acids (UAAs) can be used to provide new probes for spectroscopic studies of proteins (Leisle et al., 2015; Wang & Schultz, 2005). The incorporation of a UAA requires engineered plasmids expressing an orthogonal aminoacyl-tRNA synthetase (aaRS)/tRNA pair with specificity for the UAA. These biorthogonal pairs can repurpose *E. coli* stop codons, ochre (TAA), opal (TGA), and amber (TAG), and instead incorporate a UAA at the specific location. Of the three stop codons, the amber codon is the least used in *E. coli* (~7%) and rarely terminates essential genes (L. Wang et al., 2006). The pDule2-pCNF plasmid encodes for one such evolved pair *Methanocaldococcus jannaschii* TyrRS/tRNAtyr (Figure 2.10). The *M. jannaschii* TyrRS/tRNAtyr pair can incorporate a variety of phenylalanine derived UAAs, with I, Br, CN, or N_3^- in the para position. L-4-cyanophenylalanine (Phe_{CN}) has been shown to function as an IR probe (Schultz et al., 2006), and used to create a new FRET pair (Miyake-Stoner et al., 2009). The same TyrRS/tRNAtyr pair can also be used to insert L-4 bromophenylalanine (Phe_{Br}), which can be used as a heavy atom for XAS. UAA incorporation must be confirmed using mass spectrometry.

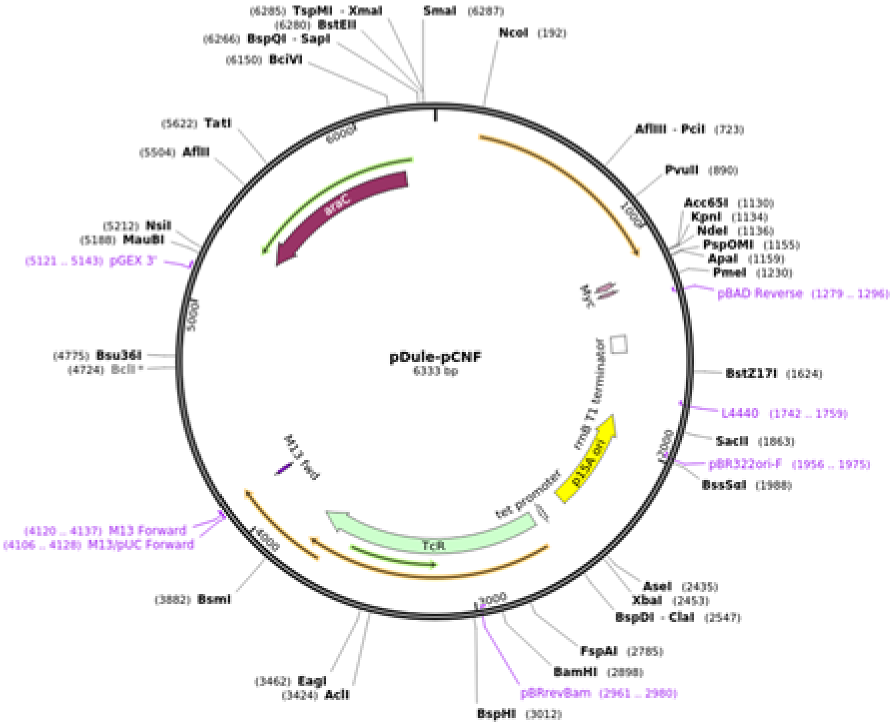

Figure 2.10 Plasmid map for pDule2-pCNF. Machinery plasmid expressing permissive pCNF synthetase and cognate amber suppressing tRNA.

CHAPTER 3: Rational design of a histidine-methionine site modeling the M-center of copper monooxygenases in a small metallochaperone scaffold

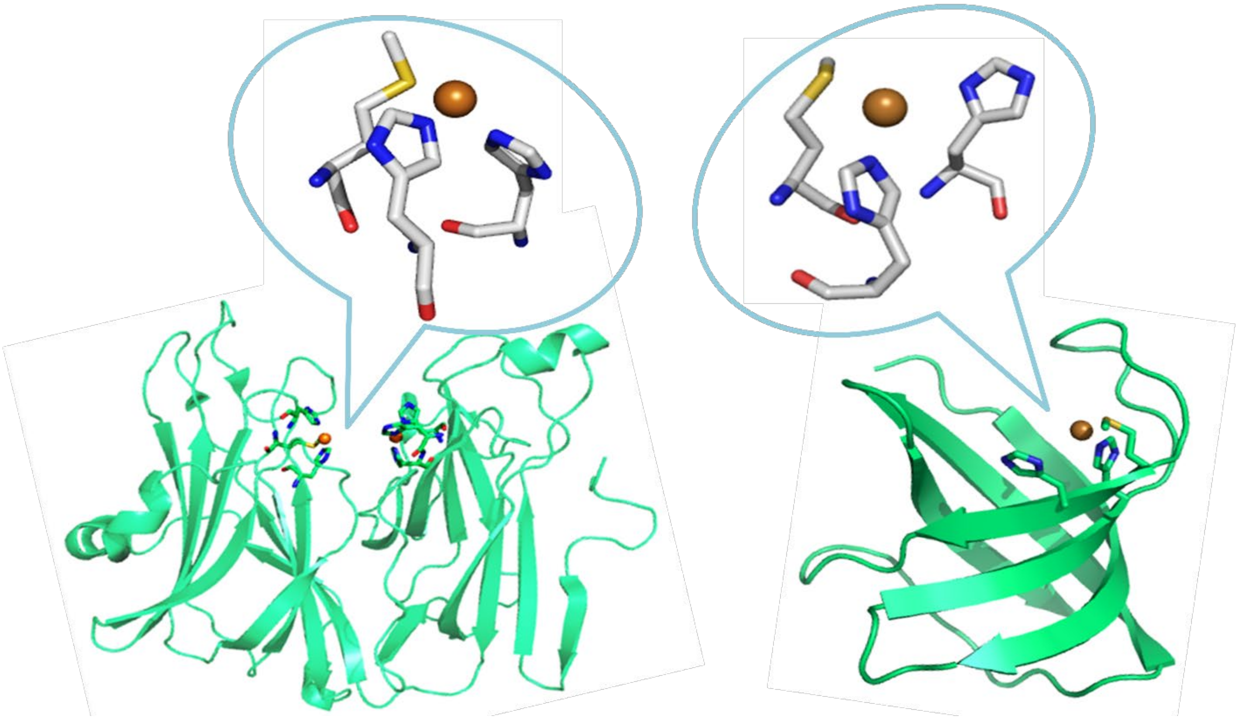

Figure 3.1 Cartoon representation of the PHM M-site model constructed in the CusF scaffold. The graphic shows an energy-minimized representation of the CusF M49H variant in a CusF M8IM59IW44A triple mutant background (right) compared with the PHM M-site (left). The energy minimized structure was obtained by mutating the WT structure (PDB: 2VB2) in Pymol. The new structure was then submitted for energy minimization to the YASARA Energy Minimization Server (Krieger et al., Proteins: Structure, Function, and Bioinformatics 77, 114-122) and the final structure rendered in PyMOL (The PyMOL Molecular Graphics System, Version 1.8 Schrödinger, LLC).

---

*Material in this chapter has been published in this or similar form in Biochemistry, and is used here with permission of the American Chemical Society.

Alwan, K. B., Welch, E. F., Arias, R. J., Gambill, B. F., & Blackburn, N. J. (2019). Rational Design of a Histidine-Methionine Site Modeling the M-center of Copper Monooxygenases in a Small Metallochaperone Scaffold. *Biochemistry*, *58*(28), 3097–3108. https://doi.org/10.1021/acs.biochem.9b00312

3.1 Introduction

Copper active sites are found in an array of essential enzymes capable of catalyzing oxidative conversions of substrates as diverse as aromatic rings, catecholamines, peptide hormones, saturated alkanes, and polysaccharides (Quist et al., 2017). The copper center is first activated via dioxygen binding, forming a Cu-dioxygen intermediate that then reacts further with the substrate via chemistry that requires a finely tuned metal binding site, capable of redox cycling. The mononuclear monooxygenases are an important class of oxygen-activating cuproproteins, which catalyze the insertion of a single oxygen atom from O_2 into the strong C-H bond of organic substrates. They include peptidylglycine α-hydroxylating monooxygenase (PHM) (Prigge et al., 2000), dopamine β-monooxygenase (DβM) (Klinman, 2006a; Vendelboe et al., 2016), its insect analog tyramine β-monooxygenase (TβM) (Hess et al., 2010; Hess et al., 2008), and the lytic polysaccharide monooxygenases (LPMO)(Walton & Davies, 2016).

Despite differing structures and substrate specificities, both PHM and DβM utilize a catalytic core made up of two nonequivalent mononuclear copper centers (Chufán et al., 2009; Prigge et al., 1997, 1999; Vendelboe et al., 2016), and react via an identical chemical mechanism (W. A. Francisco et al., 1998; Wilson A. Francisco et al., 2002; Klinman, 1996). Extensive spectroscopic (Bauman et al., 2011; Blackburn et al., 2000; Boswell et al., 1996; Chauhan et al., 2014), kinetic (Evans et al., 2003; Klinman, 1996, 2006a; Osborne et al., 2013), and computational (Bauman, Yukl, et al., 2006; P. Chen et al., 2003; P. Chen & Solomon, 2004) work on PHM suggests that one site (CuM) controls catalysis, exhibiting an unusual His_2Met ligand set, while the other site (CuH) is responsible for electron storage and transport and exhibits a His_3 ligand set. In a proposed canonical mechanism, the Cu(I)M - substrate complex reacts with oxygen to form a Cu(II)-superoxo intermediate with sufficient electrophilicity to abstract a hydrogen atom from the nearby peptide substrate (Bauman et al., 2006; Chen & Solomon, 2004; Evans et al., 2003). An X-ray structure of "oxy-PHM" (Prigge et al., 2004) has allowed a close analogue of the reactive superoxo species to be visualized as a four-coordinate, distorted tetrahedral entity containing an end-on superoxide ligand. Enzyme-bound cupric superoxo species have also been proposed as intermediates in LPMO catalysis where rapid re-oxidation of the mononuclear Cu(I) center by O2 is suggestive of the formation of an unstable

Cu(II)O2•- species (Kjaergaard et al., 2014), but spectroscopic characterization of either intermediate has yet to be achieved.

The quest for spectroscopic signatures of mononuclear copper intermediates has stimulated the synthesis of several biomimetic model compounds whose chemistry with dioxygen has been probed at low temperature. As reviewed by Tolman and coworkers (Elwell et al., 2017) a number of inorganic mononuclear cupric superoxo species have been characterized, and include both side-on (η2-)(Chen et al., 2003; Fujisawa et al., 1994), and end-on (η1-) complexes (Ginsbach et al., 2013; Kunishita et al., 2009, 2012; Lanci et al., 2007; Maiti et al., 2007; Peterson et al., 2011, 2013; Schatz et al., 2004; Tano et al., 2013; Woertink et al., 2010). Early synthons were built from 3- or 4-coordinate all-N donor scaffolds, since studies on related Cu(II)- (Lee et al., 2007) and Cu(III)-peroxo (Aboelella et al., 2006) species had shown little or no stabilization via thioether coordination. More recent work on a N_3S(thioether)-Cu(I) complex, which reacts with oxygen to form a superoxo intermediate (Kim et al., 2015), suggests that the thioether moiety may increase the electrophilic character of the superoxo with respect to H-atom abstraction. While these studies have offered great insight into the chemistry and spectroscopy of cupric superoxo species, they require the use of low temperature (-125°C) and aprotic solvents, and often exhibit a strong driving force towards formation of peroxo-bridged dinuclear complexes which lack electrophilic reactivity.

In previous work, the Blackburn Lab reported the preparation and properties of PHM variants that were designed to allow study of the M- and H-centers independently (Chauhan et al., 2014). PHM H242A bound a single Cu at the H-center while H107AH108A bound a single Cu at the M-center. More recent crystallographic studies (Maheshwari et al., 2018) have indicated conformational mobility in these copper-depleted mutants, suggesting that the single site variants may not be truly representative of the individual active sites. Notwithstanding, the ability to interrogate the individual chemistry of the two non-equivalent copper sites is an important goal in fully understanding the mechanism of PHM and its congeners, leading us to seek alternative strategies. One approach to modeling the reactivity of enzyme-active sites has made use of small peptide or protein scaffolds inside which metal binding sites can be assembled (Koebke & Pecoraro, 2018; Mann et al., 2016, 2017; Mocny & Pecoraro, 2015). This has the advantage that the protein polypeptide can provide protection from solvents and can furnish any necessary H-bonding interactions from second sphere interactions while still maintaining aqueous solubility. We have applied this approach to the PHM system via use of the CusF scaffold, a small mononuclear Cu(I) metallochaperone expressed in the *E. coli* copper export system, CusCBAF (McEvoy et al., 2012). The metal binding site of native CusF is situated in a hydrophobic pocket and ligated by two sulfurs (from methionines M47, M49), the Nε of histidine 36 (H36) and a cation-π interaction with the aromatic ring of W44 (Chakravorty et al., 2016; Changela et al., 2003, p. 200; Kline et al., 2013; Loftin et al., 2007, 2009; Xue et al., 2008). Using site-directed mutagenesis, we constructed the M49H CusF variant, along with its M47H analogue in the M8IM59IW44A triple mutant background. These engineered scaffolds provide a His_2Met copper-binding ligand set that mimics the M-center of PHM where the single Met residue in the protein is coordinated to copper. Specifically, the system holds promise for obtaining a deeper understanding of a number of attributes of PHM M-site chemistry that remain enigmatic. For example, how does substrate hydroxylation remain fully coupled to oxygen consumption even with extremely slow variants (implying that substrate binding must trigger oxygen reactivity) (Evans et al., 2006; Kline et al., 2013)? What is the role of the Met ligand, and why is it essential for catalysis (Eipper et al., 1995; Hess et al., 2010; Hess, Wu, et al., 2008; Kline et al., 2013)? Can a cupric superoxo species be isolated, and what structural features are required for its stability?

Here we report results that show that the CusF-model accurately reproduces the chemical and spectroscopic properties of the M-center. We probe details of the methionine coordination and the properties of Cu(I) and Cu(II) states in the presence of exogenous ligands such as CO and azide. We also explore the reaction chemistry of Cu(I) forms with molecular oxygen and the Cu(II) forms with chromophoric reductants. The data reveals a close structural and electronic similarity to the PHM M-center, but an unusually low reactivity towards molecular oxygen, which emphasizes the important role played by the PHM substrate complex in oxygen activation.

3.2 Materials and Experimental Details

Construction of CusF mutants. W44A M49H and W44A M47H mutations were introduced into the *CusF*$_{6–88}$ *M8IM59I trx-his6-tev* sequence (both non-coordinating Met residues mutated to

Ile) using an overlap extension polymerase chain reaction (OE-PCR). Sense and antisense oligonucleotide primers encoding ~20 bases downstream and upstream of the mutation were used for site-directed mutagenesis and paired with primers upstream and downstream of two restriction enzyme sites, HindIII and Nco1. PCR products were purified on agarose gels. Final PCR products were extracted with phenol and chloroform, digested using restriction enzymes (NEB), separated on agarose gels, purified via a Qiagen PCR kit, and ligated into the pETDuet-1 expression vector. All variants were confirmed by DNA sequencing. The resulting plasmid *pETDuet-1- CusF* was then transformed into *E. coli* BL21-(λDE3) cells.

Expression and Purification of CusF. A freshly streaked plate of BL21(DE3) cells containing *pET-Duet1-CusF* with the appropriate mutation was used to inoculate 10 ml of LB media containing 100 mg/ml ampicillin. After overnight incubation at 37°C with shaking at 250 rpm, the starter culture was used to inoculate a 1L flask of LB culture medium with 100 µg/mL ampicillin and 0.2% D-glucose. The culture was grown at 37°C until an OD_{600} of 0.6 – 0.8 was reached, at which point it was induced with 500 µM isopropyl β-D-1-thiogalactopyranoside. Growth was continued at 17 °C for 16–20 hours after which cells were harvested by centrifugation. Pellets were re-suspended in column buffer (20 mM Tris, 150 mM NaCl, 10 mM imidazole, 5% glycerol). For purification, $MgCl_2$, Dnase and protease inhibitor were added and cells were lysed using an EmulsiFlex-C3. The lysate was centrifuged at 12,000 rpm for 50 minutes to remove cell debris. The supernatant was filtered using a 0.45 µm syringe filter and then applied to Ni-NTA column, rinsed with buffer, and eluted with 250 mM imidazole. The His_6-Trx tag was cleaved using tobacco etch virus (TEV) protease during an overnight incubation at 20°C by the addition of 1 part TeV to 100 parts protein and 5 mM β-mercaptoethanol. The protein was dialyzed overnight, then reapplied to the Ni-NTA column. The flow-through represented >95% pure, apo CusF protein with the His-tag cleaved. The final product was analyzed via SDS/PAGE (8–25% gradient stained with Coomassie brilliant blue R-250) which showed a single band at the appropriate molecular weight (~10 kDa). Proteins were then dialyzed and stored in 50 mM sodium phosphate pH 8.0. Protein concentration was quantified by bicinchoninic acid assay (BCA) and, if needed, concentrated using a 3 kDa molecular weight cutoff concentrator (Amicon).

Sample Preparation. Unless otherwise stated, samples for spectroscopy and kinetics were equilibrated into a combination buffer comprising 50 mM each of formate, MES, and HEPES, adjusted to the appropriate pH using HCl or NaOH as required.

Oxidized Samples. Protein was reconstituted with $CuSO_4$ at a ratio of 2.5:1 via syringe pump (25 µl/hr). The mixture was then allowed to incubate on ice for 1 hour with stirring. Excess Cu(II) was removed by overnight dialysis in 50 mM sodium phosphate (NaP) pH 8. Holo protein was either used immediately in experiments or flash-frozen and stored in liquid nitrogen for future use. Metal-to-protein concentrations were verified by ICP-OES and BCA assay. For pH dependence, buffer exchange was achieved by a rapid 4-fold dilution of the 4-fold concentrated protein into combination buffer at the desired pH. A small protein loss was observed, but the copper to protein ratios remained at 1:1 as confirmed by ICP.

Reduced Samples. Cu(II) reconstituted protein in the buffer of choice was reduced anaerobically by addition of a 2-fold excess of ascorbate buffered at the same pH. Protein was shown to be fully reduced by the complete loss of the Cu(II) EPR signal. For protein used in re-oxidation studies, the ascorbate was removed by two cycles of desalting on spin columns (Zeba).

Stopped-Flow Spectrophotometry. Pre-weighed DMPD, syringes, argon-purged deionized water and buffer were made anaerobic by overnight storage in the anaerobic chamber. The 50 mM DMPD stock solution was prepared by dissolving pre-weighed salt in 1 ml of deionized water. This DMPD stock solution was diluted to 2 mM using deoxygenated deionized water. Stopped-flow experiments were conducted under anaerobic conditions at room temperature on a SX20 Applied Photophysics stopped-flow instrument enclosed in a Vacuum Atmospheres anaerobic chamber with oxygen levels of ≤ 1 ppm.

Analysis of stopped-flow data. DMPD undergoes one-electron oxidation to the radical cation. The DMPD radical is a chromophoric agent which absorbs strongly at 515 nm (A_{515}) and 550 nm (A_{550}) with molar absorptivity at 515 nm of 5200 $M^{-1}cm^{-1}$. The formation of the DMPD radical strongly correlates with the reduction of the copper centers making possible the measurement of copper reduction rates by monitoring the variation of absorbance at 515 nm (A_{515}) versus time. The concentration of the reduced copper was determined from the equation

$$\textit{Concentration of the reduced copper} = \Delta A_{515}/\epsilon_{DMPD} \tag{7}$$

Where ΔA_{515} is the difference in absorption at 515 nm at time t, and $\epsilon_{DMPD} = 5200\ M^{-1}cm^{-1}$. The reduced copper concentration was calculated for every time point and plotted against time using SigmaPlot 12.0. The data were fitted to a double exponential rate equation

$$A_t = A_0 + A_1(1 - e^{-k1t}) + A_2(1 - e^{-k2t}) + ct \tag{8}$$

Where A_1 and A_2 are the absorbance as a function of time for each of the two exponential time courses with rate constants k_1, k_2 respectively. A_0 is the initial absorbance at time zero. In all experiments it was found that DMPD oxidation continued in a slow, almost linear phase with coefficient c for some time after the absorbance change indicated complete reduction of the copper center.

Spectroscopic Data Collection and Processing

Azide Titrations. 2 M sodium azide (Sigma) was added via syringe pump to CusF M49H Cu(II) in combination buffer pH 5.5 at a rate of 25 µl/hr to a final azide concentration of 100 mM. Samples were stirred continuously and spectra were collected every 20 seconds on a Cary 50 UV/Vis. The data were fit to various models using the program DYNAFIT (Kuzmic, 1996).

X-ray Absorption Spectroscopy. Samples were mixed with 20% (vol/vol) ethylene glycol and measured as frozen glasses at 10 K. Cu K edge (8.9 keV) extended X-ray absorption fine structure (EXAFS) and X-ray absorption near edge structure (XANES) were collected at the Stanford Synchrotron Radiation Lightsource on beamlines 9–3 and 7–3 using a Si 220 monochromator with a φ= 90° crystal set and a Rh-coated mirror located upstream of the monochromator using a 13 keV energy cut-off to reject harmonics. Kα fluorescence was collected using a 100-element (beamline 9–3) or 30-element (beamline 7– 3) Canberra Ge array detector. A Z-1 metal oxide filter and Soller slit assembly was placed in front of the detector to attenuate the elastic scatter peak. A buffer blank was subtracted from the raw data to produce a flat pre-edge and eliminate residual Ni Kβ fluorescence of the metal oxide filter. Energy calibration was achieved by placing a Cu metal foil between the second and third ionization chamber. Data averaging, background subtraction, and normalization were performed using EXAFSPAK. The experimental energy threshold (k=0) was chosen as 8985 eV. Spectral simulation was carried out by least-squares curve fitting, using full curved wave calculations as formulated by the program EXCURVE 9.2 as previously described (Blackburn et al., 2000; Chacón et al., 2014a, 2018).

Fourier-Transform Infrared Spectroscopy. Purified CusF was concentrated to approximately 1 mM and transferred to an airtight conical vial in an anaerobic COY chamber. Samples were purged with a gentle stream of CO for 5 minutes and allowed to incubate for 10 minutes. Protein solutions (~1 mM) were loaded anaerobically into an IR cell (50 µm path length). Samples were equilibrated inside the IR sample chamber at room temperature for 15 minutes to purge water vapor and CO_2 prior to data collection. FTIR data were recorded on a Bruker Tensor 27 FTIR spectrophotometer continuously purged with CO_2-free dry air as previously described (Kline & Blackburn, 2016). One thousand scans were collected for both protein sample and buffer blank from 2250 to 1900 cm^{-1} at a resolution of 2 cm^{-1}. Spectral analysis including subtraction of the buffer-blank was performed using GRAMS AI spectroscopy software (Thermo).

Electron Paramagnetic Resonance. Electron paramagnetic resonance spectra were measured on a Bruker Elexsys e500 spectrometer with the following experimental conditions: frequency 9.63 GHz, T = 100 K, microwave power 20 mW, gain 10 dB, modulation amplitude 10 G and sweep time 84 seconds. To determine the relative concentrations of paramagnetic copper in a given sample, a series of standard solutions containing 150–600 µM Cu(II)-EDTA in 50 mM Hepes buffer, pH 7.5 was measured to create a calibration curve. The concentrations of paramagnetic copper were determined by double integration compared to the standard curve. Spectral analysis was performed using GRAMS AI spectroscopy software (Thermo). EPR spectra were simulated using EASYSPIN (Stoll & Schweiger, 2006).

3.3 Results and Discussion

The purpose of this study was to develop an aqueous model system which could mimic the M-center of the mononuclear monooxgenases, leading ultimately to a deeper understanding of the underlying reaction chemistry of this active site. A number of methodologies exist for engineering single site constructs, all of which offer both promise and potential pitfalls. For example, our laboratory has already advanced the study of the H242A (M-site empty) and the H107AH108A (H-site empty) single site mutants which in solution have ‘native-like’ properties.

However, other mutants (H107A, H108A) that lose copper from the H center *in crystallo* exhibit "non-native" conformational mobility (Maheshwari et al., 2018), raising the possibility that single site copper loss may lead to non-native conformations. Constructs that express only the M-site sub-domain may be a possible route to M-site reactivity given that limited proteolysis using lysC cleaves the inter sub-domain linker at K219 (Kolhekar et al., 1997). However, single sub-domain constructs could be structurally compromised on account of their hydrophobic inter domain interface and have not yet been reported. As an alternative, the present paper describes the rational design of an M-site model containing the His2Met ligand set engineered into the CusF protein scaffold which we are evaluating, alongside other approaches, for its ability to provide fundamental information of the chemical properties of the His_2Met ligand set.

For the reduced monooxygenases, parameters to mimic include coordination by the His_2Met ligand set provided by residues H242, H244, M314 for PHM, the presence of an unusually weak Cu(I)-S(Met) bond, and the ability to bind and/or activate exogenous diatomics (CO,O_2). A different coordination has routinely been observed for the oxidized forms of PHM (Blackburn et al., 2000) and DβM (Blackburn et al., 1991) where the Met ligand is displaced, and water and/or other exogenous ligands occupy vacant equatorial positions of a tetragonal coordinate structure. For example, the oxidized M site is known to bind azide, nitrite, and peroxide *in crystallo* (Chufán et al., 2010), and the latter has been postulated as an intermediate in the reaction pathway. Because the model does not yet have the capability to bind a substrate, our initial studies focus on validating the structural, spectroscopic and reactivity markers of the CuM active site.

Reduced Forms. CusF M47H and M49H variants each bind one equivalent of cuprous ion to form 1:1 Cu(I) derivatives. The coordination chemistry of these Cu(I) forms was studied by X-ray absorption spectroscopy (XAS). Figure 4.2 shows the Fourier transform and extended X-ray absorption fine structure (EXAFS) of ascorbate-reduced CusF M49H and M47H in combination buffer pH 5.5. Both reduced His_2Met variants produce spectra similar to that previously reported for the reduced M-center of PHM, with the best fit to the experimental data modeled by two N(His) at 1.96 Å and one S-Met ligand with Cu-S = 2.25 - 2.28 Å, respectively (Table 4.1). This compares with values for Cu-N(His) and Cu-S(Met) of 1.98 Å and 2.18 Å respectively for the isolated M-center reported for the H107AH108A PHM variant (Chauhan et al., 2014), and 1.92

Å and 2.24 Å reported for the WT PHM (Blackburn et al., 2000). As noted earlier, recent crystallographic studies on PHM variants lacking copper in the H-center show altered structural features at the M-center (Maheshwari et al., 2018), and, in one isoform of the H108A variant, show a closed conformation with a single copper ion coordinated by residues from H and M. Thus, while recognizing that the WT has both copper centers occupied, the Cu-S(Met) bond length of WT is a better indicator of similarities, and clearly shows a closer correspondence between model and enzyme. Absorption edge data (Figure 4.2, bottom) shows edge features in the region 8983 eV as expected for 3-coordination, but with some differences in geometric or electronic structure.

The value of the Debye Waller (DW) factor ($2\sigma^2$, Table 4.1) for the Cu-S(Met) interaction is also of interest. In WT PHM and DβM the Cu-S DW is unusually large and variable, simulating in the range 0.012 – 0.025 Å^2. The large DW for the enzyme has been suggested to arise from either two conformations at the M-center involving Met-on and Met-off forms (only one of which is active), or alternatively, scaffold-based protein dynamics that create a specific protein architecture and a fluxional Cu-S bond which might couple with other specialized vibrational modes involved in H-tunneling (Bauman et al., 2011; Bauman, Jaron, et al., 2006; Kline & Blackburn, 2016). While these suggestions are elegant, the finding that the model also exhibits a large DW for Cu-S(Met) at temperatures close to 10 K establishes that this is a property of the ligand set, rather than a property induced by the PHM scaffold. Sufficient data exists to compare Cu-S(Met) DW values across a series of 3-coordinate CusF and CusB His$_x$Met$_y$ ligand sets. In this series, Cu-S(Met) DW factors range from 0.007 Å2 for the Met$_3$ site of CusB (Chacón et al., 2014b), to 0.011 Å2 for the HisMet$_2$ site of WT CusF (Loftin et al., 2007) to 0.023 Å2 for the His$_2$Met site of the CusF M49H model (this work). A plausible explanation for this trend may be that the Cu-S(Met) bond is inherently fluxional: when present together with two other Met residues in the Met$_3$ ligand set, the dynamics may favor the reversible dissociation of any one Cu-S, but would leave the other two tightly coordinated with a low average DW. For the HisMet$_2$ case the stronger donor His ligand would remain coordinated, while one out of the two Met ligands would be in flux leading to a larger DW. In the His$_2$Met case the Met ligand would always be fluxional. This argument also explains why Met residues often line potential transport pathways in importers and exporters such as CTR1 (De Feo et al., 2009; Jiang et al., 2005; Rubino et al., 2010), CusA (Su et al., 2011) and CopA (Gourdon et al., 2011a; Mattle et al., 2015), since a single Cu-Met interaction provides a balance between selective binding and kinetic lability.

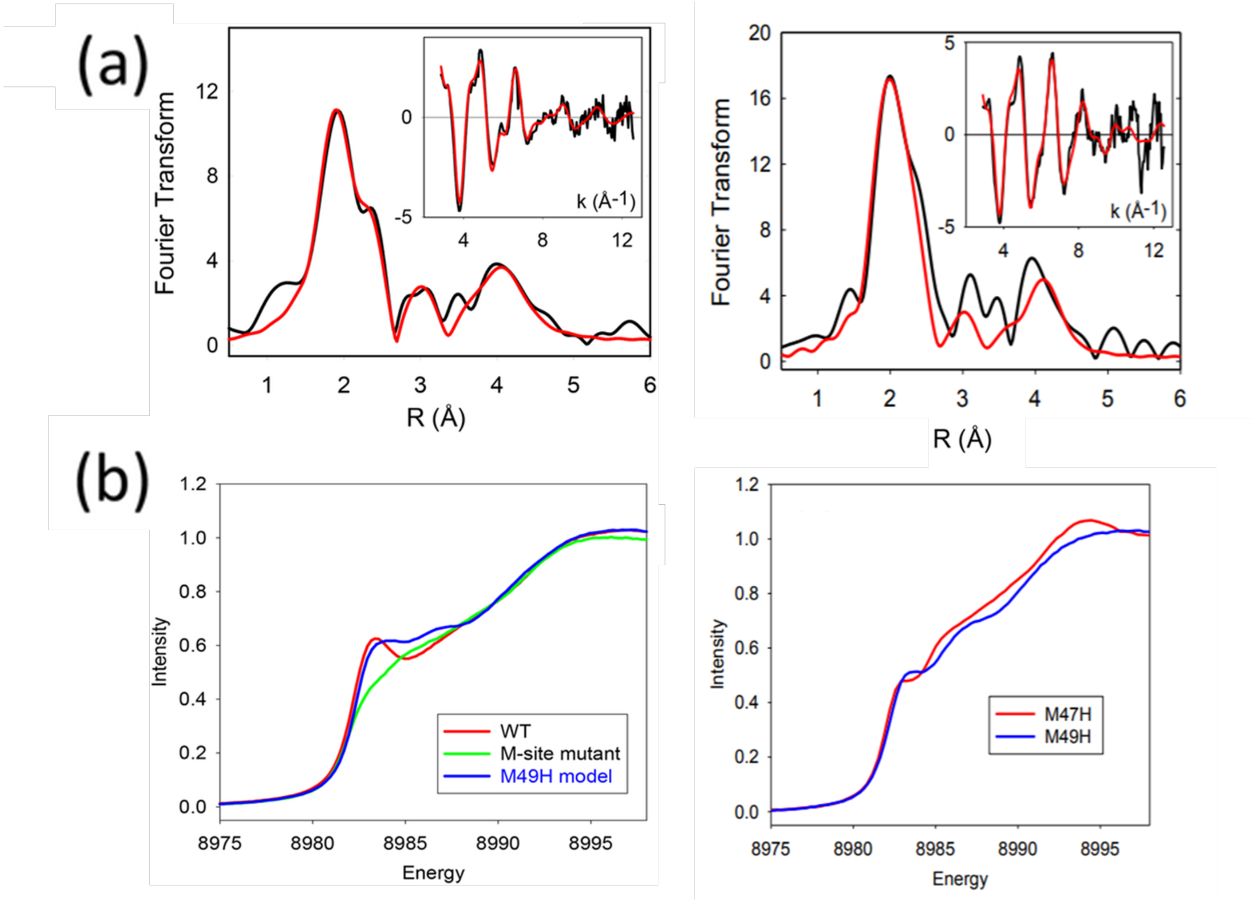

Figure 3.2 (a): Fourier transform and EXAFS (inset) for the ascorbate-reduced Cu(I)-M49H (left) and M47H (right) PHM M-site model. Black traces represent experimental data while red traces are simulations using EXCURVE 9.2. The parameters used in the fits are listed in Table 3.1. (b) Cu K absorption edges for the model compared with those of the WT enzyme (M-site and H-site metallated) and its H107AH108A variant (M-site only metallated): blue trace, M49H model, red trace WT, green trace M-site PHM variant (left) and CusF M49H and CusF M47H: blue trace, M49H model, red trace, M47H model (right).

Carbon Monoxide Binding. Carbon monoxide (CO) binding to reduced copper centers generates Cu(I)carbonyl complexes that, with few exceptions, exhibit 4-coordinate tetrahedral coordination. Since CO is a dioxygen analogue, CO binding is often used as a surrogate for O_2 reactivity, and CO has been shown to bind both the reduced M-center of PHM (Jaron & Blackburn, 1999; Kline & Blackburn, 2016) and the reduced form of DβM (Blackburn et al., 1991), forming carbonyls with stretching frequencies of 2093 cm^{-1} and 2089 cm^{-1} respectively. The ability of reduced CusF M49H and M47H to also form CO adducts would be indicative of analogous chemistry, and was tested using Fourier transform infrared spectroscopy (FTIR). Figure 3.3 shows that both the reduced M47H and M49H model systems produce a v(CO) peak indicating the formation of a carbonyl. The stretching frequency of an exogenous π-acceptor ligand such as CO, coordinated to a metal, is dependent on the degree of back-bonding from filled metal d-orbitals into the empty π*- antibonding orbitals of the CO ligand. The degree of back-bonding, in turn, is influenced by the donor strength of the endogenous protein ligands. Based on a previously established library of Cu(I)carbonyl stretching frequencies, Cu(I) carbonyls are known to have a stretching frequency range of 2012 - 2045 cm^{-1}, where the upper range is typical of rare 3-coordinate His_2CO synthons (Park et al., 2014) and the latter is the lowest frequency observed in the His_3CO ligand set of arthropodal hemocyanins (see reference (Blackburn et al., 1990)). The trend in decreasing ν(CO) with increasing donor strength is exemplified by comparison of the WT PHM M-site carbonyl (2092 cm^{-1}) with its M314H variant (2075 cm^{-1}), where replacement of thioether with histidine results in a 17 cm^{-1} downshift (Kline & Blackburn, 2016).

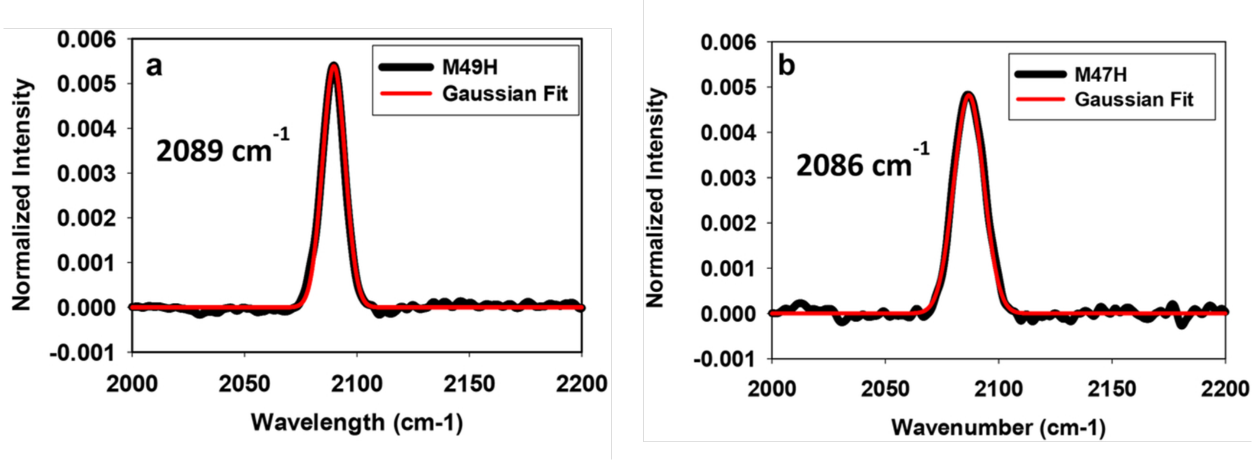

Figure 3.3 Fourier transform infrared spectra of the CO complexes of the PHM M-site models. (a) Cu(I)M49H-CO, (b) Cu(I)M47H-CO. Peaks were fit to either one or two Gaussian functions with frequencies and line widths as reported in the text.

Both CusF His_2Met models bind CO within the His_2Met ligand set range, with a v(CO) of 2086 and 2089 cm^{-1} for CusF M47H and M49H, respectively. The peak shape of both the M47H and M49H carbonyls was characterized with Gaussian peak fitting. M49H carbonyl fits to a single peak, with a width at half height (FWHH) of 11.8 cm^{-1}. The M47H carbonyl, when fit to a single peak, gave a larger FWHH value of 15.5 cm^{-1}, but could also be fit by two gaussians with FWHH values (11 cm^{-1}) that matched M49H-CO. These data suggest that M49H carbonyl is a single species, while the M47H carbonyl may form two conformers.

The coordination chemistry and Cu-O bond angle of the His_2Met carbonyls was further investigated using XAS. Figure 3.4a (left) shows the Fourier transform and EXAFS for the M49H carbonyl with absorption edge comparisons in Figure 3.4b (left), while Figure 3.4a and 3.4b (right) show the EXAFS and absorption edges of the M47H Cu(I)-carbonyl. Metrical parameters used in the simulations are given in Table 3.1. The experimental data can be modeled by Cu-C bond distances of 1.82 – 1.84 Å, with a Cu-C-O angle close to linearity and a Cu-S(Met) distance of 2.32 – 2.34 Å. The Cu(I)-His_2Met carbonyls are expected to be four-coordinate with addition of the CO ligand, and the ~0.07 Å increase in Cu-S bond length is consistent with the increase in coordination number. Both CusF His_2Met carbonyls compare well with metrical parameters (Cu-C = 1.80 Å with a ∠Cu-C-O = 179°) previously reported for the isolated M-center of the H107AH108A PHM variant, although the 2.26 Å Cu-S(Met) distance is significantly shorter (Chauhan et al., 2014). The carbonyl parameters are also consistent with those reported for WT PHM, although the latter are extracted from data on samples that have both Cu sites occupied. While both CusF His_2Met carbonyls appear structurally identical on the basis of XAS analysis, the M49H carbonyl is electronically more similar to the enzymes with a stretching frequency only 3 wavenumbers less than PHM, and identical to DβM.

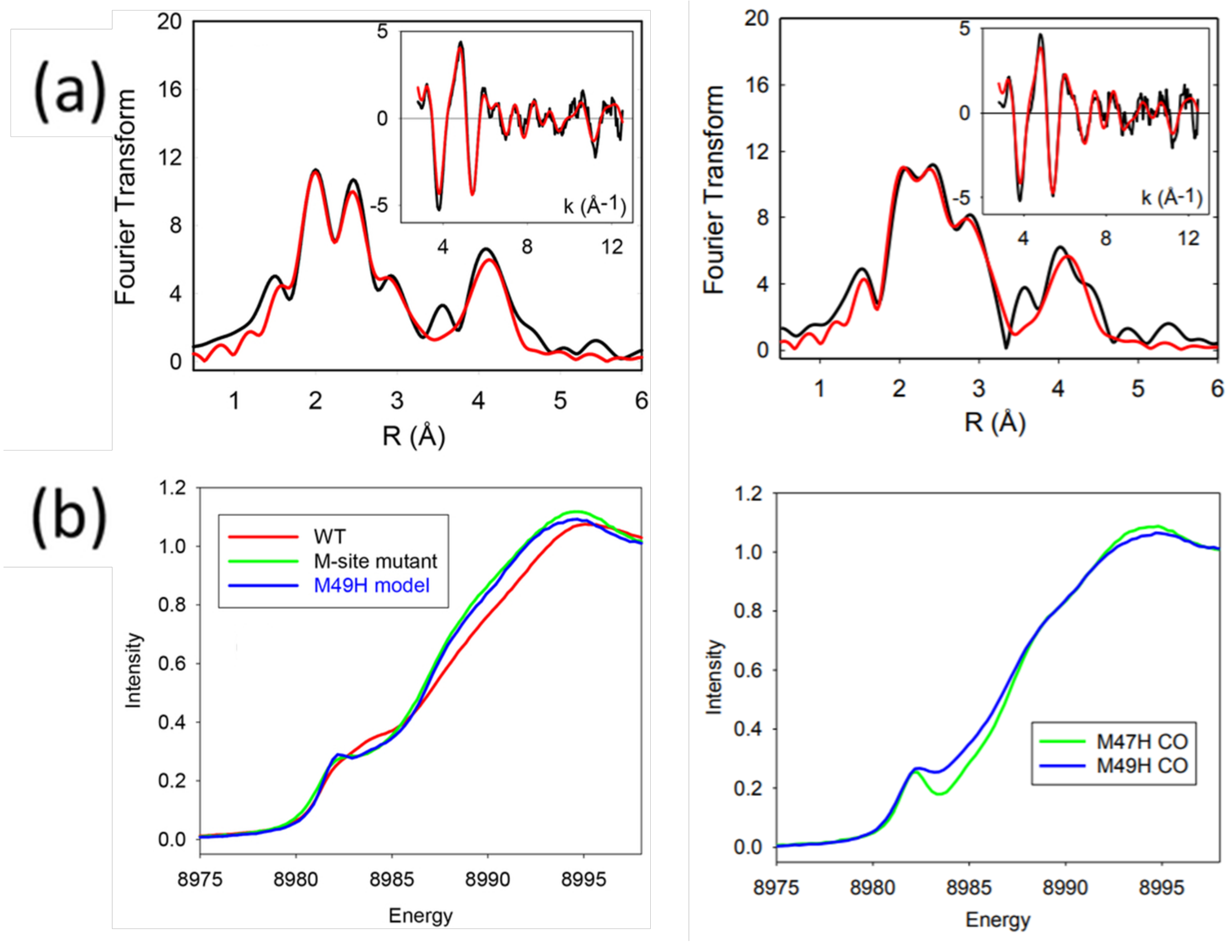

Figure 3.4 (a) Fourier transform and EXAFS (inset) for the Cu(I) CusF-CO complex, M49H (left) and M47H (right). Black traces represent experimental data while red traces are simulations using EXCURVE 9.2. The parameters used in the fits including are listed in Table 3.1 and include metrical details of the coordinated CO ligand determined from multiple scattering analysis. (b) Cu K absorption edges for the model CO complex compared with those of the WT enzyme (M-site and H-site metallated) and its H107AH108A variant (M-site only metallated): blue trace, M49H model, red trace WT, green trace M-site PHM variant (left) and M49H model complex compared to the M47H complex (right).

The M49H carbonyl was further investigated for structural and electronic changes as a function of pH, using XAS and FTIR respectively. Over the pH range 4 - 10 the overall coordination chemistry of the Cu(I) site was unchanged, with the best fit to experimental data modeled by 2 Cu-N(His) bonds at 1.99(1) Å, a single S(Met) bond at 2.33(1) Å, Cu-C at 1.82(2) Å and a linear Cu-C-O angle. All M49H carbonyls produced FTIR spectra with a peak centered at 2089 cm^{-1}

and width at FWHH of 11 cm^{-1} indicating the carbonyl complex is pH independent (Figure 3.5 and Table 3.2).

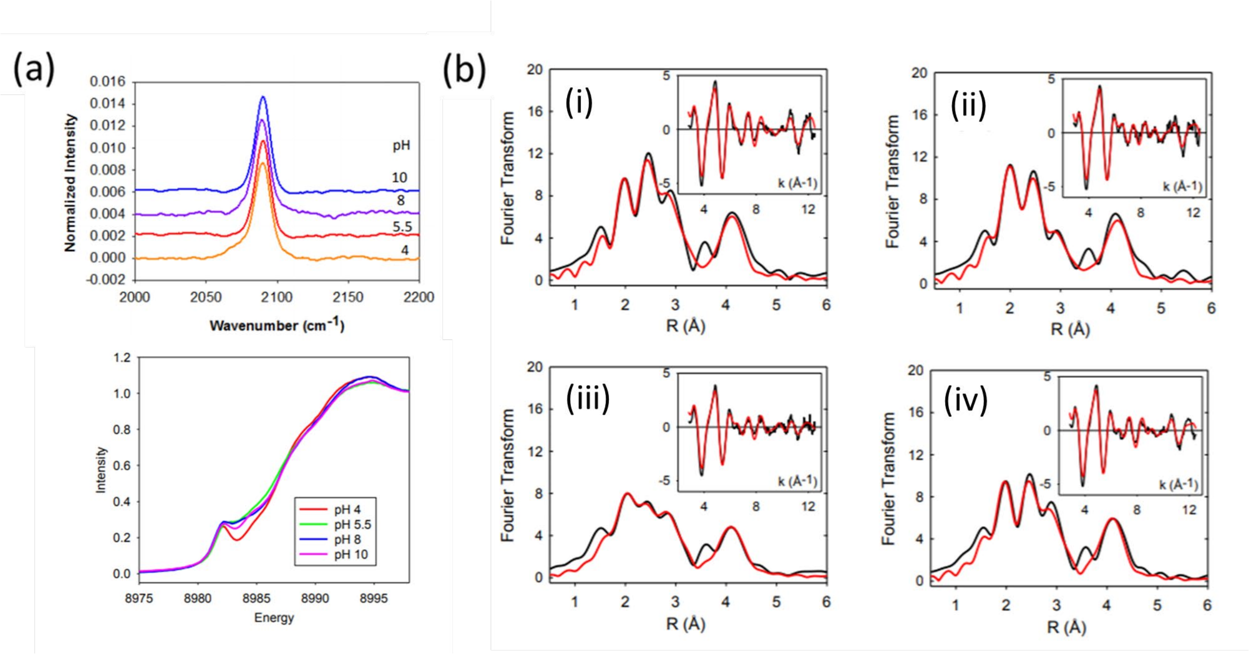

Figure 3.5 (a) pH dependence of the FTIR spectra (top) and x-ray absorption edges (bottom) of the M49H-CO complex in the pH range 4 – 10. (b) pH dependence of the EXAFS of the M49H-CO complex. (i) pH 4 (ii) pH 5.5 (iii) pH 8 (iv) pH 10. Parameters used in the fits (red traces) are listed in 3.2.

As previously discussed, in both WT PHM and the CusF His_2Met models the S-Met DW factor is large and variable, the latter due in part to large errors associated with simulating a very weak signal. The CusF M49H carbonyl provides an additional opportunity to define the origin of the large DW factor observed in the His_2Met ligand set. The M49H carbonyl produces a single peak in the FTIR establishing a single 4-coordinate species, with the EXAFS analysis predicting a contribution from 1 Cu-S with a correspondingly large DW between 0.012 and 0.023 $Å^2$. Further, this single species remains structurally identical across the full pH range. This, in turn, provides strong evidence for a single Met-on configuration, since an equilibrium between Met-on and Met-off forms of the carbonyl must lead to two distinct peaks (or at least to peak broadening) in the FTIR. Therefore, we conclude that the large DW factors are indeed the result of fluxional Cu-S(Met) dynamics as suggested above for the WT protein. While the CusF M49H model carbonyl stretching frequency matches that of the PHM M-site carbonyl in the absence of substrate, the binding of substrates to the enzyme causes an additional drop in the ν(CO) in a substrate-dependent fashion, with acetyl-YVG dropping the frequency to 2062 cm^{-1} (Kline & Blackburn, 2016). The 30 cm^{-1} red-shift implies a large increase in the electron donating power of the CuM ligand set induced by substrate binding and signals electronic activation of Cu(I)-bound diatomics, suggesting a plausible mechanism for substrate triggering of catalysis. Notwithstanding, the structural origin of the substrate-induced ν(CO) downshift is unclear since EXAFS data show no changes on substrate binding. The crystal structure of PHM reveals that the M-site ligand H242 forms a strong H-bond (2.8 Å) between its Nε imino group and the amide oxygen of the side chain of Q272. In the presence of substrate, an additional slightly longer interaction forms between H242 Nε and the substrate carboxy terminus. Taken together, these interactions suggest a protein-mediated deprotonation of the imidazole ring of H242, which is enhanced on substrate binding and could provide CO/O_2 activation. The M49H model provides some insight into this hypothesis. WT CusF H36 forms a weak 3.3 Å H-bond with its own main chain amide O, and although no structure exists for CusF M49H, inspection suggests no strong H-bonding ligand within H-bonding distance of the H49 distal N in this variant. We can therefore conclude that the 2089 cm^{-1} frequency represents a non H-bonded conformer which, in turn, would imply that in solution the 2092 cm^{-1} band in PHM is also a non H-bonded form. This raises the possibility that substrate binding induces the strongly H-bonded form observed in the crystal structures of PHM, leading to the observed drop in ν(CO).

Oxidized Forms. CusF M49H binds one equivalent of cupric ion to form a Cu(II) derivative. We investigated the properties of this species using XAS, EPR and exogenous ligand binding. Figure 3.6 shows the Fourier transform and EXAFS for oxidized CusF M49H. When simulated, the best fit to experimental data was obtained using two histidines and two water-derived ligands, with distances consistent to those reported for the oxidized CuM site of PHM (Blackburn et al., 2000) (Table 3.1). In complete agreement with EXAFS analysis of the oxidized enzymes, CusF M49H shows no contribution from the S-Met ligand, further supporting CusF M49H as a structural model for the M-site PHM.

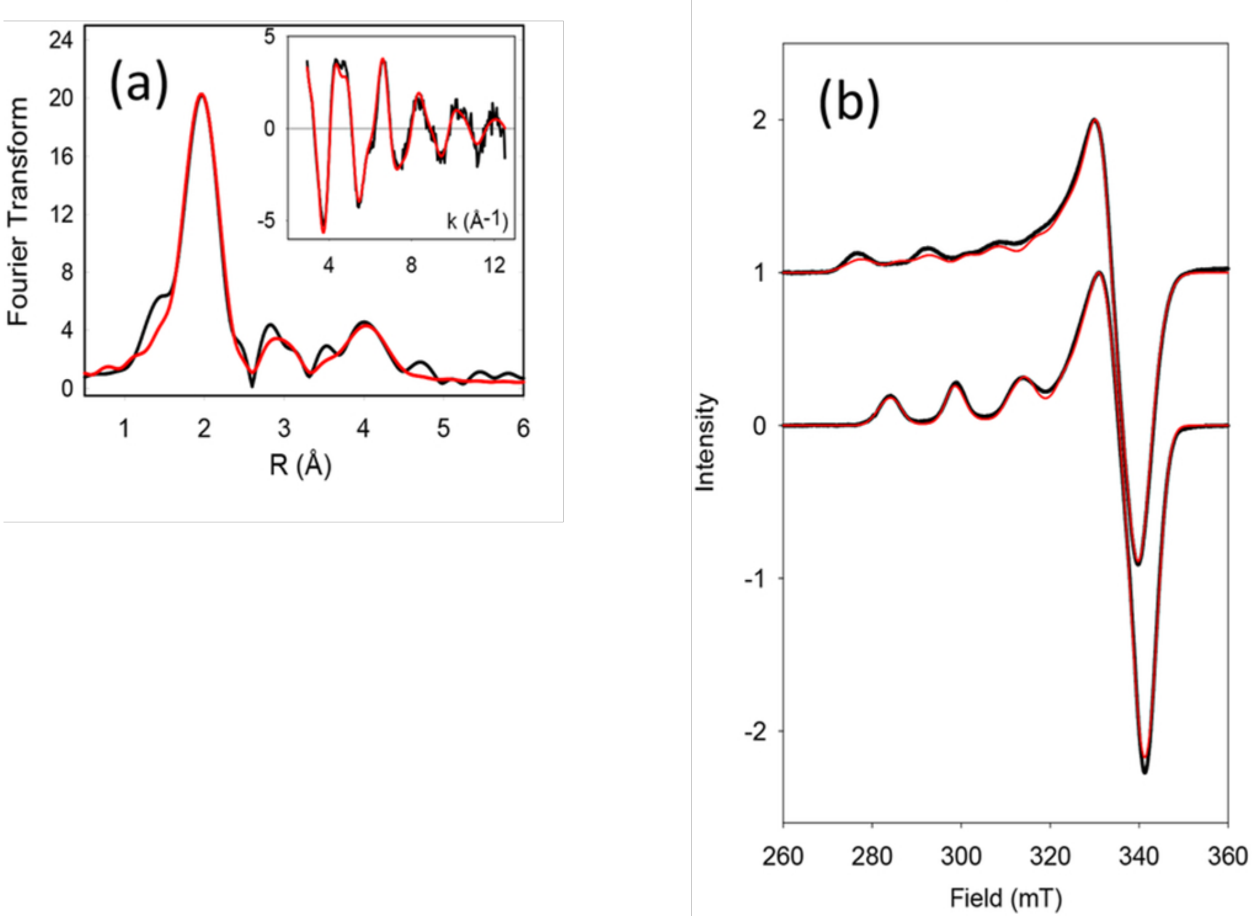

Figure 3.6 (a) Fourier transform and EXAFS (inset) for oxidized Cu(II)-M49H PHM M-site model. Black traces represent experimental data while red traces are simulations using EXCURVE 9.2. The parameters used in the fits are listed in Table 1. (b) X-band CW EPR spectra of the oxidized M49H PHM M-site model (top trace) and its azido derivative (bottom trace) determined at pH 5.5. Black traces are experimental data while red traces are simulations using EASYSPIN. The oxidized model was simulated by two components in a ratio of 1:0.3, with g and A values for component 1: gx=2.049, gy=2.076, gz=2.301, Az=481 MHz; and for component 2: gx=2.062, gy=2.084, gz=2.238, Az=472 MHz. The azido species also exhibited a two component fit in the ratio 1:0.25 with g and A values for component 1: gx=2.041, gy=2.068, gz=2.253, Az=476 MHz; and for component 2: gx=2.029, gy=2.107, gz=2.269, Az=390 MHz. Spectra were collected at a temperature of 100 K, microwave frequency 9.688 GHz, 100 Khz modulation, 10 G modulation amplitude, 20 mW microwave power and 1000 G sweep width with the field centered at 3100 G.

Oxidized CusF M49H exhibits an EPR spectrum that has contributions from two Cu(II) species which vary in a pH-dependent fashion (Figure 3.7 (left)). Also of note, spin quantitation against a Cu(II)-EDTA standard shows that the amount of EPR-detectable copper is also pH dependent, decreasing to less than 50% above pH 5 (Table 3.3 and Figure 3.7 (right)). Taken together, the data suggest an equilibrium between monomers and hydroxy-bridged dimers formed by ionization of one or more coordinated solvent molecules. Attempts to confirm the presence of dimers using size exclusion chromatography were unsuccessful due to copper dissociation on the column.

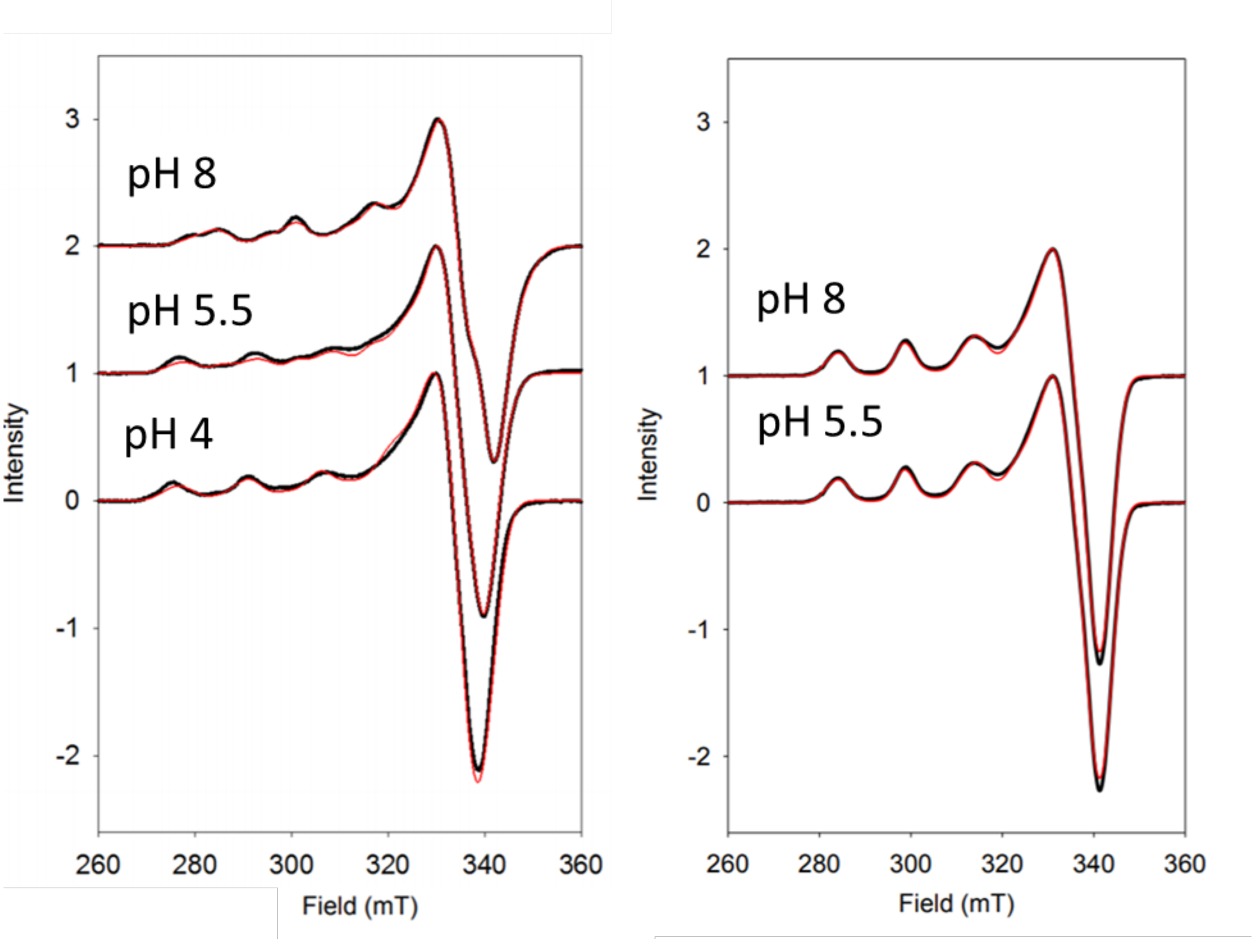

Figure 3.7 pH dependence of the EPR spectra of the M49H Cu(II) (left) and Cu(II)-azido (right) complexes. Black traces are experimental data, red traces are simulated spectra using EASTSPIN. Parameters used in the fits are given in Table 3.3. Spectra were recorded at a temperature of 100 K, microwave frequency of 9.688 GHz, 100 Khz modulation, 10 G

modulation amplitude, 20 mW microwave power and 1000 G sweep with the field centered at 3100.

Azide binding has been used as a reporter ligand for the oxidized copper centers in type 2 copper proteins since it gives rise to a LMCT band around 400 nm (Blackburn et al., 1984; Dooley & Golnik, 1983; Fee & Gaber, 1972). The Cu(II) form of CusF M49H also binds azide, generating a species that elicits close to 90 percent EPR detectable Cu(II) consistent with formation of mononuclear azido adducts that resists dimerization. The azido complex gives rise to the expected LMCT band at 390 nm (Figure 3.8), which can be titrated to yield a formation curve best fit by a single azido species with KD=3.4 mM. This chemistry is typical of type 2 Cu(II) sites in proteins, and closely resembles published PHM (Chen et al., 2004; Chufán et al., 2010), and DβM (Blackburn et al., 1984) reactivity.

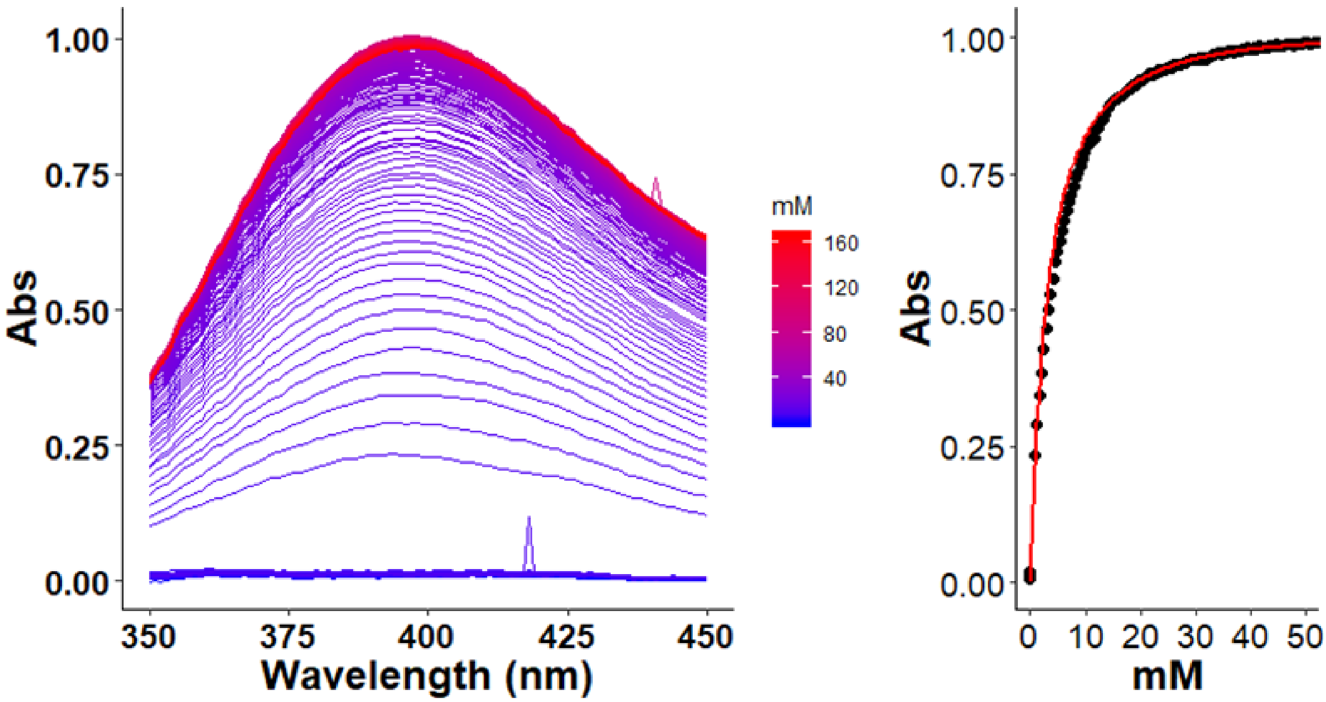

Figure 3.8 Titration of the oxidized M49H PHM M-site model with azide at 390 nm. The right panel shows a fit to the experimental UV/vis data modeled by a single Cu(II)-azido adduct with K_D = 3.4 mM.

Oxygen Reactivity. The oxygen reactivity of the reduced form of CusF M49H was tested in two series of experiments. The first series examined the rate of oxidation of ascorbate-reduced M49H with molecular oxygen, using an oxygen electrode. All excess reductant was first removed by two cycles of desalting in spin columns. The ascorbate-free anaerobic Cu(I) complex was then added to an oxygen-saturated solution of combination buffer pH 5.5, and the oxygen consumption monitored. No oxygen was consumed in this experiment, indicating a remarkable lack of reactivity. When the experiment was repeated with the carbonylated ascorbate-free protein, a similar lack of reactivity was observed. In the second series, we tested the ability of the M49H model to undergo a simple redox turnover reaction by adding sub-stoichiometric amounts of the oxidized protein to oxygenated buffer in the presence of excess ascorbate. Here the reduced Cu(I) form of the protein could form by ascorbate reduction and subsequently react with oxygen to regenerate the Cu(II) form in a catalytic redox cycle. Again, no reactivity was observed. Adding the PHM substrate dansyl-Tyr-Val-Gly to this solution did not lead to observable oxygen consumption, as expected, on the basis that the model is not yet designed to bind a peptide substrate. Therefore the Cu(I)-His2Met ligand set is unreactive to molecular oxygen in agreement with the substrate-triggering of activity exhibited by the ES complex of PHM.

Reduction by N,N'-dimethyl phenylenediamine (DMPD). DMPD is a chromophoric reductant that has been shown to support substrate hydroxylation in PHM and DβM (Li et al., 1994), and has been used previously to investigate the rates of reduction of the copper centers in PHM (Chauhan et al., 2016). We investigated the rate of reduction of the Cu(II)-M49H model by DMPD using stopped flow spectrometry. The stopped flow trace and rate of reduction of the Cu(II)-M49H model is shown in Figure 4.9. The data were fit by non-linear regression to a rate equation which describes the process as a combination of fast and slow pseudo first order reactions and is identical to that used previously to analyze the DMPD reduction of the WT PHM (Chauhan et al., 2016).

$$A_t = A_0 + A_1 (1 - e^{(-k1t)}) + A_2 (1 - e^{(-k2t)}) + ct \qquad (9)$$

Where A_1 and A_2 are the absorbance as a function of time for each of the two exponential time courses with rate constants k_1, k_2 respectively. A_0 is the initial absorbance at time zero. As before, it was found that DMPD reduction continued in a slow, almost linear, reaction after all the Cu(II) complex had been reduced. In a reaction of 20 mM Cu(II)-M49H with 1 mM DMPD in combination buffer at pH 5.5 under strictly anaerobic conditions, k_1 and k_2 had values of 102 ± 2 s^{-1} and 4.0 ± 0.1 s^{-1} and appeared to be present in a ratio of 2:1 respectively. The data show that the Cu(II) complex is reduced rapidly but at least two species likely exist with differing rates of reduction. We note that EPR spectroscopy described above also identifies two components whose composition and g/A values are pH dependent. Therefore, we suggest that the biphasic reduction kinetics are the result of differing rates of reduction for protonated and deprotonated forms of the Cu(II)-M49H complex. Although the ratios of major and minor components differ somewhat between the stopped flow and EPR data, we note that they represent data collected at room temperature versus 100 K respectively which can alter the protonation equilibrium significantly.

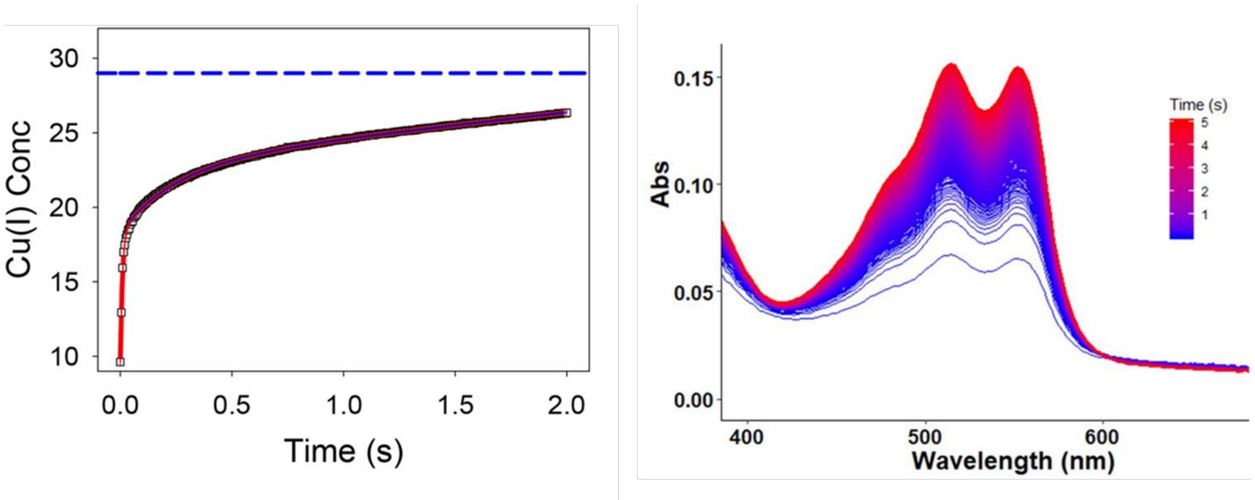

Figure 3.9 Stopped flow measurement of the reduction of 20 mM Cu(II)-M49H by 1 mM DMPD in combination buffer at pH 5.5 and 23°C. The top panel is a plot of calculated Cu(I) concentration versus time using $\varepsilon_{515} = 5200\ M^{-1}cm^{-1}$. The data are simulated by a double exponential rate equation with fast and slow rate constants of 102 and 4 s^{-1} respectively in an approximate ratio of 2:1.

3.3 Conclusions

We have described a model system for the M-center of PHM and DβM, which has been designed by mutagenic repurposing of a metallochaperone copper-binding site. Although a crystal structure is not yet available, energy minimization suggests a structure close to that of the crystallographic M-centers, while spectroscopic investigations confirm strong correlations between the structure and electronics of model versus enzyme. In particular, adduct formation between CO in the reduced forms, and azide in the oxidized forms, demonstrates a similar reaction chemistry. Of significance, the data show clearly that structural attributes such as the weak Cu−S(Met) bond (XAS) and the binding of diatomics (ν(CO)) are properties of the His2Met ligand set itself, rather than electronics induced by the enzyme protein scaffold.

We also investigated the oxygen reactivity of the reduced forms of the model, finding that the Cu(I)-His_2Met site was unreactive to O_2. Consensus has arisen around the notion that 3-coordinate Cu(I) complexes with N3 and/or N2S ligand sets are reactive toward oxygen, and there is a substantial amount of inorganic literature that supports this premise in aprotic solvents (J. Y. Lee & Karlin, 2015). In proteins, there is likewise a large body of work that demonstrates the fast reactivity of O_2 with Cu(I)His_3 active sites, albeit mainly in binuclear (hemocyanin, tyrosinase, cytochrome oxidase) or trinuclear (multicopper oxidase) systems (Quist et al., 2017). With the exception of LPMOs where the Cu(I) state appears to be extremely reactive toward dioxygen (Caldararu et al., 2019; Kjaergaard et al., 2014), the data on type 2 mononuclear copper centers is extremely sparse and, in the case of PHM and DβM, is complicated by the presence of two chemically distinct spatially separated metal sites. We believe that our model data provide some of the first conclusive evidence that mononuclear Cu(I) centers in aqueous environments may be less reactive toward O_2 than presumed, and require substrate activation. While this may seem surprising, it is nonetheless entirely consistent with the observed reactivity of the enzymes. Previous work has clearly established that oxygen reduction in PHM (Evans et al., 2006; Kline et al., 2013; Kline & Blackburn, 2016) is 100% coupled to substrate hydroxylation even with slow substrates and mutants with a low activity, implying that the M-center is unreactive until a substrate is bound. While the origin of this activation is still unknown, it raises questions relating to what structural and/or chemical properties induce the oxygen reactivity that is observed during catalysis. The development of this model system is in its early stages, but we anticipate further efforts to introduce reactivity that will model substrate binding and oxygen activation. Such efforts have been successful in other rationally designed enzyme mimics such as the three-helix bundles designed by Pecoraro and co-workers to model nitrite reductase (Koebke & Pecoraro,

2018) or the engineered myoglobin systems of Lu and co-workers that are successful mimics of nitric oxide reductase (Bhagi-Damodaran et al., 2018) (Yeung et al., 2009). Modification of second sphere H-bonding effects to induce diatomic activation (Mann et al., 2017) or to alter binding constants of exogenous ligands (Mann et al., 2018) has also been achieved by Borovik Lab and co-workers in rationally designed copper-binding sites engineered into streptavidin scaffolds. These emerging systems all leverage the potential of biomimetic modeling in aqueous environments that can couple the effects of protonation and H-bonding with the promise of induced substrate reactivity. Our future studies on the M-site model will explore these and other areas of biomimetic chemistry.

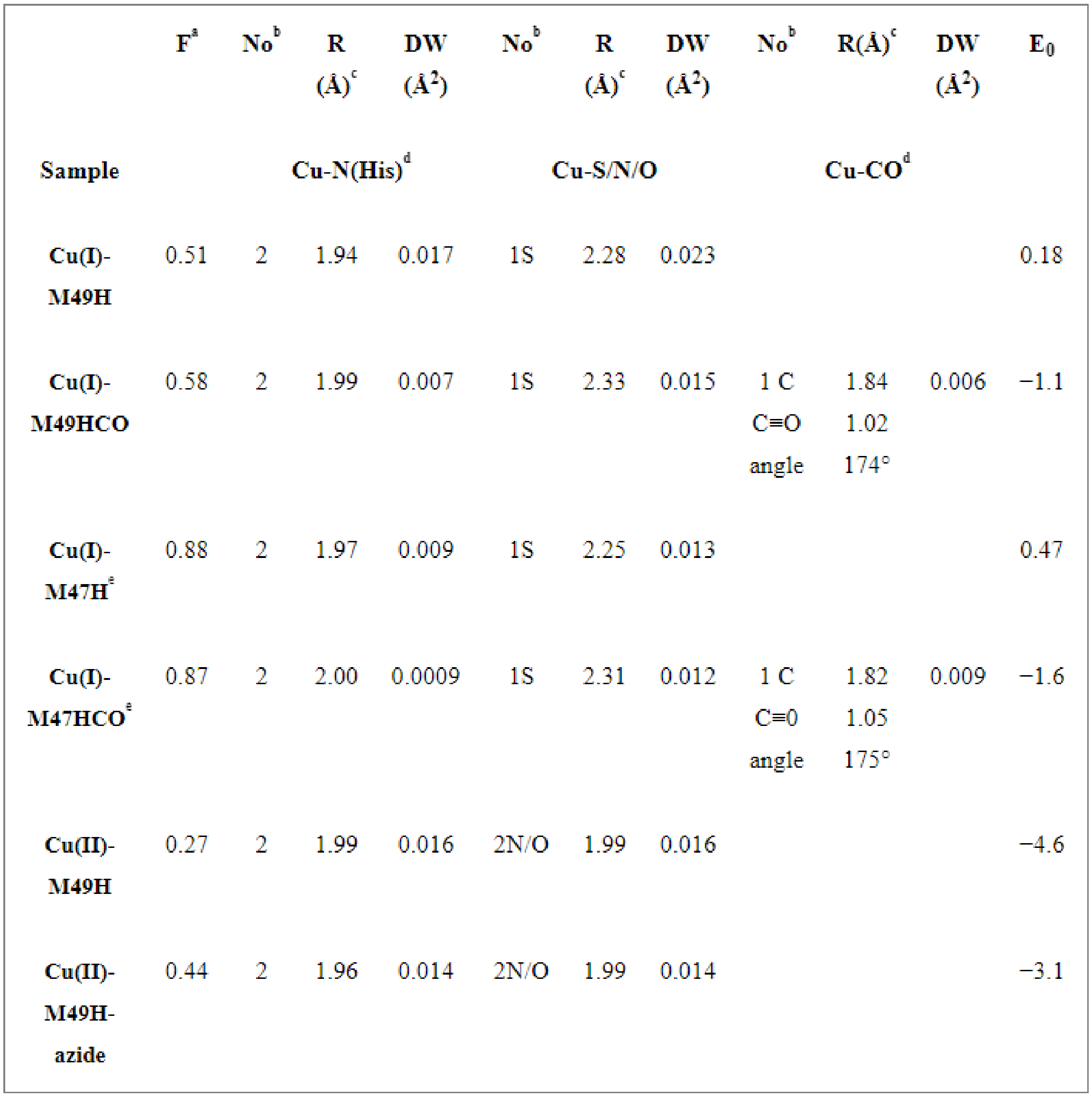

Sample	F[a]	No[b]	R (Å)[c]	DW (Å^2)	No[b]	R (Å)[c]	DW (Å^2)	No[b]	R(Å)[c]	DW (Å^2)	E_0
		Cu-N(His)[d]			Cu-S/N/O			Cu-CO[d]			
Cu(I)-M49H	0.51	2	1.94	0.017	1S	2.28	0.023				0.18
Cu(I)-M49HCO	0.58	2	1.99	0.007	1S	2.33	0.015	1 C	1.84	0.006	−1.1
								C≡O	1.02		
								angle	174°		
Cu(I)-M47H[e]	0.88	2	1.97	0.009	1S	2.25	0.013				0.47
Cu(I)-M47HCO[e]	0.87	2	2.00	0.0009	1S	2.31	0.012	1 C	1.82	0.009	−1.6
								C≡0	1.05		
								angle	175°		
Cu(II)-M49H	0.27	2	1.99	0.016	2N/O	1.99	0.016				−4.6
Cu(II)-M49H-azide	0.44	2	1.96	0.014	2N/O	1.99	0.014				−3.1

Table 3.1 Fits obtained to the ascorbate-reduced Cu K EXAFS of the M49H and M47H PHM models at pH 5.5 by curve-fitting using the program EXCURVE 9.2.

[a] F is a least-squares fitting parameter defined as $F^2 = \frac{1}{N}\sum_{i=1}^{N} k^6 (Data - Model)^2$

[b] Coordination numbers are generally considered accurate to ± 25%.

[c] In any one fit, the statistical error in bond-lengths is ±0.005 Å. However, when errors due to imperfect background subtraction, phase-shift calculations, and noise in the data are compounded, the actual error is probably closer to ±0.02 Å.

[d] Fits included both single and multiple scattering contributions from the imidazole ring and/or the linear CO unit.

[e] M47H samples were measured in 50 mM sodium phosphate buffer pH 8.

	F[a]	No[b]	R (Å)[c]	DW (Å^2)	No[b]	R (Å)[c]	DW (Å^2)	No[b]	R (Å)[c]	DW (Å^2)	E$_0$
Sample			**Cu-N(His)[d]**			**Cu-S**			**Cu-CO[d]**		
pH 4	0.75	2	1.99	0.009	1S	2.34	0.012	1 C C≡O angle	1.82 1.06 179°	0.012	--1.3
pH 5.5	0.58	2	1.99	0.007	1S	2.33	0.015	1 C C≡O angle	1.84 1.02 174°	0.006	-1.1
pH 8	0.71	2	1.99	0.015	1S	2.32	0.023	1 C C≡O angle	1.83 1.05 180°	0.013	-1.0
pH 10	0.60	2	1.98	0.010	1S	2.34	0.017	1 C C≡O angle	1.81 1.05 180°	0.009	-0.7

Table 3.2 Fits obtained to the Cu K-EXAFS of the M49H Cu(I)-carbonyl complexes as a function of pH.

[a] F is a least-squares fitting parameter defined as $F^2 = \frac{1}{N}\sum_{i=1}^{N} k^6 (\,Data - Model\,)^2$

[b] Coordination numbers are generally considered accurate to ± 25%.

[c] In any one fit, the statistical error in bond-lengths is ±0.005 Å. However, when errors due to imperfect background subtraction, phase-shift calculations, and noise in the data are compounded, the actual error is probably closer to ±0.02 Å.

[d] Fits included both single and multiple scattering contributions from the imidazole ring and/or the linear CO unit.

Sample	Component 1			Component 2				
	g-value	A-value	Line Width	g-value	A-value	Line width	Ratio	% Cu(II)
pH 4.4	g_1 2.049 g_2 2.081 g_3 2.316	A_1 10 A_2 10 A_3 466	6.2	g_1 2.054 g_2 2.102 g_3 2.263	A_1 10 A_2 10 A_3 402	6	1: 0.20	48
pH 5.5	g_1 2.049 g_2 2.076 g_3 2.301	A_1 10 A_2 10 A_3 481	7.8	g_1 2.062 g_2 2.084 g_3 2.238	A_1 10 A_2 10 A_3 472	4.8	1: 0.31	62
pH 8.0	g_1 2.090 g_2 2.019 g_3 2.269	A_1 10 A_2 10 A_3 497	8.2	g_1 2.055 g_2 2.077 g_3 2.233	A_1 10 A_2 10 A_3 501	5.3	1: 0.87	51
Azido pH 5.5	g_1 2.041 g_2 2.068 g_3 2.253	A_1 10 A_2 10 A_3 476	5.2	g_1 2.029 g_2 2.107 g_3 2.269	A_1 10 A_2 10 A_3 390	4.0	1: 0.25	89
Azido pH 8	g_1 2.043 g_2 2.072 g_3 2.247	A_1 10 A_2 10 A_3 514	6.2	g_1 2.029 g_2 2.107 g_3 2.269	A_1 10 A_2 10 A_3 390	4.0	1: 0.37	70

Table 3.3 EPR parameters used to fit the spectra in Figures 3.6 and 3.7 using EASYSPIN.

CHAPTER 4: The catalytic M-center of copper monooxygenases probed by rational design. Effects of selenomethionine and histidine substitution on structure and reactivity.[2]

4.1 Introduction

Methionine, histidine, and cysteine are common ligands for copper in biological systems. Because these ligands can bind to both oxidation states of copper, they are often found together in proteins whose function is electron transfer, such as the blue copper proteins azurin and plastocyanin ((Hosseinzadeh et al., 2016; Liu et al., 2014), the purple CuA-containing proteins cytochrome oxidase (Kroneck, 2018; Williams et al., 1999) and N_2O reductase (Carreira et al., 2017; Kroneck, 2018), and engineered azurins (Chakraborty et al., 2015; Liu et al., 2014). Very recently, a CuA site formed at a dimer interface has been identified in pmoD, an accessory protein involved in particulate methane monooxygenase assembly and/or metalation (Fisher et al., 2018; Ross et al., 2019). Methionine ligation is also common in periplasmic transporters such as CopC (Djoko et al., 2007), PCuaC (Abriata et al., 2008), and the CusCBAF exporter (McEvoy et al., 2012; Su, Long, & Yu, 2011; Su, Long, & Zimmermann et al., 2011), where the methionines are either found as the sole Cu(I) binding residues (Bagai et al., 2007; Mealman, Zhou, et al., 2012; Ucisik et al., 2013), or in a mixed complex with histidine (Loftin et al., 2007; Xue et al., 2008). These latter systems are designed to stabilize the Cu(I) and/or Ag(I) states, and in most cases adopt multi-Met motifs where the preponderance of uncharged thioether donors inhibit oxidation of copper to its dicationic state (Davis & O'Halloran, 2008).

The family of mononuclear monooxgenases that encompass the enzymes PHM (peptidylglycine monooxygenase), DβM (dopamine β-monooxygenase), and TBM (tyramine β-monooxygenase) are unusual in that they exhibit a His_2Met ligand set at the copper center (CuM) that binds

---

*Material in this chapter has been published in this or similar form in Biochemistry, and is used here with permission of the American Chemical Society.

Alwan, K. B., Welch, E. F., & Blackburn, N. J. (2019). Catalytic M Center of Copper Monooxygenases Probed by Rational Design. Effects of Selenomethionine and Histidine Substitution on Structure and Reactivity. *Biochemistry*, *58*(44), 4436–4446. https://doi.org/10.1021/acs.biochem.9b00823 oxygen and activates it towards hydroxylation of the substrate bound nearby (Klinman, 2006b; S. Prigge et al., 2000; Vendelboe et al., 2016). These proteins contain a second copper center (CuH) which is coordinated by three histidines, but whose role appears to be electron transfer (Chauhan et al., 2014, 2016; Osborne et al., 2013; Prigge et al., 1997, 1999). The role of the Met ligand in the catalytic chemistry has been enigmatic, for a number of reasons. First, it is absolutely essential to catalysis; second, it only coordinates in the reduced form; thirdly, it appears to be only weakly bound to copper in the state that binds oxygen (Bauman et al., 2011; Blackburn et al., 2000; Eipper et al., 1995; Hess et al., 2010). Mutagenesis of the catalytic Met to Ile (Siebert et al., 2005), His (Bauman et al., 2011; Hess et al., 2010; Kline & Blackburn, 2016), and Cys (Hess et al., 2010; Hess, Wu, et al., 2008) has largely failed to illuminate the electronic role, as these mutants are either inactive due to copper loss, or, in the case of Cys, lead to suicide inhibition (Hess et al., 2010; Hess, Wu, et al., 2008). Studies (Elwell et al., 2017; Quist et al., 2017) on the reactivity of thioether containing inorganic models in aprotic solvents at low temperature are also inconclusive as to whether thioether coordination is expected to amplify or leave unchanged the electrophilic properties of the cupric superoxo (Kim et al., 2015) believed to be the reactive species in these enzymes (Bauman et al., 2006; Chen et al., 2004; Chen & Solomon, 2004; Evans et al., 2003; Prigge et al., 2004). Understanding the role of this essential yet chemically silent residue has thus been challenging.

Selenomethionine (Se-Met) labeling is a useful technique for isolating the contributions to electronics and structure from thioether coordination and relating these to function. This approach has been used successfully to assess the role of the M121 ligand to the spectroscopy of azurin (Berry et al., 2003), and the M160 ligand to the structure of the CuA center in *T. thermophilus* cytochrome oxidase (Blackburn et al., 1999). The utility of the approach derives in part from the ability to isolate and track the contribution to bonding via measurements at the Se K absorption edge, which report directly on the Se-Cu bond length and its force constant via the magnitude of its Debye-Waller factor. In addition, Se-Met labeling has been leveraged to study the reaction mechanisms of metalation or metal transfer between chaperone target pairs where each has Cu-Met coordination, but where one member of the pair can be selectively labeled with Se-Met (Bagai et al., 2008). In this way, we have reported the identity of intermediates in the metallation of the CuA centers in an isolated subunit 2 of cytochrome oxidase (Chacón &

Blackburn, 2012) and engineered CuA azurin (Chakraborty et al., 2015); determined the pathway and direction of metal flux in the CusCBAF exporter (Chacón et al., 2014b); and identified a shared ligand intermediate of metal transfer between the CusF and CusB components of this metal export complex (Chacón et al., 2018). These studies share the requirement that all Met residues in the proteins be ligands to copper in order to provide maximum sensitivity to the Se label.

Against this background Se-Met labeling should be an ideal approach to assess the structural and electronic contributions of coordinated methionine to the catalytic chemistry of PHM and its homologues. Unfortunately, two factors have hindered application of the method. First, the catalytic core of PHM (residues 42 -356) contains 16 Met residues, only one of which is a ligand to copper; and second, the protein is expressed in a mammalian cell line, which precludes simple Se-Met incorporation via supplementation of the medium due to the transmethylation of homocysteine by methionine synthase. Recently we reported the construction, bacterial expression, and characterization of a protein-based model for the M-center of PHM, built from a small metallochaperone (CusF) scaffold, and carrying (via mutation) the His_2Met ligand set (Alwan et al., 2019a). The spectroscopy and exogenous ligand binding properties of this model have validated its close resemblance to the M-site of PHM, and furthermore it contains a single Met residue which acts as a ligand to the copper center. This model system therefore satisfies all the conditions for using Se-Met labeling to interrogate the structural and electronic properties of the His_2Met ligand set. The model system also allows for facile substitution of the Met ligand by histidine, forming a derivative that in the enzyme is inactive.

Here we report spectroscopic studies of the Cu(I) and Cu(II) states of the Se-Met and His variants of the CusF M-site model, and discuss the results in terms of how the data informs the structure and function of the mononuclear monooxygenase family of metalloenzymes. We examine the effects on coordinate structure and exogenous ligand binding via XAS, FTIR, and EPR, and the consequences of mutations on redox chemistry via studies on the reduction by ascorbate and oxidation via molecular oxygen. The EXAFS data at the Se K-edge of the Se-Met variant provides unique information on the nature of the Cu-Methionine bond while kinetic comparisons document a remarkable stability of the Cu(I) state in all three variants. The results show little difference between the Met ligand and its Se-Met and His congeners, and suggest that the Met contributes to catalysis in ways that are more complex than simple perturbation of the redox chemistry.

4.2 Materials and methods

Construction of CusF Mutants. W44A M49H and W44A M47HM49H mutations were introduced into the CusF M8M59Ile double-mutant background as previously described in Section 3.2.

Expression and Purification of CusF W44A M49H and W44A M47HM49H Variants. S-Met CusF variants were expressed and purified as previously described in Section 3.2.

Expression and Purification of Se-Met Labeled CusF M49H. The *pETDuet-1-CusF* plasmid containing the M49H mutation was transformed into Met auxotrophic *E. coli* cells. Liquid culture medium (LB and 100 mg/mL ampicillin) was inoculated from a freezer stock and incubated overnight at 37 °C while being shaken at 250 rpm. A 100 μL aliquot of the overnight culture was used to inoculate 10 mL of minimal culture medium containing S-Met. After overnight incubation at 37 °C with shaking, this culture was used to inoculate a 1 L flask of minimal medium substituted with Se-Met. After approximately 12 hours, when the cell culture reached an OD_{600} of approximately 1, the culture was induced with 500 μM isopropyl β-D-1-thiogalactopyranoside. Growth was continued at 17 °C for 16−20 hours, after which cells were harvested and purified as previously described in Section 3.2. Se and protein concentrations were determined by ICP-OES and a BCA assay from which the Se:protein ratio was determined and used to verify the Se-Met substitution yield, which in all cases was found to be >95%.

Sample Preparation. The CusF apoprotein was reconstituted with 100 mM CuSO4 at a ratio of 2.5:1 using a syringe pump operating at 25 μL/h and allowed to incubate on ice for 1 hour with stirring. Excess Cu(II) was removed by overnight dialysis in 50 mM sodium phosphate (NaP) (pH 8). Se and Cu concentrations were determined by ICP-OES. The protein was assessed by a BCA assay and combined with Se and Cu analyses to calculate metal:protein ratios. The holoprotein was then exchanged into pH 5.5 combination buffer, made up of 50 mM formate, 50 mM MES, and 50 mM HEPES, via a rapid 4-fold dilution of the 4-fold concentrated protein into buffer. A small protein loss was observed, but the copper:protein ratios remained at 1:1 as confirmed by ICP. For Cu(I) samples, Cu(II)-reconstituted protein in pH 5.5 combination buffer was reduced anaerobically by addition of a 2-fold excess of ascorbate buffered at pH 5.5. The ascorbate was then removed by two cycles of desalting on spin columns (Zeba) as previously described(Alwan et al., 2019a). The Cu(I)-reconstituted protein could also be prepared by addition of a 2.5-fold excess of $[Cu(I)(CH_3CN)_4]PF_6$ in buffer supplemented with 10% acetonitrile, followed by serial dialysis against the same buffer containing 5% and 0% acetonitrile. This procedure was carried out in a Coy chamber at 30 ppm of O2 and took ~24 hours to complete. Surprisingly, we observed 20% oxidation of samples prepared in this way. The ascorbate reduction protocol could be carried out more expeditiously and did not lead to oxidation so was used in all future experiments.

Spectroscopic Measurements. EPR, FTIR, XAS, and UV-vis protocols, including azide titrations to determine binding constants, were as described previously in Section 3.2. X-ray absorption measurements were taken on beamlines (BLs) 7.3 and 9.3 at the Stanford Synchrotron Radiation Lightsource, operating at 3 GeV under continuous top-up mode. Copper spectra were recorded and analyzed as described previously in Section 3.2. Se K edge data were collected on BL 7.3 using 20% detuning of the monochromator or on BL 9.3 using a Rh-coated mirror set to a 15 keV energy cutoff to reduce harmonic contamination of the beam. Se data were calibrated by means of a Se metal foil placed between the second and third ionization chambers. XAS was measured at 10 K in fluorescence mode using either a 30-element (BL 7.3) or 100-element (BL9.3) Ge detector (Canberra). Elastic scatter was reduced by means of a Soller slit assembly and a 6μ-As filter placed immediately in front of the detector, and total counts from each channel were adjusted below 50 kHz to avoid saturation. Four to six scans of each sample were collected and averaged to improve the signal-to-noise ratio, and the average of four to six scans of a buffer blank were subtracted from each averaged spectrum to correct for pre-edge curvature and As Kβ fluorescence emanating from the Soller slit filter. Data were analyzed and simulated as described previously (Alwan et al., 2019a).

Kinetics of Oxidation by O_2. Rates of oxidation by molecular oxygen were determined using the 400 nm charge transfer (CT) band of the azido adduct to determine the rate of formation of the Cu(II) form. Anaerobic ascorbate-free Cu(I) protein was produced as described above, transferred to a reaction chamber, and diluted with buffer previously saturated with 100% oxygen gas at 25 °C and ambient pressure. During the course of the ensuing oxidation reaction, the reaction chamber was gently purged with a stream of buffer-saturated O_2 gas to maintain the O_2 level at a constant (100%) level. Aliquots of the reaction mixture were sampled at appropriate time points and mixed with 100 mM sodium azide, resulting in conversion of all oxidized [Cu(II)] species into the chromophoric azido adduct with a λ_{max} of 400 nm. Rates were fitted to a single-exponential rise to maximum using nonlinear regression in SigmaPlot 14.

Stopped-Flow Spectrophotometry of Ascorbate Reduction. Reduction rates of Cu(II) azido derivatives by ascorbate were determined from the rate of disappearance of the 400 nm CT band using an Applied Photophysics SX20 stopped-flow instrument contained in a Vacuum Atmospheres anaerobic chamber with oxygen levels below 1 ppm. Anaerobic Cu(II) azido samples were placed in one syringe and shot against anaerobic buffer containing a 5-fold excess of ascorbate. Data were fitted to single-exponential decay curves to extract pseudo-first-order rate constants.

4.3 Results and Discussion

In a previous study, we reported the properties of the His_2S(Met) Cu(I) complex engineered into the protein scaffold of CusF, as small periplasmic metallochaperone (Alwan et al., 2019a). In the present work we investigate the effect on the structure, electronics, adduct formation and redox properties of Met substitutions, Se-Met and His. Using the methods as previously reported (Alwan et al., 2019a), both Cu(I) and Cu(II) complexes were prepared for Se-Met and His substituted CusF. The Cu(I) and Cu(II) complexes formed with simple 1:1 stoichiometry. The structure of the complexes was studied using Cu and Se K edge XAS. The EXAFS data for the Cu(I) and Cu(II) complexes of the His_2Se-Met model were fit using full curved-wave multiple scattering theory with metrical parameters listed in Table 4.1.

Reduced forms. For the Cu(I) complex, the best fit at the Cu edge (Figure 4.1 and Table 4.1) is a 3-coordinate complex comprising two Cu-N(His) and 1 Cu-Se-Met interaction with Cu-N and Cu-Se distances of 1.95 and 2.43 Å respectively. The Se edge fit gave an identical Se-Cu distance. The Se-Cu bond length is typical of Cu(I)-selenoethers in both inorganic (Black et al., 1996; H. C. Wang et al., 2011) and protein (Bagai et al., 2008; Chacón et al., 2014b) systems but the Debye-Waller (DW) factor for the Se-Cu ($2\sigma^2 = 0.017$ Å^2) is high for a single absorber-scatterer interaction, and is further discussed below.

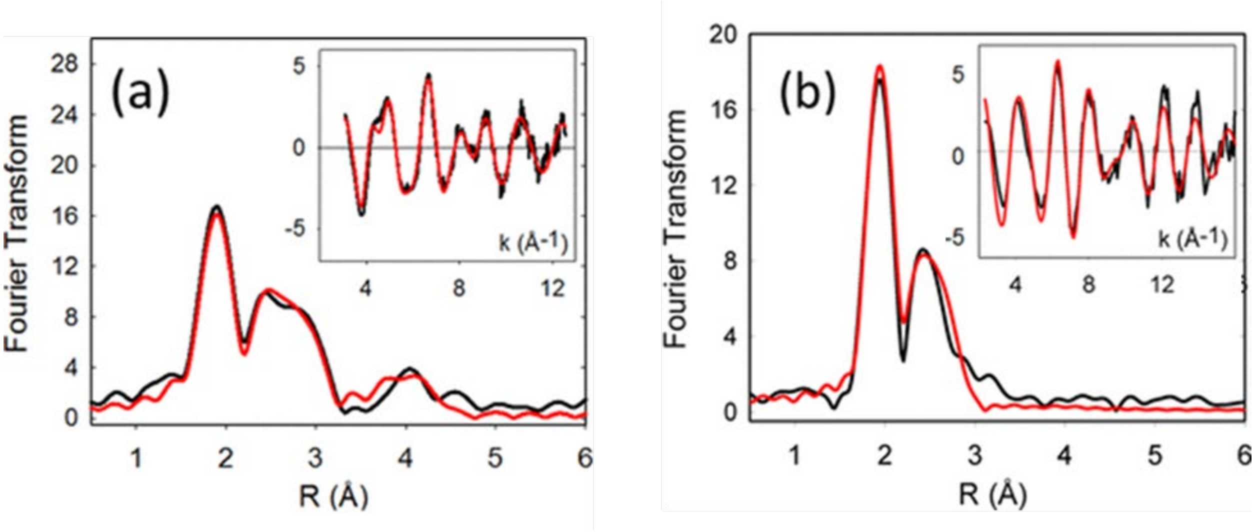

Figure 4.1 Fourier transforms and EXAFS (insets) of the reduced (Cu(I)) CusF Se-Met-M49H derivative. (a) Cu edge data (b) Se edge data. Black traces are experimental data, red traces are simulations using EXCURVE 9.2. Parameters used in fitting the data are listed in Table 4.1.

Selenomethionine coordination to Cu(I) is expected to give rise to two peaks in the Fourier transform of the Se K EXAFS, Se-C from the ligand itself and Se-Cu from its interaction with the metal. In native CusF with the (Se-Met)$_2$ His ligand set, the DW term ($2\sigma^2$) was found to be 0.005(2) Å^2, indicating a strong Cu-Se-Met interaction (Chacón et al., 2018). Remarkably, the intensity of the Se-Cu interaction is significantly attenuated on transitioning from the Se(Met)$_2$His -Cu(I) of native CusF to Se(Met)His$_2$-Cu(I) in the PHM M-site model. This behavior has been observed previously in the S(Met)-containing model and in PHM and DβM enzymes themselves (Alwan et al., 2019a), and has been interpreted in terms of fluxionality of the Cu-thioether bond. This hypothesis was based on assessment of the increasing Debye-Waller factors for the Cu-S(Met) interaction in the series Cu(I)-S(Met)$_3$ (CusB), Cu(I)-S(Met)$_2$His

(CusF), and Cu(I)-S(Met)His$_2$ (monooxygenase model). We suggested that the Cu-Met bond is inherently fluxional leading to the reversible dissociation of any one Cu-(Met), but leaving the other two ligands coordinated with a low average DW. In the (Met)His$_2$ case the Met ligand would always be labile and would exhibit a large Debye-Waller factor. This argument also explains why Met residues are often found lining import and export channels of transporters such as CTR1 (De Feo et al., 2009; Jiang et al., 2005; Rubino et al., 2010), CusA (Su, Long, & Yu, 2011) and CopA (Gourdon et al., 2011b; Mattle et al., 2015), since a single Cu-Met interaction is in rapid exchange between on and off conformers. The Se edge data provides a means of validating this hypothesis with increased confidence since the Se K EXAFS data allows the Se-metal interaction to be isolated from contributions from the other ligands. The Debye-Waller terms for the series Cu(I)-Se(Met)$_3$ (CusB) (Chacón et al., 2018), Se(Met)$_2$His (CusF) (Chacón et al., 2018) and the Se(Met)His$_2$ (PHM model) are 0.005, 0.005, and 0.018 Å^2 respectively. Here the high DW factor observed in the Se(Met)His$_2$ ligand set of the monooxygenase model amply demonstrates the lability of a single Cu(I)-methionine bond.

The Cu K EXAFS of the Cu(I) forms of the M47HM49H double mutant (His$_3$) ligand set is unremarkable and simulates to 3 Cu-N(His) at 1.95 Å. Experimental and simulated data are shown in Figure 5.2 with parameters listed in Table 5.2.

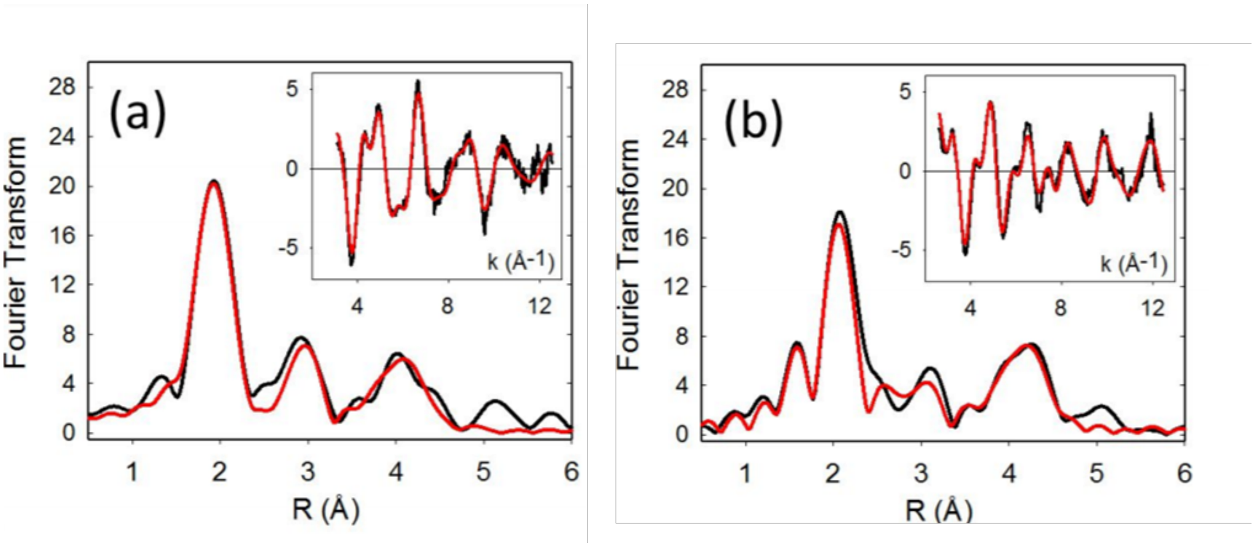

Figure 4.2 XAS structural characterization of the Cu(I) forms of the His$_3$ (M47HM49H) CusF M site model. Fourier transforms and EXAFS (insets) of (a) unligated and (b) CO-bound complexes. Parameters used in the fits are listed in Table 4.2.

Cu(I)carbonyl derivatives. Both S-Met and Se-Met derivatives of the CusF M49H PHM model react with carbon monoxide to form CO adducts. For the S-Met derivative reported previously, the close correspondence between model and enzyme M-site carbonyl, suggested strong structural and electronic similarities. The CO stretching frequency of a metal-carbonyl is strongly perturbed via an electronic mechanism whereby metal d-electron density is back-donated into the empty π* orbitals of the triply-bonded CO ligand, reducing the bond-order and thus red-shifting ν(CO) (Pike, 2012). In turn, the magnitude of this effect is influenced by the donor strength of the other ligands in the complex, making ν(CO) an excellent reporter of the electronics of ligand-metal interaction. We are now able to compare the donor strength of thioether with selenoether ligands, where the softer, more polarizable selenomethionine might be expected to form stronger covalent bonds with Cu(I), and thus lead to a larger red-shift. Indeed such behavior has been documented in a selenium substituted H-cluster of the CpI hydrogenase matured using the $[Fe_2(\mu(SeCH_2)_2NH)(CO)_4(CN)_2]^{2-}$ synthon, where two seleno-azidothiolate ligands bridge the two Fe atoms of the H cluster (Kertess et al., 2017). FTIR data comparing ν(CO) for S-Met and Se-Met ligand complexes of the CusF M49H model are shown in Figure 4.3. The Se-Met derivative has a ν(CO) of 2087 cm^{-1}, just 2 wavenumbers less than the S-Met system. For comparison, FTIR data for the CO complex of the M47HM49H double His mutant shows a much larger red-shift to 2072 cm^{-1} similar to that reported for the M314H mutant of PHM (where the single M314 residue at the M-center is replaced by His) (Kline & Blackburn, 2016). These data indicate (i) that Se substitution has minimal effect on the electronic structure of the complex and (ii) both S-Met and Se-Met ligands are much weaker donors than histidine.

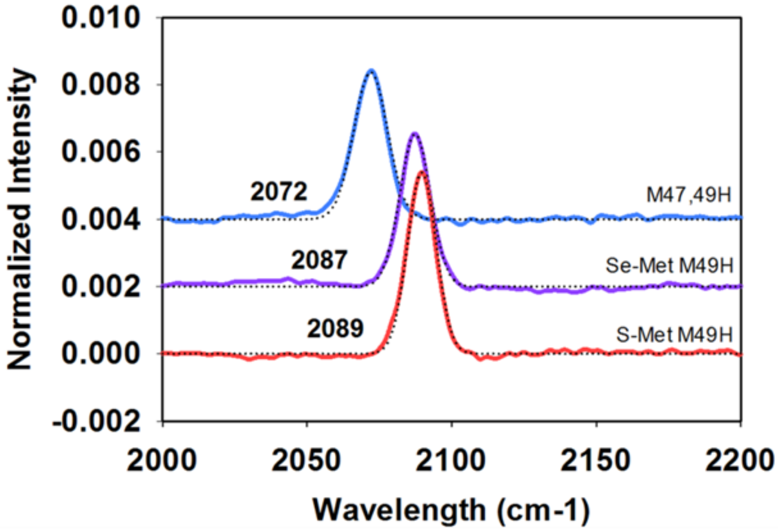

Figure 4.3 Fourier transform infrared spectra of the CO adducts of the Cu(I) CusF model system.

We also examined the structure of the Se-Met Cu(I)-carbonyl at both Cu and Se K edges via simulation of the EXAFS spectra. The results are listed in Table 4.1 with simulations in Figure 4.4. Se K edge EXAFS provides unique information on the Se-Cu bond-length and Debye-Waller factor, and shows the expected lengthening of the Se-Cu bond from 2.43 to 2.51 Å as the result of an increase in coordination number to form the 4-coordinate carbonyl. Like the parent complex, the DW factor is large, indicating a weak, kinetically labile bond. Cu edge data confirm details of the Cu-Se bond, together with coordination by the two His residues and a linear Cu-CO adduct (Figure 4.4 and Table 4.1).

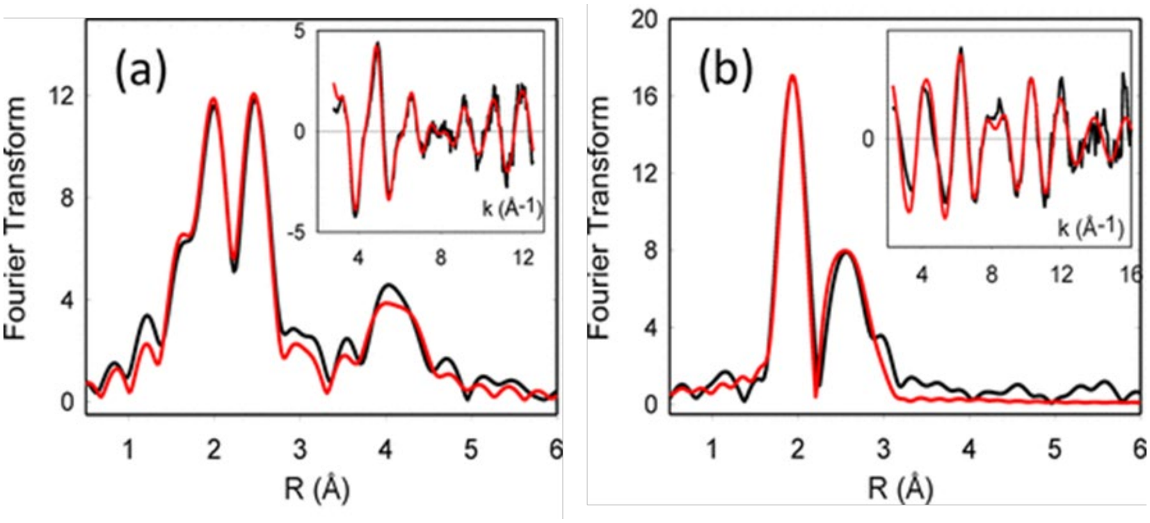

Figure 4.4 Fourier transforms and EXAFS (insets) of the reduced (Cu(I)) CO complex of the CusF Se-Met-M49H derivative. (a) Cu edge data (b) Se edge data. Black traces are experimental data, red traces are simulations using EXCURVE 9.2. Parameters used in fitting the data are listed in Table 4.1.

The X-ray absorption near edge structure (XANES) was compared for unligated Cu(I) complexes and their CO analogues and is shown in Figure 5.5. Notably, the Cu(I) data are emblematic of 3-coordination with partially resolved 1s → 4p transitions at 8983 eV on the rising absorption edges. The CO complexes exhibit XANES features typical of 4-coordinate Cu(I) carbonyls as reported previously (Alwan et al., 2019a).

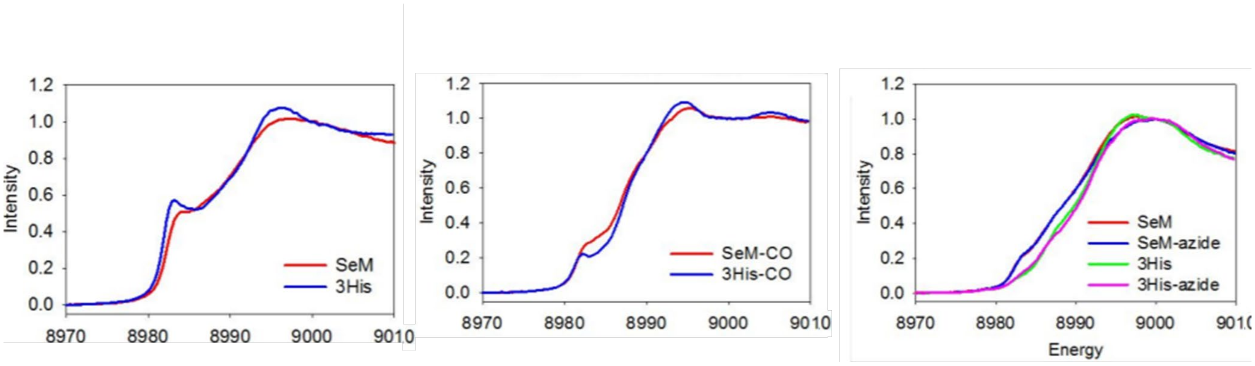

Figure 4.5 Absorption edges of M-site CusF derivatives. Unligated Cu(I) (left), CO complexes (middle), and unligated and azido Cu(II) complexes (right). Spectra are color coded as per the legend to each panel.

Oxidized Samples. The structure of the oxidized Se-Met derivative was interrogated by similar methods. Cu edge EXAFS data were best fit by a 4 – 5 coordinate model involving 4 Cu-O/N scatterers at 1.96 Å with multiple scattering contributions that were consistent with two histidine and two non-His O/N ligands as equatorial ligands. In one sample, a small contribution at ~2.4 A could be simulated by a weak interaction with Se (0.4 ± 0.2), but was absent in other samples and is likely the result of some photoreduction in the beam. Taken together, the oxidized Cu and Se edge data are most consistent with the absence of an observable Cu(II)-Se-Met interaction, and are consistent with previous conclusions, from analysis of both PHM EXAFS and the S-Met M49H model, that the Met ligand is not observable in the oxidized XAS data. This is consistent with the Met residue occupying an axial position in a tetragonally distorted 5-coordinate complex, with two His and two solvent ligands bound in the equatorial plane, and confirms that the system must undergo a significant conformational change on reduction, as previously suggested (Blackburn et al., 2000; Chen et al., 2004). Figure 4.6 top shows experimental and simulated EXAFS data for Cu and Se edges of the Cu(II) Se-Met complex. EXAFS-derived metrical parameters are listed in Table 4.2. EXAFS of the oxidized His_3 double mutant was unremarkable, and analyzed to three imidazole and one O/N scatterer as expected (Table 4.2, Figure 4.6 bottom).

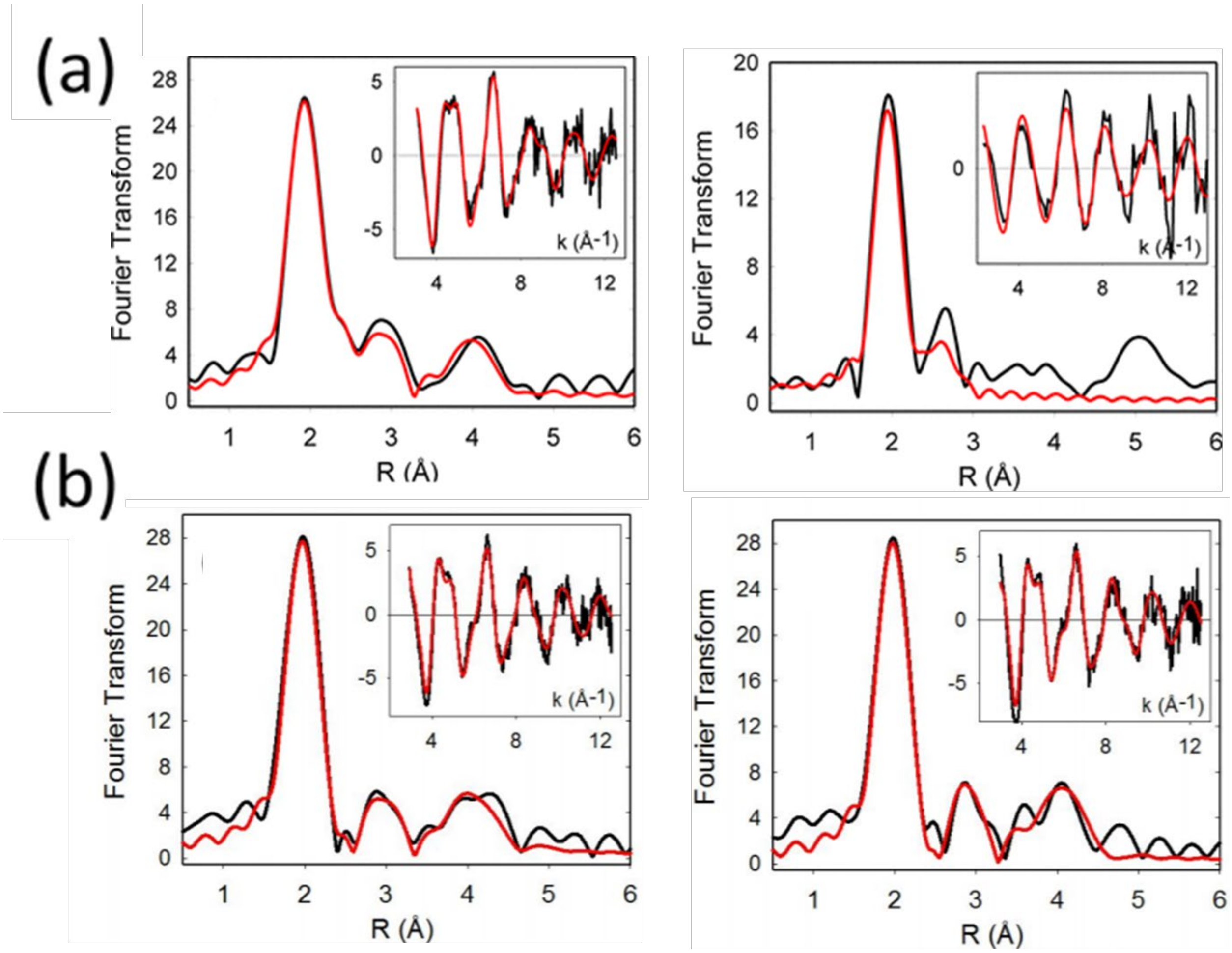

Figure 4.6 Fourier transforms and EXAFS (insets) of the oxidized (Cu(II)) CusF Se-Met-M49H derivative (top). Cu edge data (left) Se edge data (right). Black traces are experimental data, red traces are simulations using EXCURVE 9.2. Parameters used in fitting the data are listed in Table 5.2. XAS structural characterization of the Cu(II) forms of the His_3 (M47HM49H) CusF Msite model (bottom). Fourier transforms and EXAFS (insets) of (left) unligated and (right) azido-bound complexes. Parameters used in the fits are listed in Table 4.3.

XANES data for the Cu(II) complexes and their azido adducts are shown in Figure 4.3 and indicate a slightly lower energy for the Se-Met derivative than for the His_3 homologue. The XANES data for the oxidized samples were extracted from single scans, and were collected under fast scanning conditions to eliminate photoreduction. The small red-shift observed for the Se-Met derivative is consistent with some photoreduction as discussed above for the EXAFS analysis. Surprisingly, the Se-Met derivative shows a lower tendency towards *chemical* reduction (vide infra), suggesting a photoprocess that implicates an excited state.

EPR data for oxidized SeM substituted M49H and the M47H49H His_3 variant is shown in Figure 4.7. Like the M49H counterpart, the spectra were complex and indicative of multiple species. Double integration of the spectra gave spin concentrations less than the expected total copper concentrations but greater than reported previously for the parent S-Met complex (78% for Se-Met and 71% for His_3 respectively). Due to the complexity of the system, studies on these unligated Cu(II) derivatives were not pursued; rather, we focused on the characterization of the azido adducts which, as previously reported, generate EPR spectra closer to stoichiometric EPR detectable Cu(II) levels.

Reaction of the oxidized derivatives with azide. Both Cu(II)-Se-Met and His_3 derivatives react with azide to form azido adducts with absorption at 400 nm (Table 4.3). Titration data (Figure 4.8) reveal formation of 1:1 complexes with K_D= 2.9 and 3.8 mM respectively, but for Se-Met at higher azide concentrations, the absorbance at 400 nm (corrected for dilution effects) falls. The most plausible interpretation of this behavior is photobleaching of the signal due to photoreductive processes, which can be simulated by formation of a second species with lower extinction coefficient. (This species represents the photobleached azido-adduct and is not a true species; it is only included in the non-linear regression analysis to improve the accuracy of K_D). This behavior is not observed for either the parent S-Met complex or for the His_3 derivative where the titration data fit well to a single mono azido adduct. Table 4.3 compares binding parameters for S-Met, Se-Met and His_3 derivatives. EPR spectra of the azido species are shown with simulations in Figure 4.7 with relevant spectral parameters in Table 4.3. Notably, the spin concentrations determined by double integration are increased relative to the unligated derivatives and approach 85 percent.

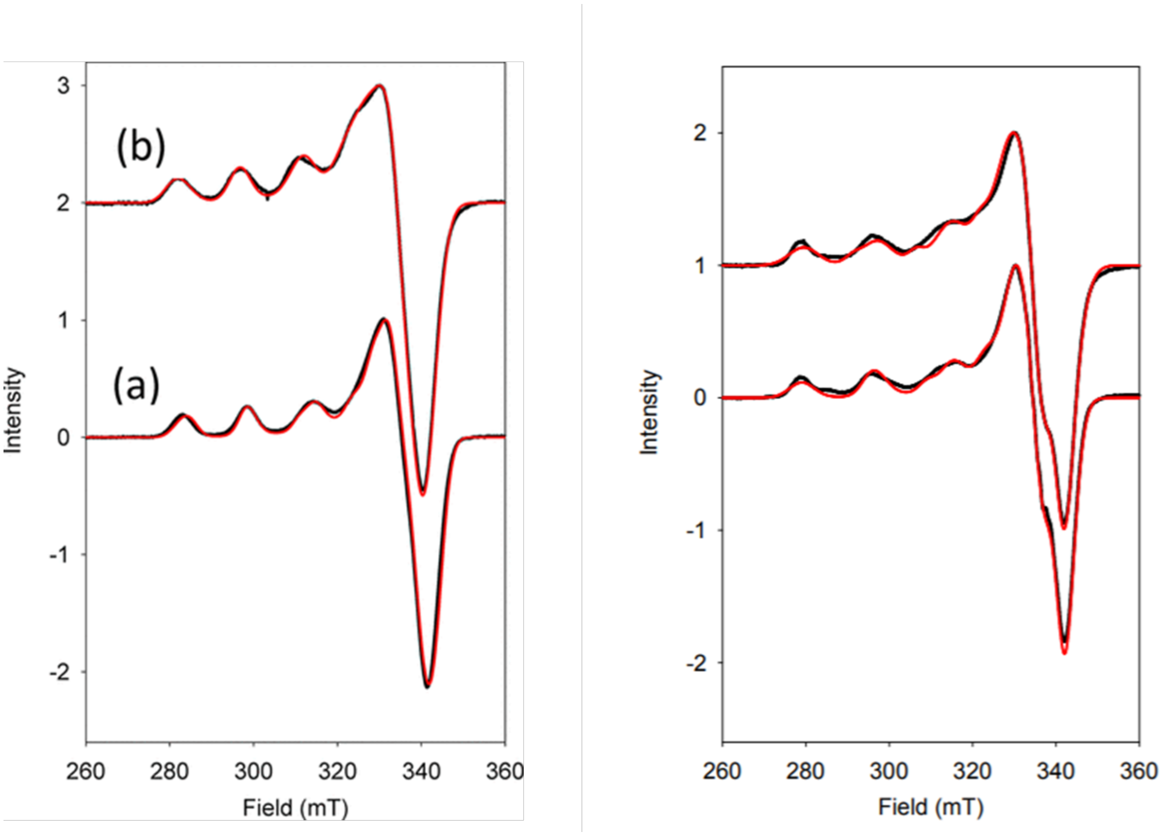

Figure 4.7 (Left) X-band CW EPR spectra of the Cu(II) azido adducts of the CusF M-site model. Black traces are experimental data while red traces are simulations using EASYSPIN. (a) Se-Met-M49H (b) His_3. Spectra were collected at a temperature of 100 K, microwave frequency 9.678 GHz, 100 Khz modulation, 10 G modulation amplitude, 20 mW microwave power and 1000 G sweep width with the field centered at 3100 G. Both spectra were simulated using 2-components with ratios and EPR parameters listed in Table 4.3. (Right) X-band CW EPR spectra of the oxidized Se-Met-M49H PHM M-site model (bottom trace) and the M47HM49H (His_3) derivative (top trace) determined at pH 5.5. Black traces are experimental data while red traces are simulations using EASYSPIN. The Se-Met model was simulated by two components in a ratio of 1:0.3 with g and A values for component 1: gx=2.065, gy=2.080, gz=2.259, Az=559 MHz; and for component 2: gx=2.053, gy=2.065, gz=2.188, Az=415 MHz. The His_3 species also exhibited a two component fit in the ratio 1: 0.45 with g and A values for component 1: gx=2.054, gy=2.073, gz=2.271, Az=483 MHz; and for component 2: gx=2.024, gy=2.121, gz=2.281, Az=395 MHz. Spectra were collected at a temperature of 100 K, microwave

frequency 9.678 GHz, 100 KHz modulation, 10 G modulation amplitude, 20 mW microwave power and 1000 G sweep width with the field centered at 3100 G.

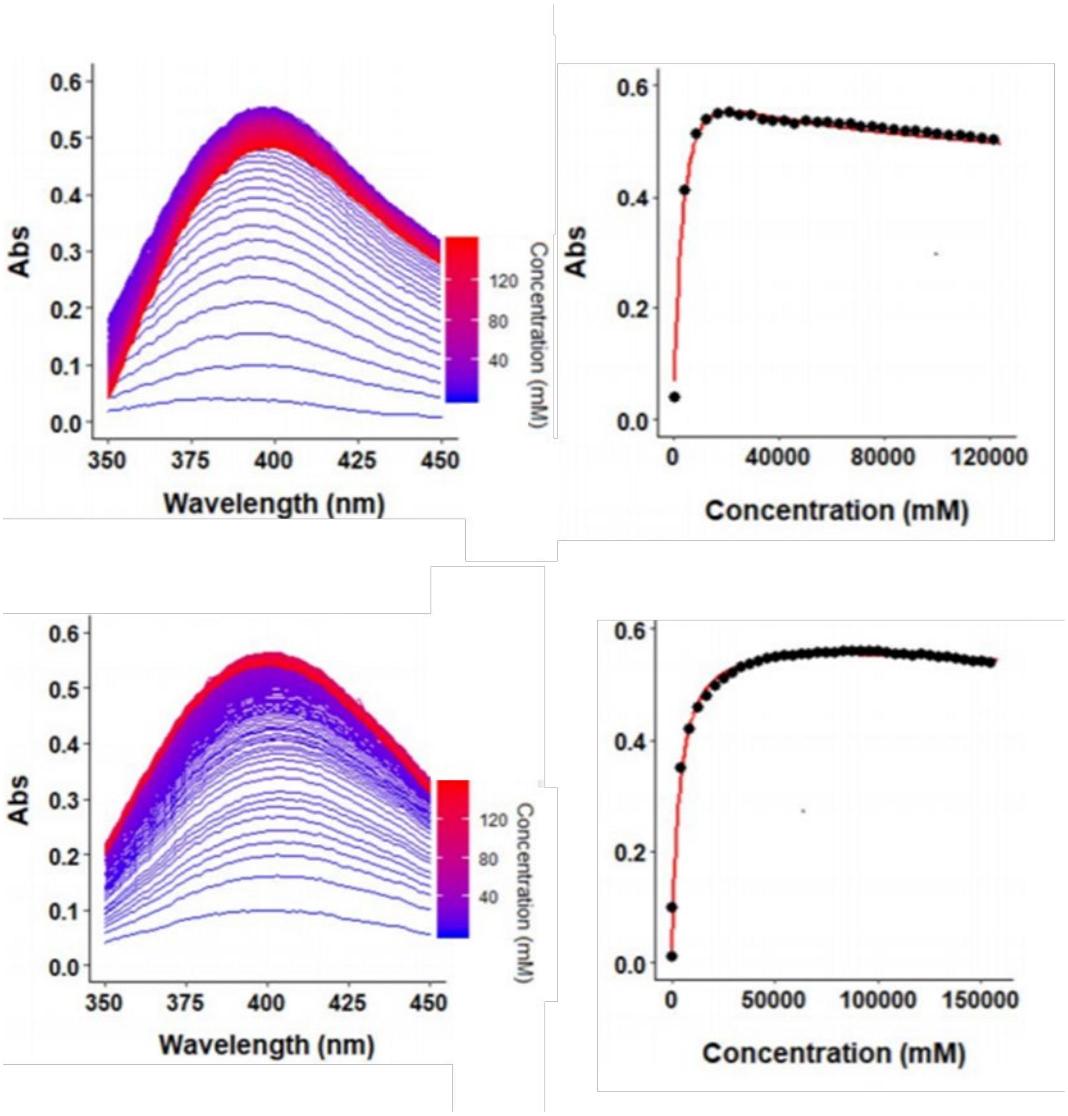

Figure 4.8 Azide titrations of the oxidized CusF M-site model variants, Se-Met (top) and His$_3$ (bottom) via additions of aliquots of 2M sodium azide to a final concentration of 100mM. The resulting absorbance at 390 nm was fit to a formation curve as described in the text. KD values extracted from the data are listed in Table 3 of the main manuscript. Top panels are for the Se-Met-M49H and bottom panels are for the M4749H (His$_3$) azido complexes.

Oxygen reactivity. The formation of simple 1:1 chromophoric azide adducts provided us with a tool to assess the relative reactivity of the three M-site model derivatives. First, we explored the reactivity with molecular oxygen. Previous work (Alwan et al., 2019a) established that the fully reduced parent S-Met complex was unreactive to molecular oxygen when a stoichiometric amount of ascorbate-reduced sample was added to an air-saturated buffer in an oxygen electrode, or when a catalytic amount of reduced or oxidized sample was reacted with air-saturated buffer in the presence of excess reductant. We repeated these experiments and again found neither stoichiometric oxidation nor catalytic oxidation of ascorbate on the time-scale of the experimental protocol (0-5 minutes). Therefore, we designed an additional experiment wherein fully reduced, ascorbate-free complex was allowed to react with oxygen-saturated buffer for several hours during which aliquots were removed and treated with 100 mM sodium azide. Any oxidized product was then converted into its azide adduct which was immediately quantified by UV/Vis at 400 nm (Figure 4.9). In a separate experiment we added 100 mM sodium azide to the reaction mixture and monitored the formation of the 400 nm Cu(II)-azido peak at defined time points during the course of the oxidation reaction. The results are shown in Figure 4.10 with rate constants listed in Table 4.3. The analysis indicates comparable yet extremely slow rates of oxidation which are either comparable or reduced in the presence of azide, suggesting that azido adduct formation does not accelerate the rate via favoring the Cu(II) state.

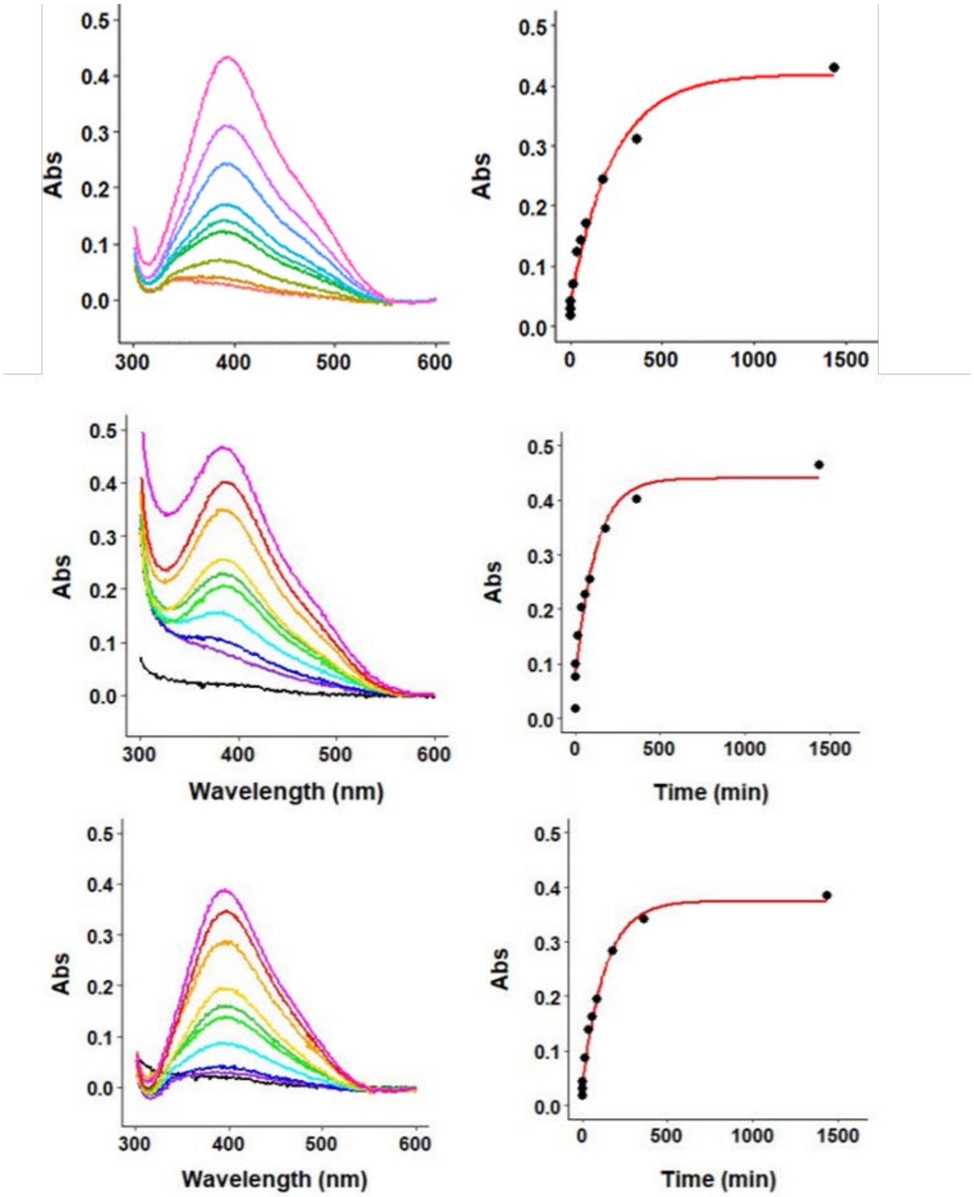

Figure 4.9 Oxidation of CusF PHM M-site models, M49H (top), Se-Met (middle) and His_3 (bottom) with oxygenated buffer at 400 nm over 24 hours. The reaction was sampled at 0 min (black), 1 min (purple), 5 min (blue), 15 min (cyan), 40 min (green), 60 min (dark green), 90 min (yellow), 180 min (gold), 360 min (red) and 1440 min (pink). (b) Absorption at 400 nm plotted versus time fit to a single exponential.

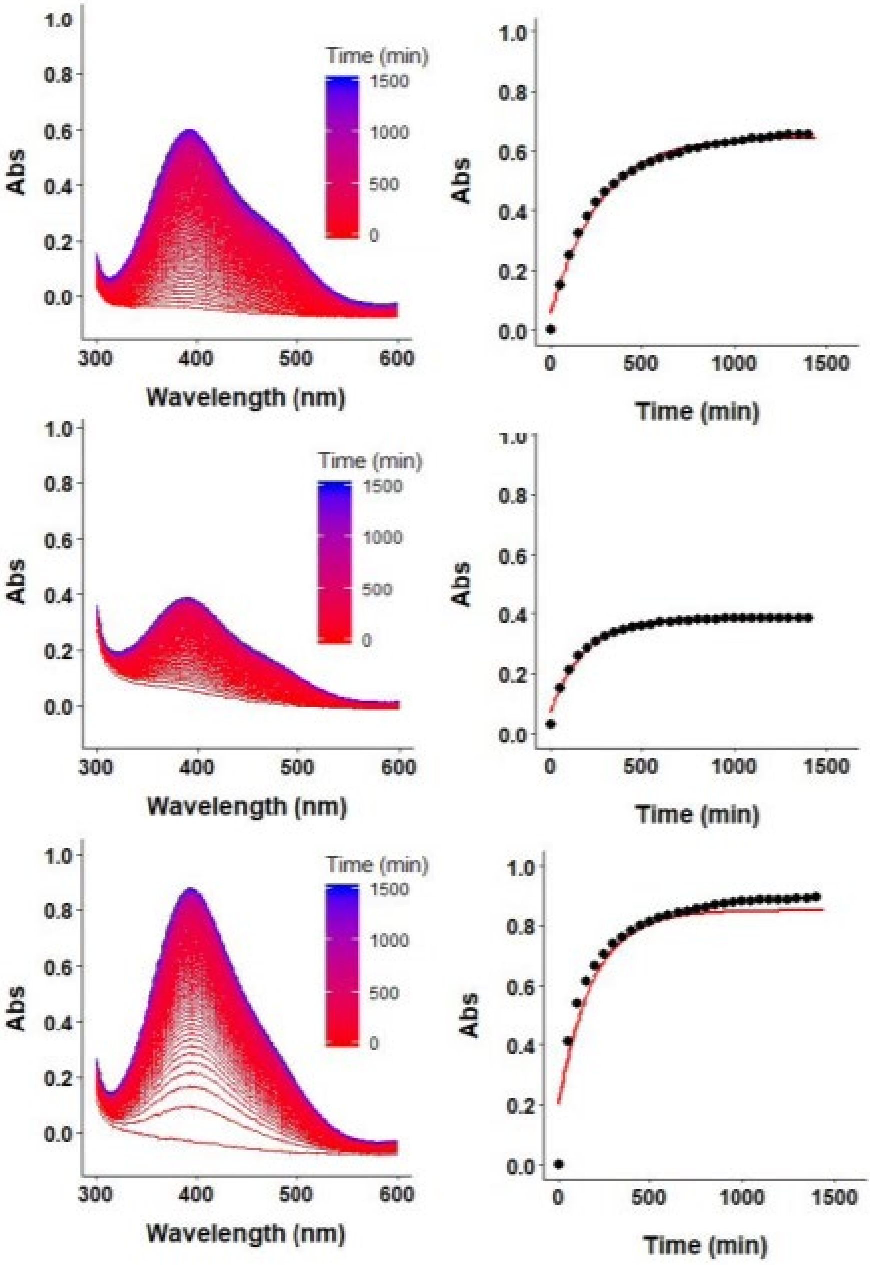

Figure 4.10 Oxidation kinetics of the reduced CusF M-site model variants measured in the presence of 100 mM sodium azide and monitored by formation of the Cu(II) azido complex at 400 nm. The reaction conditions differ from those reported in Figure 4.9 in that azide is present throughout the complete time course, rather than being added to aliquots after sampling. First order rate constants are as follows: M49H (top traces) 6.3 x 10-5 s^{-1}, Se-Met-M49H (middle) 9.5 x 10-5s $^{-1}$, and M47HM49H (His$_3$) (bottom) 9.0 x 10-5 $^{s-1}$. Comparison with data in Table 4.3

shows little effect for the M49H, and a percent decrease of 33 and 30 for the Se-Met and His_3 variants respectively.

Rates of reduction of the azido adducts by ascorbate (stopped flow). We also determined the rates of reduction of the oxidized azido derivatives by ascorbate. The rates of reduction by ascorbate were much more rapid than the corresponding rates of oxidation, and required the use of stopped flow. Because the speciation of the azido adducts is largely homogeneous, the rate constants should follow the relative value of the redox potentials of each derivative, and lead to an assessment of the role of the S/Se-Met ligand in setting this potential. Figure 4.11 shows data for the parent S-Met derivative fit to a single exponential decay, while similar data for Se-Met and His_3 derivatives are also shown. Rate constants are listed in Table 4.3. Whereas all three derivatives undergo rapid reduction, thio- or selenoether ligation appears to provide less stabilization of the Cu(I) state than histidine, with the Se-Met derivative exhibiting the slowest rate of reduction, and the His_3 being almost ten times faster. This result is notable since it excludes redox stabilization of the Cu(I) state in PHM/DβM by methionine as a rationale for the essential role of Met over His in catalysis.

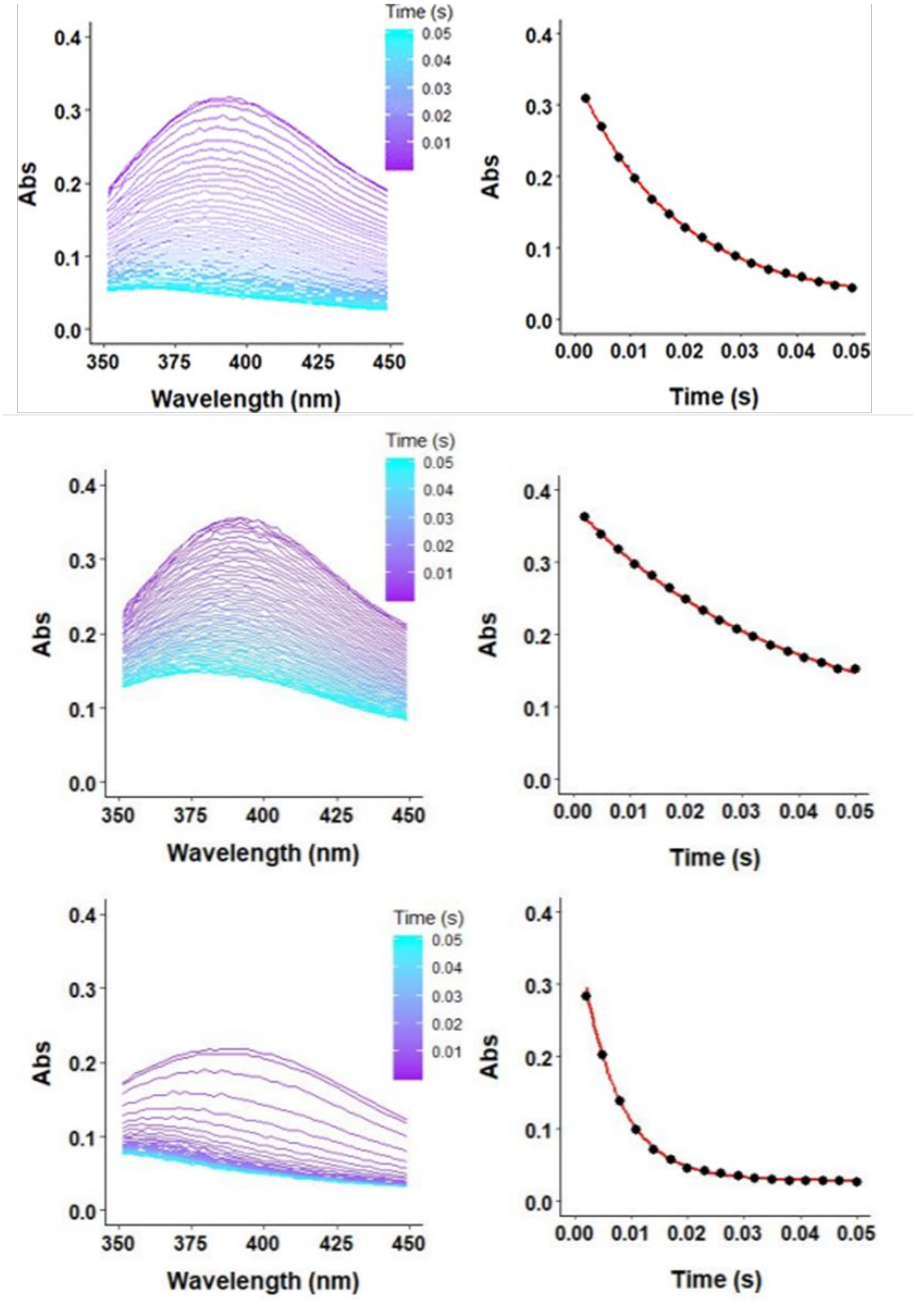

Figure 4.11 Stopped-flow measurements of the reduction of oxidized CusF M-site model variants, M49H (top), Se-Met (middle) and His$_3$ (bottom) with a 5X excess of buffered ascorbate. The resulting absorbance at 400 nm was plotted versus time fit to a single exponential decay with rate constants as listed in Table 4.3.

4.3 Conclusions

Using a rationally designed protein model complex we have investigated the effect of methionine mutation on the reaction chemistry of the His_2Met ligand set that is central to the catalytic activity of mononuclear copper monooxygenases PHM and DβM. Selenomethionine substitution coupled to XAS at the Se edge has provided a unique description of thioether/selenoether coordination which when correlated with Cu EXAFS, has led to an accurate description of the His_2Met reaction center. The approach has determined that the M-site model is 3-coordinate in the Cu(I) state with a highly fluxional Cu-S(Met) bond, and increases to tetragonal 5-coordinate with a long axial Met ligand in the Cu(II) state. Histidine substitution is also informative particularly since the Met to His mutation eliminates activity in the enzymes. Comparison of His with Met has shown that thioether coordination has little effect on redox chemistry, nor does it alleviate the sluggish reactivity of the His_2Met ligand set towards oxygen. These observations provide insights into the role of the Met ligand that have been difficult to determine from studies of the enzymes themselves on account of the overlapping spectroscopic signals and reactivity of the CuH and CuM centers.

The 3-coordinate description of the M center is based on the following three pieces of evidence: (i) the absorption edges are characteristic of 3-coordination (ii) EXAFS analysis does not support the presence of more than 3 ligands, one of which is the thio- or selenoether and (iii) adduct formation with CO increases the coordination number to 4, supported by both the overall EXAFS analysis and the observed increase in Cu(I)-S or Cu(I)-Se distance in the carbonyl models. Indeed the availability of data from both Cu and Se K EXAFS analysis of the Se-Met derivative provides compelling evidence for this increase, which is expected to accompany coordination expansion. Additionally, solution data on the oxidized states of the model and its S/Se derivatives are only consistent with 5-coordinate (His)2 (O/N)2X coordination with X=S(Met) or Se(Met) occupying an axial position. The latter result reproduces the conformational change from a 3-coordinate distorted trigonal Cu(I) to a 5-coordinate tetragonal Cu(II) state that has been documented by us and others for the M-center in the enzymes (Blackburn et al., 1991; Blackburn et al., 2000; Chauhan et al., 2014; Chen et al., 2004). Importantly, the copper coordination of the His_2Met ligand set determined from the model chemistry contrasts sharply with that determined from PHM crystal structures. The crystallographic description of the Cu(I)M site in PHM as visualized in the ascorbate reduced enzyme is 4-coordinate tetrahedral with 2 His, 1 Met and a water ligand while in the oxy form, the water ligand is replaced by a diatomic (Prigge et al., 1999; Prigge et al., 2004). Computational studies have used the crystallographic structures as the starting point for calculations that support end-on cupric superoxo reactive intermediates that progress along a reaction coordinate with attainable activation barriers and overall exergonic thermodynamics 61. These approaches have been remarkably insightful in delineating a canonical reaction mechanism in which a CuM superoxo abstracts a H atom from bound substrate to generate a substrate-based radical followed by radical rebound and a second electron transfer from CuH. However, their validity rests on whether the M-site structures depicted in the crystal structures are representative of the active forms of the solution structures. Our data reported here as well as a substantial body of spectroscopic data (Bauman et al., 2011; N. J. Blackburn et al., 1991; Blackburn et al., 2000; Chen et al., 2004; Jaron & Blackburn, 1999) on the ascorbate-reduced enzymes that fail to observe the coordinated water molecule, suggest significant differences between crystal and solution coordination at the M-site. We also note that to our knowledge computational studies do not provide insight into why replacement of Met with His kills the reactivity.

Next we turn to the reactivity of the Cu(I)-His$_2$Met center with oxygen. First, we note that all three (His)$_2$X Cu(I) model complexes are remarkably resistant to dioxygen oxidation in contrast to expectations based on computational and biomimetic investigations, (Itoh, et al., 2015; Lee & Karlin, 2015) but consistent with reactivity of the enzymes themselves where the Cu(I) state has low reactivity towards oxygen in the absence of substrate (Evans et al., 2006; Kline et al., 2013; Kline & Blackburn, 2016). Sluggish oxygen reactivity in the absence of substrate underscores the need for substrate triggering of catalysis, and understanding how the enzymes achieve substrate dependent oxygen activation remains a key unanswered question. For example, substrate activation may perturb second sphere contacts such as H-bonding that are important for HAA reactivity as highlighted recently in model complexes (Bhadra et al., 2018) and suggested for the unusual thiolate-rich active site of formylglycine generating enzyme (Miarzlou et al., 2019).One possibility supposes that the 5-coordinate tetragonal oxidized M site induces a “facial triad” (comprised of two equatorial His and one axial Met) similar to alpha-keto-glutarate-dependent Fe enzymes (which also show substrate triggering) (Hangasky et al., 2017). This would leave two open equatorial coordination positions allowing the end-on superoxo to adopt a cis configuration with a coordinated solvent which can then H-bond to the proximal O of the superoxide. Computational studies have also hinted that the peroxo intermediate formed after HAA with the bound substrate is bound to Cu(II) in a side-on configuration necessitating cis binding (Cowley et al., 2016).

Alternatively, it may be necessary to undertake a more extensive reexamination of established tenets of the canonical monooxygenase mechanism. An important finding relevant to substrate triggering is the observation that substrate binding (in PHM) red-shifts the M-site Cu(I)-CO stretching frequency by 30 cm^{-1} from 2093 to 2063 cm^{-1} (Kline & Blackburn, 2016). In the M314H mutant substrate binding shifts the frequency to 2052 cm^{-1} a value well below any mononuclear CuN_3CO species reported for copper proteins (Jaron & Blackburn, 1999) or models, (Pasquali & Floriani, 1983; Sanyal et al., 1993) and in the range for binuclear Cu(I)-CO species such as hemocyanin and tyrosinase (Fager & Alben, 1972; Lucas & Karlin, 2009). Red shifted CO frequencies are also observed for the bridging CO ligands of the H cluster of hydrogenase (Kuchenreuther et al., 2011). These observations are relevant to recent crystal structures of both PHM (Maheshwari et al., 2018) and DβM (Vendelboe et al., 2016) which have documented the existence of "closed" conformations of the active site where the separation between CuH and CuM centers shrinks from 11 to 4 Å. Therefore it is possible that substrate binding to the ascorbate-reduced enzyme could trigger an open to closed conformational change which would result in the red-shifted (semi-bridging) ν(C≡O) and activate oxygen via binding to the resulting dinuclear Cu(I) center. Our laboratory is engaged in exploring this chemistry as an alternative mechanistic pathway.

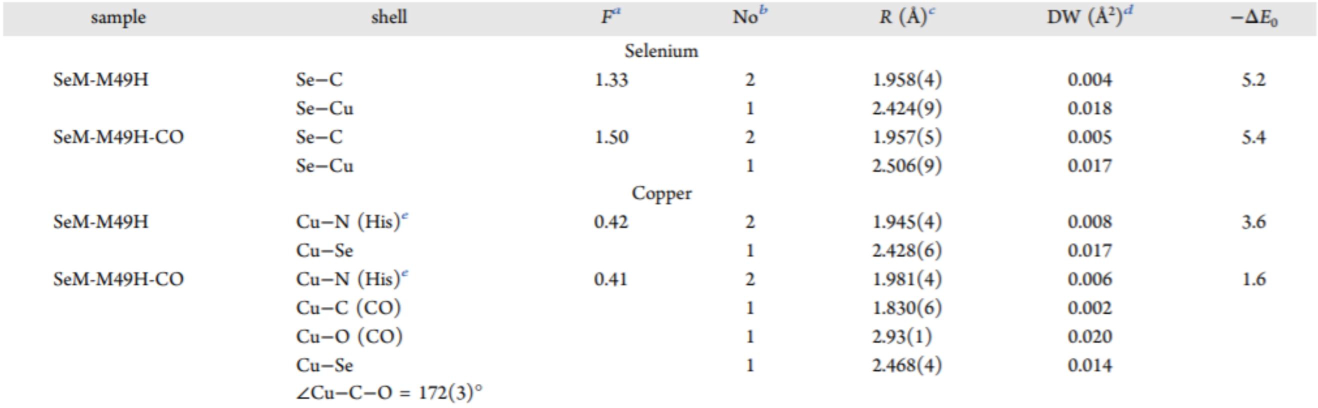

sample	shell	F^a	No^b	R (Å)^c	DW (Å^2)^d	$-\Delta E_0$
			Selenium			
SeM-M49H	Se−C	1.33	2	1.958(4)	0.004	5.2
	Se−Cu		1	2.424(9)	0.018	
SeM-M49H-CO	Se−C	1.50	2	1.957(5)	0.005	5.4
	Se−Cu		1	2.506(9)	0.017	
			Copper			
SeM-M49H	Cu−N (His)^e	0.42	2	1.945(4)	0.008	3.6
	Cu−Se		1	2.428(6)	0.017	
SeM-M49H-CO	Cu−N (His)^e	0.41	2	1.981(4)	0.006	1.6
	Cu−C (CO)		1	1.830(6)	0.002	
	Cu−O (CO)		1	2.93(1)	0.020	
	Cu−Se		1	2.468(4)	0.014	
	∠Cu−C−O = 172(3)°					

Table 4.1 Fits obtained to the Se and Cu K EXAFS of the Cu(I)-Se-Met-M49H derivative of the CusF M-site model.

[a] F is a least-squares fitting parameter defined as $F^2 = \frac{1}{N}\sum_{i=1}^{N} k^6 (Data - Model)^2$ where N is the number of data points and *k* is the photoelectron wave vector defined as $k= 2\pi/h\sqrt{(2m_e(E-E_0))}$.

[b] Coordination numbers are generally considered accurate to ± 25%.

[c] Errors in bond lengths are reported as 95% confidence limits as determined from the least squares analysis. This underestimates the true error in the distances due to experimental factors such as finite data range, errors in the phase shifts, and choice of ΔE_0 which are strongly correlated with R. True errors are probably closer to 0.02 Å for first-shell (coordinated) ligands and 0.05 Å for outer-shell (non-coordinated) ligands.

[d] Debye-Waller terms (DW) are calculated as $\exp(-2\sigma^2 k^2)$ and reported as values of $2\sigma^2$ (Å^2).

[e] Fits included both single and multiple scattering contributions from the imidazole ring.

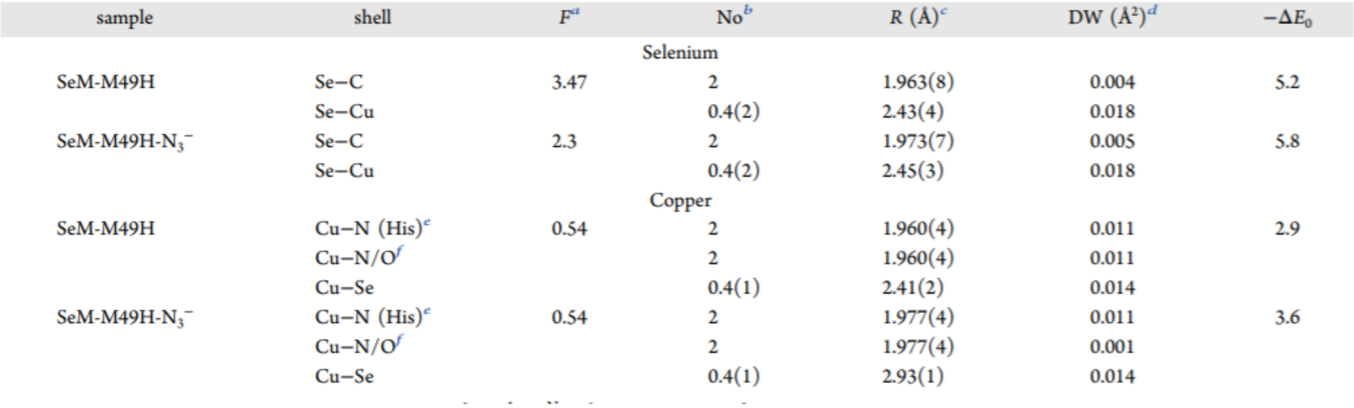

sample	shell	F[a]	No[b]	R (Å)[c]	DW (Å^2)[d]	$-\Delta E_0$
			Selenium			
SeM-M49H	Se−C	3.47	2	1.963(8)	0.004	5.2
	Se−Cu		0.4(2)	2.43(4)	0.018	
SeM-M49H-N_3^-	Se−C	2.3	2	1.973(7)	0.005	5.8
	Se−Cu		0.4(2)	2.45(3)	0.018	
			Copper			
SeM-M49H	Cu−N (His)[e]	0.54	2	1.960(4)	0.011	2.9
	Cu−N/O[f]		2	1.960(4)	0.011	
	Cu−Se		0.4(1)	2.41(2)	0.014	
SeM-M49H-N_3^-	Cu−N (His)[e]	0.54	2	1.977(4)	0.011	3.6
	Cu−N/O[f]		2	1.977(4)	0.001	
	Cu−Se		0.4(1)	2.93(1)	0.014	

Table 4.2 Fits obtained to the Se and Cu K EXAFS of the Cu(II)-Se-Met-M49H derivatives of the CusF M-site model.

[a] F is a least-squares fitting parameter defined as $F^2 = \frac{1}{N}\sum_{i=1}^{N} k^6 (Data - Model)^2$ where N is the number of data points and k is the photoelectron wave vector defined as $k = 2\pi/h\sqrt{(2m_e(E-E_0))}$.

[b] Coordination numbers are generally considered accurate to ± 25%.

[c] Errors in bond lengths are reported as 95% confidence limits as determined from the least squares analysis. This underestimates the true error in the distances due to experimental factors such as finite data range, errors in the phase shifts, and choice of ΔE_0 which are strongly correlated with R. True errors are probably closer to 0.02 Å for first-shell (coordinated) ligands and 0.05 Å for outer-shell (non-coordinated) ligands.

[d] Debye Waller terms (DW) are calculated as $\exp(-2\sigma^2 k^2)$ and reported as values of $2\sigma^2$ (Å^2).

[e] Fits included both single and multiple scattering contributions from the imidazole ring.

[f] In cases where the resolution ΔR for split histidine and non-histidine shells is less than the theoretical resolution of the data (π/2k), histidine and non-histidine scatterers are simulated as a single shell.

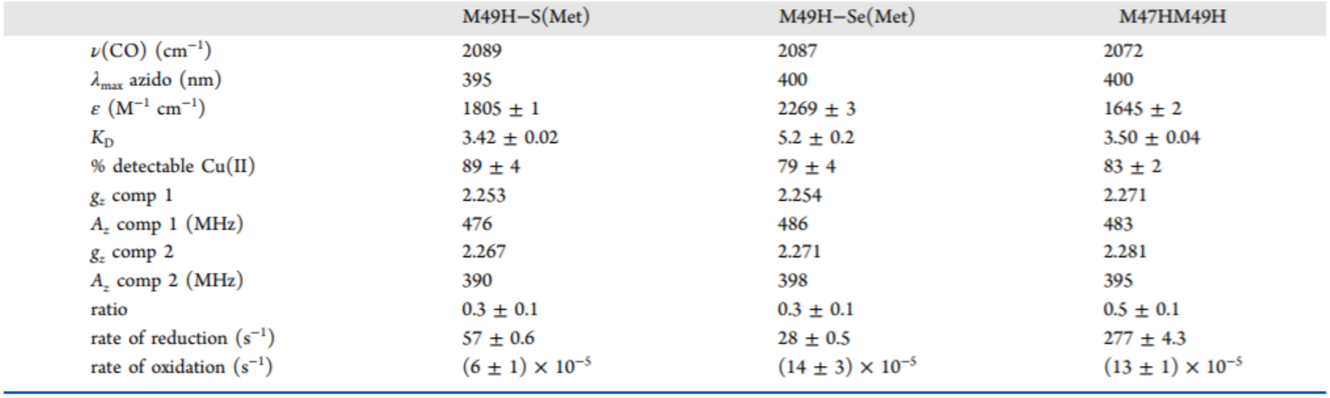

	M49H−S(Met)	M49H−Se(Met)	M47HM49H
ν(CO) (cm^{-1})	2089	2087	2072
λ_{max} azido (nm)	395	400	400
ε (M^{-1} cm^{-1})	1805 ± 1	2269 ± 3	1645 ± 2
K_D	3.42 ± 0.02	5.2 ± 0.2	3.50 ± 0.04
% detectable Cu(II)	89 ± 4	79 ± 4	83 ± 2
g_z comp 1	2.253	2.254	2.271
A_z comp 1 (MHz)	476	486	483
g_z comp 2	2.267	2.271	2.281
A_z comp 2 (MHz)	390	398	395
ratio	0.3 ± 0.1	0.3 ± 0.1	0.5 ± 0.1
rate of reduction (s^{-1})	57 ± 0.6	28 ± 0.5	277 ± 4.3
rate of oxidation (s^{-1})	(6 ± 1) × 10^{-5}	(14 ± 3) × 10^{-5}	(13 ± 1) × 10^{-5}

Table 4.3 Spectroscopic and kinetic data for ligand complexes of M49H and M47HM49H model complexes. Standard error shown as ± values.

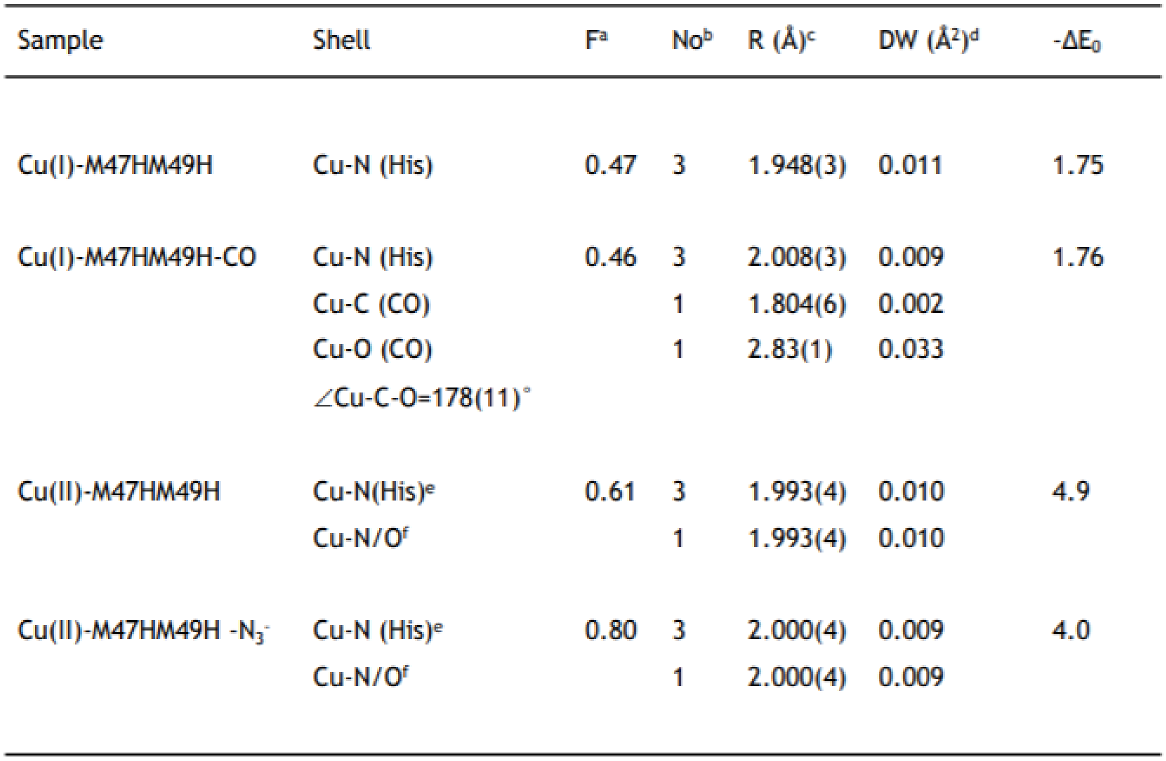

Sample	Shell	F[a]	No[b]	R (Å)[c]	DW ($Å^2$)[d]	-ΔE_0
Cu(I)-M47HM49H	Cu-N (His)	0.47	3	1.948(3)	0.011	1.75
Cu(I)-M47HM49H-CO	Cu-N (His)	0.46	3	2.008(3)	0.009	1.76
	Cu-C (CO)		1	1.804(6)	0.002	
	Cu-O (CO)		1	2.83(1)	0.033	
	∠Cu-C-O=178(11)°					
Cu(II)-M47HM49H	Cu-N(His)[e]	0.61	3	1.993(4)	0.010	4.9
	Cu-N/O[f]		1	1.993(4)	0.010	
Cu(II)-M47HM49H -N_3^-	Cu-N (His)[e]	0.80	3	2.000(4)	0.009	4.0
	Cu-N/O[f]		1	2.000(4)	0.009	

Table 4.4 Fits obtained to the Cu K EXAFS of the Cu(I) and Cu(II)-M47HM49H (His_3) derivatives of the CusF M-site model.

[a] F is a least-squares fitting parameter defined as $F^2 = \frac{1}{N}\sum_{i=1}^{N} k^6 (Data - Model)^2$ where N is the number of data points and k is the photoelectron wave vector defined as $k = 2\pi/h\sqrt{(2m_e(E-E_0))}$.

[b] Coordination numbers are generally considered accurate to ± 25%.

[c] Errors in bond lengths are reported as 95% confidence limits as determined from the least squares analysis. This underestimates the true error in the distances due to experimental factors such as finite data range, errors in the phase shifts, and choice of ΔE_0 which are strongly correlated with R. True errors are probably closer to 0.02 Å for first-shell (coordinated) ligands and 0.05 Å for outer-shell (non-coordinated) ligands.

[d] Debye Waller terms (DW) are calculated as $\exp(-2\sigma^2 k^2)$ and reported as values of $2\sigma^2$ ($Å^2$).

[e] Fits included both single and multiple scattering contributions from the imidazole ring.

[f] In cases where the resolution ΔR for split histidine and non-histidine shells is less than the

theoretical resolution of the data (π/2k), histidine and non-histidine scatterers are simulated as a single shell.

Chapter 5: Cu(I)-Trp cation-π interaction within metallochaperone CusF fine-tunes selectivity and protects Cu(I)-binding site

5.1 Introduction

Copper presents a bilateral challenge for both eukaryotic and prokaryotic cells, as copper is both an essential and toxic micronutrient. This is exemplified at the host-pathogen interface where eukaryotic hosts exploit Cu(I) toxicity against invading pathogenic bacteria and, in turn, pathogens have coevolved defense strategies conferring virulence (Fu et al., 2014), including the highly specific multiprotein export pump CusCBAF. The CusCBAF export pump, expressed by gram-negative bacteria, is part the resistance-nodulation-division (RND) family of heavy metal exporters (Mealman, Blackburn, et al., 2012). Under anaerobic conditions or high levels of copper stress, the Cus components are expressed after Cu-sensing membrane-associated histidine kinase (CusS) senses copper at zeptamolar concentrations activating the cytoplasmic transcription factor CusR. The *cus* operon encodes four structural genes, with CusC, CusB and CusA forming a tripartite complex which spans the periplasmic space, and imparts resistance to both Ag(I) and Cu(I) (Franke et al., 2001, 2003; Kittleson et al., 2006). CusA is a homotrimer (MW 115 kD, 1047 amino acids (aa)) made up of 12 transmembrane helices per monomer and two periplasmic domains, one of which contains the Cu(I)-binding Met(S)$_3$ ligand set. The trimer binds six molecules of the adaptor protein CusB (44 kD, 407 aa), whose N-terminal Met(S)$_3$ metal binding site binds one Cu(I) ion (Long et al., 2010; Su, Long, Zimmermann, et al., 2011). The outer membrane protein CusC (51 kD, 460 aa) completes the envelope-spanning tripartite complex interacting with the BA complex to form a funnel-shaped contact, allowing the transported metal to enter the 25 Å diameter pore and move into the extracellular space (Kulathila et al., 2011; Symmons et al., 2009). The fourth gene encodes a small soluble periplasmic metallochaperone

CusF (12.2 kD, 110 aa), which is unique to the *cus* system and has no homologs in the related RND multidrug-resistant exporters (Symmons et al., 2009). The crystal structure of CusF reports a small, 12kDa, copper binding protein made up of five-stranded β-barrel with OB-fold (usually seen in oligonucleotide-binding proteins) and a single unique metal binding site (Loftin et al., 2007; Xue et al., 2008). CusF binds Cu(I) in a Met$_2$His binding environment with a unique a Cu(I)–π interaction between the metal ion and W44, a nearby tryptophan (Loftin et al., 2007; Xue et al., 2008).

The fluorescence of the Cu(I)–π interaction has been studied by O'Halloran and coworkers, who found that the apo CusF exhibits strong fluorescence from this tryptophan at 344 nm when excited at 295 nm, which is fully quenched by the addition of Cu(I) at a 1:1 stoichiometry (Xue et al., 2008). Recent studies from the Blackburn Lab show a similar result by slowly titrating anaerobic apo CusF with Cu(II) sulfate in the presence of 1mM ascorbate. We observed complete quenching of the 344 nm emission of apo CusF at a Cu(I)-to-protein ratio of 1:1. Interestingly, we also observed that as the Cu(I) binds, a new luminescence signal grows in at ~490 nm which forms concomitant with the loss of the 344 nm emission, and exhibits an isosbestic point indicative of conversion of one species (apo CusF) to another (Cu(I) CusF) (Chacón et al., 2018). This phenomenon has also been characterized in the CO complex of Cu(I) hemocyanin which emits at 540 nm when excited between 280 and 330 nm (Finazzi-Agro et al., 1982). as well as the CO adducts of Cu(I) complexes of substituted imidazoles (Sorrell & Borovik, 1986, 1987). These emissions were assigned to the decay of a triplet state which is populated by energy transfer from singlet states arising from the Cu(I)−CO interaction, most likely involving charge transfer from metal to empty π* levels on the CO ligand. It is likely that a similar photophysical mechanism may operate in the Cu(I)-W44 π-cation luminescence involving a charge transfer between the filled d-shell and the π-antibonding levels of the tryptophan six-membered ring system. To further test the premise that the ~490 nm emission is related to a Cu(I)-tryptophan π−acceptor interaction, we examined the luminescence properties of apo and Cu(I)-loaded CusF-W44A which showed no emission with or without added Cu(I). Additionally, an excitation scan of Cu(I)-loaded CusF, parked at ~490 nm, produces a sharp peak at ~296 nm, which corresponds to the canonical Trp excitation. Together these data provide confirmation that the 490 nm emission is both Cu(I) and W44 dependent, adding confidence in the assignment.

The Blackburn Lab has pioneered the use of selenocysteine Cys(Se) (Berry et al., 2003) or selenomethionine Se-Met (Bagai et al., 2007; Chacón et al., 2014b) labeling of the Cu(I)-coordinating Cys(S) or Met(S) ligands in one member of the donor-acceptor pair, which provides a unique Se-Cu feature in the Se K-edge extended X-ray absorption fine structure (EXAFS) spectrum used to follow metal transfer into or out of the Se environment. The Cus system is especially suited for Se-Met labeling as each protein has at least one Cu(I)-binding Met(S) residue. Previous work studying the structure/function relationships in copper transporters has been limited to determining minimal inhibitory metal concentrations on cell growth (MIC values) or by affinity tagging of one component, followed by separation and analysis of the extent of transfer (Huffman & O'Halloran, 2000; Padilla-Benavides et al., 2014; Xiao et al., 2011). Nuclear magnetic resonance (NMR) studies have also been powerful in determining how donor-acceptor pairs interact across specific protein-protein interface and share metal ligands in the transfer intermediate (Banci et al., 2006). However, these studies provide little kinetic information, as direct measurement of rate constants is very challenging due to the similarity of the coordination chemistry of donor and acceptor sites of metal transfer pairs and by the fact that the Cu(I) cargo is invisible to many spectroscopic techniques.

The utility of Se-Met labeling coupled to Cu and Se EXAFS within the Cus system has already been established. In 2008, our lab reported the direct Cu(I) transfer between its partner CusB (Bagai et al., 2008) and in 2014 our lab showed that CusF is required for CusCBA metal export (Chacón et al., 2014b). Selenomethionine labeling was also used to establish a "switch" mechanism for Cus metal export, where CusF senses the periplasmic metal load, and under high flux transfers Cu(I)/Ag(I) to CusB, generating an active CusB conformer which binds to CusA and activates the pump. The activated form can now also accept metal from the CusF chaperone and transport it out of the cell. However, as the periplasmic metal flux falls, back-transfer from CusB to CusF leads to the apo-form of CusB, which can no longer interact with CusA and shuts off further transport (Chacón et al., 2014b). The "switch" mechanism is supported by single molecule fluorescence resonance energy transfer (FRET) studies, which have suggested that the activation mechanism may involve shifting the equilibrium from partially assembled to fully assembled (envelope-spanning) forms of the pump (Santiago et al., 2017). In 2018, our lab combined Se-Met labeled protein X-ray absorption spectroscopy (XAS) and rapid freeze quench (RFQ) sample preparation, allowing for time-resolved tracking of Cu(I) transfer between CusF to CusB and the capture of transient CusF/CusB protein-protein intermediates (Chacón et al., 2018). Copper transfer was found to be biphasic, and can be fit to a mechanistic model where CusF and CusB interact at a rapid rate (k~1 x $10^6 M^{-1} s^{-1}$) to form a protein-protein shared ligand complex intermediate at about 100 ms, with 2 Met(S) ligands from CusB and 1 Se-Met ligand from CusF, followed by a slower ligand rearrangement to fully loaded CusF (k = 0.3 sec^{-1}).

While the function of CusF as metallochaperone is clear, there have only been a few studies investigating the role of its unique Cu(I)-W44 cation-π interaction within the CusF metal binding site. Functional suggestions include protection of the Cu(I) from O_2 oxidation and/or increase in selectivity for Cu(I)/Ag(I), although a role in assisting metal transfer reactivity is also possible. A previous study by the McEvoy Lab in collaboration with the Blackburn Lab investigated the effect of the mutagenesis of residue 44. The structure of $CusF_{WT}$ was compared to that of $CusF_{W44A}$ and $CusF_{W44M}$ using both NMR and XAS (Loftin et al., 2009). NMR HSQC spectra were collected to determine the effects of W44 mutations on CusF structure and metal specificity. The similarities of the spectra to the spectrum of the wild-type protein indicate both $CusF_{W44A}$ and $CusF_{W44M}$ exhibit the native fold and are stable proteins. Additionally, each mutant was reported to bind a metal ion in the same metal binding site as evidenced by chemical shift changes similar to those seen for $CusF_{WT}$. XAS of both the alanine and methionine mutants showed that $CusF_{W44A}$ exhibits a spectrum similar to that reported previously for wild-type CusF with a best fit achieved by one His(N) and two Met(S) ligands. The spectrum produced by $CusF_{W44M}$ is four-coordinate, with a best fit achieved by one His(N) and three Met(S) ligands. Comparison of the edge region for both $CusF_{W44A}$ and $CusF_{W44M}$ suggest that the alanine mutant may be more susceptible to oxidation, where the apparent shift in the absorption edge to higher energy, coupled with the small but significant decrease in intensity at 8,983 eV, may signal a minor population of oxidized copper sites. Thus, the W44 Cu(I)–π interaction or a formal fourth ligand contributed by a methionine protects the Cu(I) from oxidation. The binding affinity for each mutant was also determined using competition assays. They found that $CusF_{W44A}$ has a similar Cu(I) affinity compared to $CusF_{WT}$ and that $CusF_{W44M}$ has 2-fold increase in affinity. This study indicates that W44 may be involved in Cu(I) affinity as well as protection and maintenance of the three-coordinate Cu(I) binding environment. To further investigate the function of the unusual Cu(I)-W44 cation-π interaction found in the metal binding site of CusF, we have used an array of advanced spectroscopic methods to monitor changes in (i) structure, (ii) accessibly, (iii) Cu(I) specificity and (iv) metal transfer to CusB as a result of changes to residue 44 interrupting the Cu(I)-W44 cation-π interaction.

5.2 Materials and Experimental Details

Construction of CusF mutants. The CusF$_{W44A}$, CusF$_{W44F}$ and CusF$_{W44M}$ mutations were introduced into CusF$_{6\text{-}88}$ M8IM59I trx-his6-tev sequence (both non-coordinating Met residues mutated to Ile), as previously described in Section 3.2.

Expression and purification of CusF and CusB proteins. Both Met(S) and Se-Met labeled CusF and CusB proteins were expressed and purified and reconstituted with Cu(I) as previously described in Sections 3.2 and 4.2. After purification, both proteins were dialyzed into in 50mM HEPES buffer pH 7.5 and either immediately used as apo protein (CusB) or reconstituted with copper (CusF).

Sample preparation of Cu(I)-loaded CusF. CusF was reconstituted with Cu(I) in a COY chamber by adding tetrakis(acetonitrile)copper(I) hexafluorophosphate dissolved in pure acetonitrile as a bolus, at a ratio of 1.5:1 metal to protein. The mixture was then allowed to incubate for 1.5 hours with stirring, on ice. The Cu(I)-loaded protein was concentrated to the desired volume using a microconcentrator, and three cycles of desalting were accomplished using spin columns that had been equilibrated with HEPES buffer containing 10%, 5%, and 0% acetonitrile, which removed excess metal and salt from the proteins. Metal-to-protein concentrations were verified by ICP-OES and the BCA assay.

Sample preparation of Cu(II)-loaded CusF. The protein was reconstituted with $CuSO_4$ at a ratio of 2.5:1 via syringe pump (25 µL/h). The mixture was then allowed to incubate on ice for 1 hour with stirring. Excess Cu(II) was removed by overnight dialysis in 50 mM HEPES, pH 7.5 with 10uM $CuSO_4$. Metal-to-protein concentrations were verified by ICP-OES and BCA assay.

X-ray Absorption spectroscopy sample preparation. Samples were mixed with 20% (vol/vol) ethylene glycol, loaded into sample cells and frozen in LN_2.

Rapid freeze quench sample preparation. Apo Se-Met CusB was mixed with Cu(I)-loaded CusF using a Quench Flow-3 apparatus (KinTek) configured for RFQ by the manufacturer, at

24° C. Both proteins were prepared in 50mM HEPES pH 7.5 with 5% ethylene glycol at final mixture protein concentrations of 1200 μM CusF and 600 μM CusB, resulting in a 2:1 final mixture, and loaded anaerobically onto the apparatus via gastight syringe and rapidly mixed at the desired time point. Mixtures were quenched by liquid ethane maintained at −170 °C and the resulting snow packed firmly into machined RFQ-XAS cuvettes. The cuvettes were then further frozen in liquid nitrogen as a glassed snow for EXAFS experiments. The time resolution of the experiment was estimated to be 13 milliseconds.

Spectroscopic Data Collection and Processing

XAS, FTIR, azide titrations, oxidation by O_2 and stopped-flow spectrophotometry of ascorbate reduction data were collected and processed as previously described in Section 3.2 and 4.2.

5.3 Results and Discussion

In previous work, our lab and others reported the effects of mutagenesis of the W44 ligand in the Cu(I) binding site of CusF (Loftin et al., 2009). In this study we investigated the effect of disrupting the Cu(I)-W44 interaction by substituting the tryptophan at position 44 with alanine, phenylalanine and methionine in terms of (i) structure, (ii) accessibly, (iii) Cu(I) specificity and (iv) metal transfer to CusB. The $CusF_{W44A}$ construct is expected to form a "cap-off" metal binding site, while $CusF_{W44M}$ will have a 4-coordinate binding environment as previously reported (Loftin et al., 2009). $CusF_{W44F}$, a non-W aromatic, may be more similar to $CusF_{WT}$. Both Cu(I) and Cu(II) complexes of $CusF_{WT}$ and its W44 variants could be prepared by incubating apoprotein with a small excess of either $[Cu(I)(CH_3CN)_4]^+$ under anaerobic conditions or aqueous Cu(II) salts, followed by desalting to remove excess metal ions. Cu(I) complexes could also be prepared by ascorbate reduction of the Cu(II) species. Both Cu(I) and Cu(II) complexes formed with a simple 1:1 stoichiometry.

Structural characterization of Cu(I)-loaded CusF by Cu EXAFS. Both $CusF_{WT}$ and its W44 variants bind Cu(I) in a 1:1 ratio of protein to copper ion as measured by ICP-OES. In the initial study identifying the Cu(I)-W44 cation-π interaction, $CusF_{WT}$ produced a Fourier transform (FT) and EXAFS, with the best fit to two Met(S) at 2.26 Å and one His(N) at 1.97 Å (Loftin et al., 2007). Follow up XAS studies on $CusF_{W44A}$ and $CusF_{W44M}$ produced spectra with a best fit of two Met(S) at 2.32 Å and one His(N) at 2.02 Å and three Met(S) at 2.31 Å and one His(N) at

2.05 Å, respectively (Loftin et al., 2009). Figure 5.1 shows FT and EXAFS of reduced (a) $\mathrm{CusF_{W44A}}$, (b) $\mathrm{CusF_{W44F}}$ and (c) $\mathrm{CusF_{W44M}}$. As expected, the Cu(I)-loaded $\mathrm{CusF_{W44A}}$ (cap-off) variant produced a spectrum most similar to $\mathrm{CusF_{WT}}$ with a best fit to two Met(S) at 2.25 Å and one His(N) at 1.92 Å. The phenylalanine at position 44 also had little effect on the $\mathrm{Met_2His}$ structure observed in $\mathrm{CusF_{WT}}$ and $\mathrm{CusF_{W44A}}$. In the $\mathrm{CusF_{W44M}}$, a third methionine forms a 4-coordinate metal binding site with three Met(S) at 2.32 Å and one His(N) at 2.00 Å. All experimental fits are listed in Table 5.1.

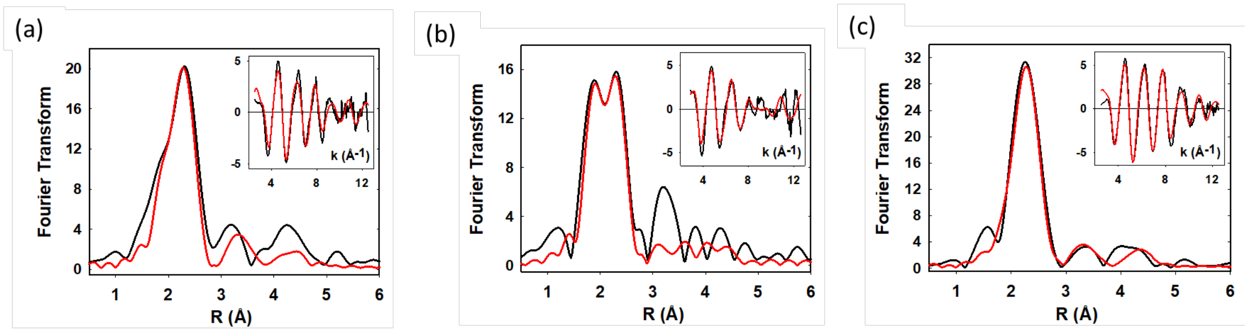

Figure 5.1 Fourier transforms and EXAFS (insets) of the Cu(I)-loaded (a) $\mathrm{CusF_{W44A}}$ (b) $\mathrm{CusF_{W44F}}$, and (c) $\mathrm{CusF_{W44M}}$. Black traces are experimental data, and red traces are simulations using EXCURVE 9.2. Parameters used in fitting the data are listed in Table 5.1.

CO access to Cu(I) binding site. One suggested function of the Cu(I)-W44 interaction is protection from exogenous ligands such as CO and/or oxidation from O_2 molecules. Here we use CO to investigate the degree of exogenous ligand access to the Cu(I) binding site of $\mathrm{CusF_{WT}}$ and its W44 variants. To measure the effect of Cu(I)-W44 interaction on CO accessibility we tested the ability of $\mathrm{CusF_{WT}}$ and its W44 variants to form a Cu(I)carbonyl complex, measured by FTIR. The $\mathrm{CusF_{W44A}}$ Cu(I)carbonyl v(CO) peak at 2108 cm^{-1} and the highly attenuated v(CO) $\mathrm{CusF_{WT}}$ peak at 2103 cm^{-1} are shown in Figure 5.2a. Together these data suggest that the Cu(I)-W44 interaction does function to block exogenous ligands, including CO, from accessing the Cu(I) ion. Additionally, neither $\mathrm{CusF_{W44M}}$ or $\mathrm{CusF_{W44F}}$ formed distinct Cu(I)carbonyl complexes, which is consistent with the “capping” ligand restricting access as M44 forms a 4-coordinate site not able to bind CO. F44 is a bulky ligand, like its Trp homolog, which may inhibit CO binding. The $\mathrm{CusF_{W44A}}$ Cu(I)carbonyl was also confirmed by XAS, shown in Figure 5.2b. The experimental data can be modeled by Cu−C bond distances of 1.82 Å, with a Cu−C−O angle close to linearity and a Cu−Met(S) distance of 2.31 Å. Fitting parameters used in the simulations can be found in Table 5.1. As XAS produces an average of all complexes present at the time of freezing, it was not possible to perform XAS on the native CusF carbonyl as the spectra would be dominated by the Cu(I) complex.

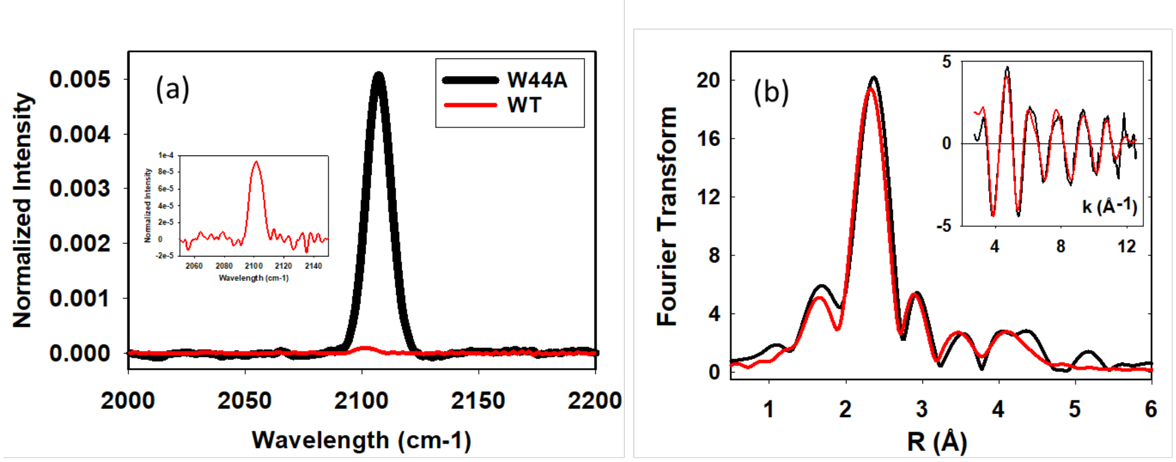

Figure 5.2 (a) Fourier transform infrared spectra of the CO complexes formed by CusF$_{WT}$ (red) and CusF$_{W44A}$ (black). Inset shows CusF$_{WT}$ spectrum. CusF$_{W44M}$ and CusF$_{W44F}$ did not produce a ν(CO) after 10 minutes of exposure. Peaks were fit to either one or two Gaussian functions with frequencies and line widths as reported in the text. All data normalized for concentration. (b) Fourier transforms and EXAFS insets of CusF$_{W44A}$ Cu(I)CO. Black traces are experimental data, and red traces are simulations using EXCURVE 9.2. Parameters used in fitting the data are listed in Table 5.1.

Spectral characterization of Cu(II)-loaded CusF. In previous work (Alwan et al., 2019a) we engineered and characterized CusF with a His$_2$Met copper binding site as a model for the catalytic CuM site of cuproenzyme PHM. Unlike the Met$_2$His binding site of metallochaperone CusF, the engineered His$_2$Met binding site is known to bind both cuprous and cupric ions. Unlike cuprous ions, cupric ions form well-characterized Cu(II)-azido complexes, giving rise to a LMCT band around 400 nm. We have previously used this LMCT band to assess the relative reactivity of the His$_2$Met model binding site (Alwan et al., 2019a). In subsequent work we also used azide (N_3^-) as a reporter to characterize redox chemistry of the Se-Met labeled His$_2$Met site and the His$_3$ site (Alwan et al., 2019b). In all cases the Cu(II) center formed a 1:1 Cu(II)-azido complex and underwent slow (hrs) oxidation compared with fast (ms) reduction. In order to gain insight on the redox chemistry of the $\mathrm{CusF_{WT}}$ copper binding site we prepared Cu(II)-loaded $\mathrm{CusF_{WT}}$ and its W44 variants. All CusF variants including $\mathrm{CusF_{WT}}$ bound Cu(II) 1:1 in the presence of 10 uM excess copper sulfate. All Cu(II)-loaded derivatives reacted with sodium azide and produced a visible LMCT band. Titration data (Figure 5.3) reveals the formation of a Cu(II)-azido complex with a single LMCT band with a λ_{max} that shifts from 350 nm to 400 nm as the N_3^- concentration increased. The $\mathrm{CusF_{W44M}}$ variant produced two discrete peaks at 350 nm and 400 nm. We hypothesize that the 350 nm peak is produced by a Cu(II)-N_3^- adduct while the 400 nm is a bis-N_3^- adduct. The simple 1:1 complexes (λ_{max} 350 nm) were used to find the K_d value for each CusF construct (Figure 5.3). All $\mathrm{Met_2His}$ constructs bound N_3^- poorly, with K_d values of 56 mM, 140 mM, 95 mM, 81 mM, for $\mathrm{CusF_{WT}}$, $\mathrm{CusF_{W44A}}$, $\mathrm{CusF_{W44M}}$ and $\mathrm{CusF_{W44F}}$, respectively.

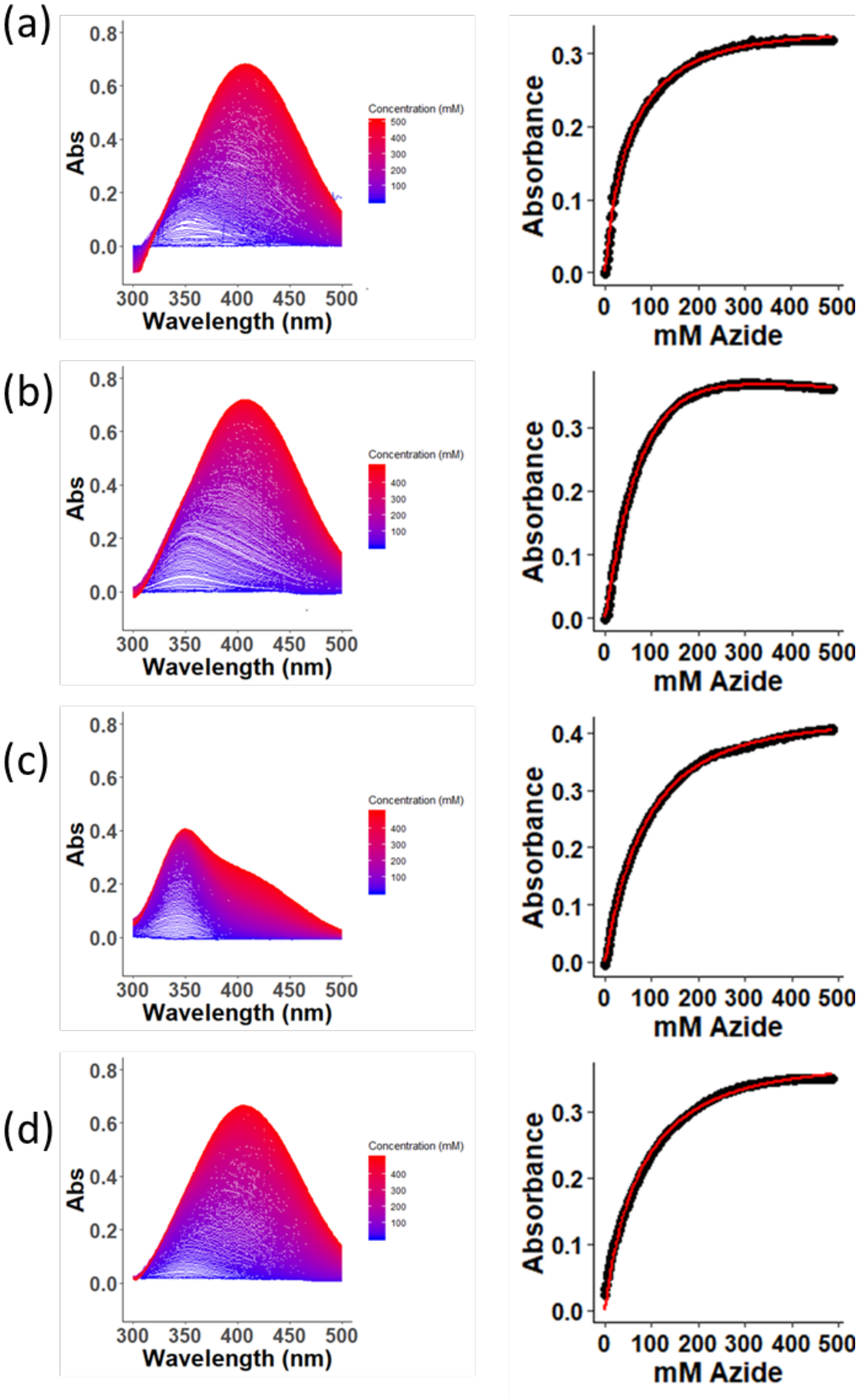

Figure 5.3 Sodium azide titration of the oxidized (a) CusF$_{\text{WT}}$ and its W44 variants: (b) CusF$_{\text{W44A}}$, (c) CusF$_{\text{W44F}}$ and (d) CusF$_{\text{W44M}}$. All Cu(II)N$_3^-$ complexes where modeled using a $\lambda_{\max}$ of 350 nm. Experimental UV/vis data was fit and K$_d$s are reported in text.

Reduction of the Azido Adducts by Ascorbate (stopped flow). To further investigate both of the Cu(II)-azido complexes we measured both the rates of reduction and oxidation rates of Cu(II)-loaded CusF$_{WT}$ and its variants. At low azide concentration, less than 250 mM, the predominant CusF Cu(II)-azido complex produced an LMCT band at 350 nm, which can be used as a tool to assess the relative reactivity of CusF$_{WT}$ and its variants. The rate of reduction by ascorbate was measured in the stopped flow. As shown in Figure 5.4 all Met$_2$His CusF variants underwent reduction on a millisecond timescale with rates similar to the previously measured His$_2$Met constructs (Table 5.2). CusF$_{W44A,}$ which is proposed to be in the “cap-off” state, reduced significantly slower than all three “cap-on” constructs. This suggests that the absence of W44 produces a metal binding site that is more stable in the Cu(II) form, therefore having less selectivity for monovalent Cu(I).

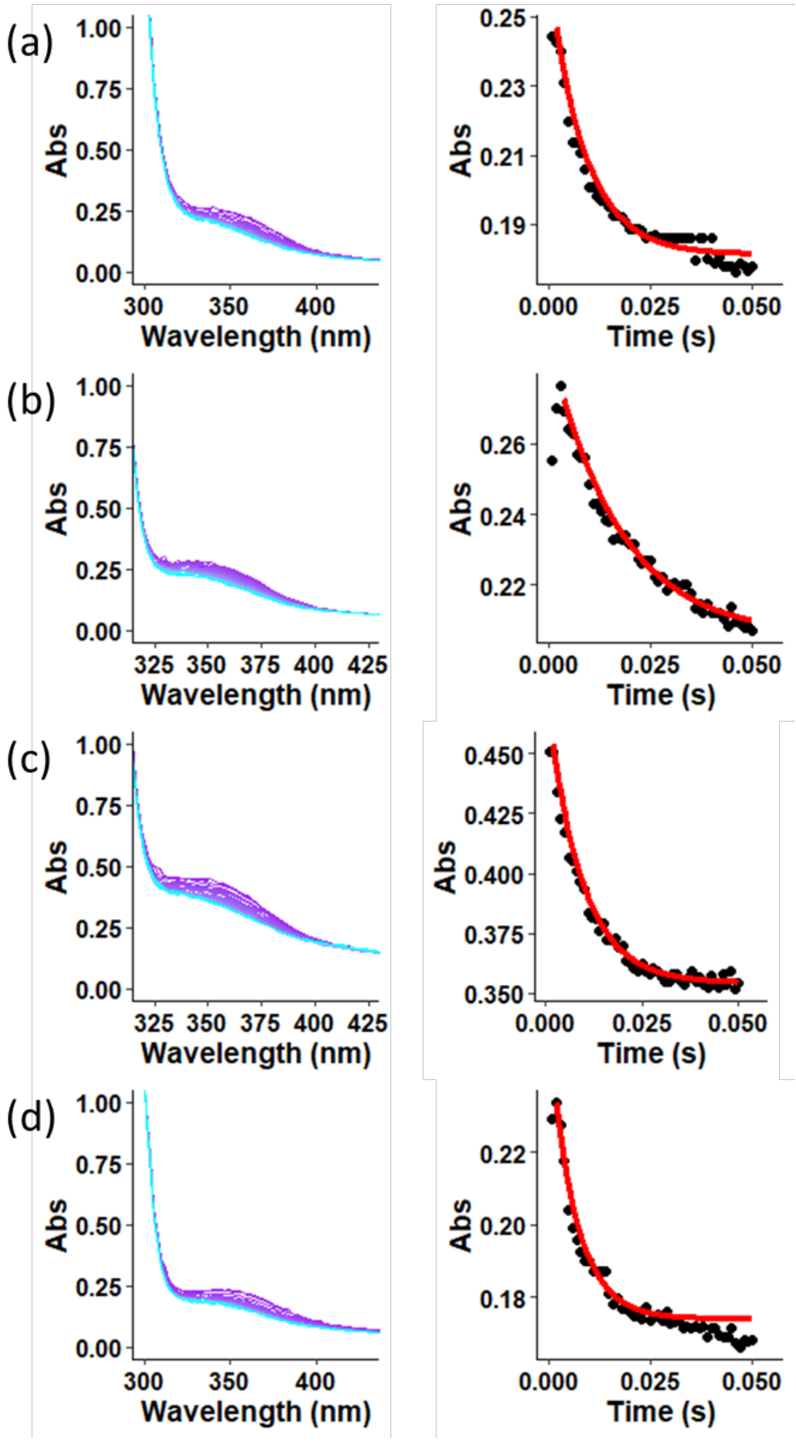

Figure 5.4 Stopped-flow measurements of the reduction of Cu(II) in the presence of 250mM N_3^- for (a) CusF$_{WT}$ and its W44 variants; (b) CusF$_{W44A}$ (c) CusF$_{W44F}$ and (d) CusFW$_{44M}$ with a 5-fold excess of buffered ascorbate at 350 nm over a 50 millisecond reaction time. Data were baseline-

corrected with respect to pure buffer and simulated by a single-exponential decay (right) with rate constants as listed in Table 5.2.

Cu(I) transfer between CusF and CusB measured by RFQ XAS. As discussed in Section 2.6, the Blackburn Lab pioneered the use of Se-Met labeling in combination with XAS in order to add a second probe able to report copper occupancy and transfer. By observing the Fourier transform (FT) spectra derived from the Se EXAFS, specific holo and apo metal binding sites within a given protein can be clearly distinguished, allowing for metal ion transfer to be tracked both from the vantage point of Se as well as from the vantage point of the bound metal ion. In 2018 our lab combined XAS of Se-Met labeled proteins with RFQ sample preparation for time-resolved tracking of metal ion transfer for structural and kinetic information (Chacón et al., 2018). The use of RFQ sample preparation at room temperature made it possible to measure copper occupancy on a millisecond timescale (15 ms to 30 s) and track the rapid Cu(I) transfer between CusF and CusB. The reaction was found to be biphasic with a fast phase complete within 20–50 ms, and a slow phase occurring on the 500 ms to 10 s time scale. The kinetic profile could be fit to a mechanism in which CusF and CusB react in a rapid step ($k \sim 1 \times 10^6$ M^{-1} s^{-1}) to form a protein-protein complex, with the Fourier transform amplitude indicating that the Cu atom is bound to one of the two Se-Met ligands in CusF. CusF subsequently rearranges ($k = 0.3$ s^{-1}) to the final product, fully loaded CusF, with copper bound to both of the Se-Met ligands. In order to determine if the Cu(I)-Trp cation-π effects the rate of Cu(I) transfer between CusF and CusB, we mixed Cu(I)-loaded Met(S) CusF with apo- Se-Met CusB at room temperature, allowing metal transfer to be determined by monitoring the increase in the Se-Cu signal at the Se edge (Figure 5.5).

The data shows that the identity of the capping ligand at position 44 does affect the rate of Cu(I) transfer between CusF and CusB. The observed Cu(I) transfer between Cu(I)-loaded $CusF_{WT}$ and Se-Met-labeled CusB produced a biphasic reaction with a fast phase complete within 20–50 ms and a slow phase occurring on the 500 ms to 10 s time scale, consistent with our finding in 2018 (Chacón et al., 2018). The initial fast phase of Cu(I) transfer between $CusF_{W44A}$ and CusB was 4 times faster than $CusF_{WT}$ with a similar slow phase, with complete transfer by 10 s. Neither $CusF_{W44F}$ or $CusF_{W44M}$ could be fit to a biphasic as the transfer was incomplete for both mutants, with $CusF_{W44M}$ only reaching 40% transfer at 5 s and 70% at 10 s. (Figure 5.5)

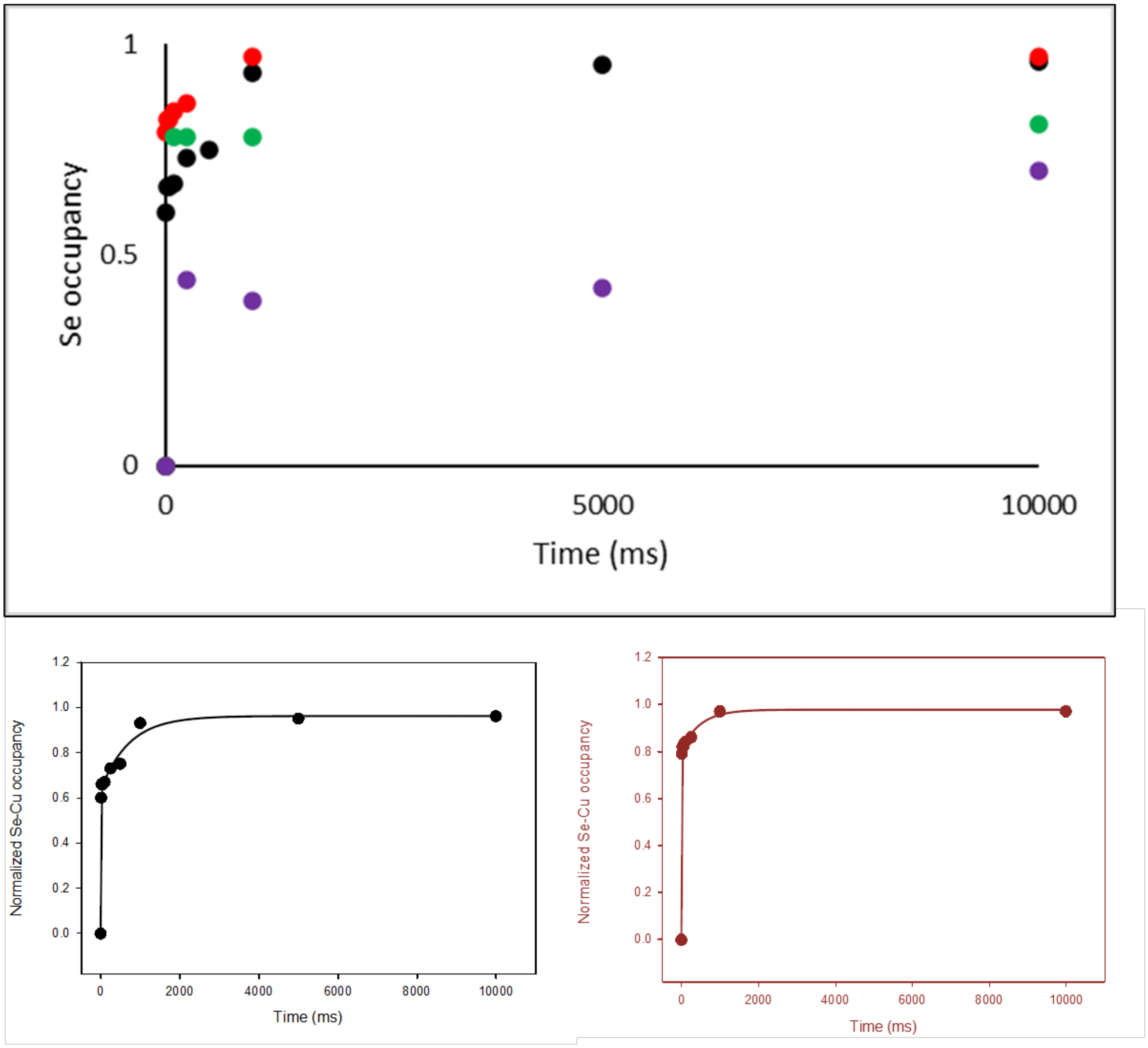

Figure 5.5 (Top panel) Cu(I) transfer between CusF and CusB as determined by Se-Cu occupancy at the Se edge for CusF$_{\mathrm{WT}}$ (black), CusF$_{\mathrm{W44A}}$ (red), CusF$_{\mathrm{W44F}}$ (green), and CusF$_{\mathrm{W44M}}$ (purple). (Bottom panel) The data are simulated for CusF$_{\mathrm{WT}}$ (black) and CusF$_{\mathrm{W44A}}$ (red) by a double exponential rate equation with a fast phase and a slow phase.

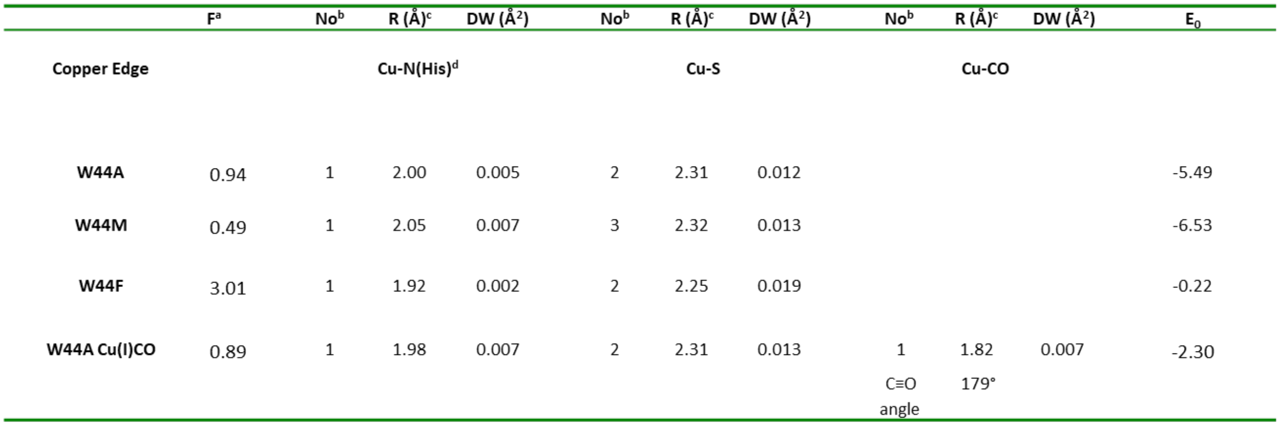

	F[a]	No[b]	R (Å)[c]	DW (Å^2)	No[b]	R (Å)[c]	DW (Å^2)	No[b]	R (Å)[c]	DW (Å^2)	E_0
Copper Edge			**Cu-N(His)[d]**			**Cu-S**			**Cu-CO**		
W44A	0.94	1	2.00	0.005	2	2.31	0.012				-5.49
W44M	0.49	1	2.05	0.007	3	2.32	0.013				-6.53
W44F	3.01	1	1.92	0.002	2	2.25	0.019				-0.22
W44A Cu(I)CO	0.89	1	1.98	0.007	2	2.31	0.013	1	1.82	0.007	-2.30
								C≡O angle	179°		

Table 5.1 Fits Obtained to the Cu(I)-loaded Cu K EXAFS of the CusF W44 variants.

Parameter	WT	W44A	W44M	W44F
v(CO) (cm^{-1})	2103	2018	-	-
max azido (nm)	350	350	350	350
ε at 350nm (M^{-1}cm^{-1})	756	844	824	867
ε at 400nm (M^{-1}cm^{-1})	2078	2057	732	2389
K_d at 350nm (mM)	56	140	95	81
K_{fast} asc 350 nm (sec^{-1})	130 +/- 10.1	59 +/- 3.4	154 +/- 1.2	148 +/- 3.7

Table 5.2 Spectroscopic and Kinetic Data for Ligand Complexes of CusF$_{WT}$ and its W44 variants.

5.4 Conclusions

CusF is a small soluble periplasmic metallochaperone that is produced in excess as part of *cus* operon; it is responsible for either binding or receiving Cu(I) ions in the periplasm and then transporting and transferring its cargo to CusB (for regulation) and CusA (for export). Structural studies of CusF have observed a unique cation-π interaction between the Cu(I) ion and capping a tryptophan W44. As the metal status of CusF plays a major role in CusCBA regulation and function, understanding the function of the Cu(I)-W44 cation-π interaction is of interest. To this end we produced three CusF constructs: CusF$_{W44A}$ (cap-off), CusF$_{W44M}$ (fourth Cu(I)-binding ligand) and CusF$_{W44F}$ (non-Trp-aromatic), and then compared each to CusF$_{WT}$ in terms of (i) structure, (ii) exogenous ligand access and (iii) substrate specificity. We assessed the structure of each Cu(I)-bound construct by XAS and found that all produced the expected Met_2His ligand set, except $CusF_{W44M}$ which bound the excepted fourth Met(S). This was not surprising, as the Cu(I)-W44 in $CusF_{WT}$ cannot be detected outside of the XAS interaction range, but the edge region does show evidence of a fourth ligand (Loftin et al., 2007). We investigated the possible role of exogenous ligand protection by monitoring the formation of Cu(I)-carbonyl complex using FTIR. We were able to show that W44 does block access to exogenous ligands, as only $CusF_{W44A}$ produced a Cu(I)carbonyl with the excepted stretching frequency for a Met_2His Cu(I)carbonyl. We also observed the formation of a highly attenuated Cu(I)carbonyl peak for $CusF_{WT}$, suggesting that a small percent of Cus_{WT} is in the "cap-off" state, simulated by the $CusF_{W44A}$ construct.

Our lab has also engineered and characterized CusF with a His_2Met copper binding site as a model for the catalytic CuM site of cuproenzyme PHM, which was found to bind both cuprous and cupric ions. Unlike cuprous ions, cupric ions form well-characterized Cu(II)-azido complexes, rising to an LMCT band around 400 nm. We previously used this LMCT band to assess the relative reactivity of the His_2Met model binding site (Alwan et al., 2019a), and in subsequent work we also used azide as a reporter to characterize redox chemistry of the Se-Met labeled His_2Met site and the His_3 site (Alwan et al., 2019b). In this work we used the same Cu(II)-azido LMCT band to characterize the Cu(II) adduct and measure the rates of reduction and oxidation. Unlike the His_2Met CusF PHM model, CusF WT and its W44 variants were unstable in the Cu(II) form and all produced spectra with λ_{max} shifting from 350 nm to 400 nm as the N_3^- concentration increased. The W44M variant produced two discrete peaks at 350 nm and 400 nm. We hypothesized that the 350 nm peak is produced by a Cu(I)-N_3^- adduct while the 400 nm is a bis- N_3^- adduct. Using the simple 1:1 azido complex with an LMCT band at 350 nm we measured the rates of reduction by ascorbate using UV/Vis stopped flow spectroscopy. The $CusF_{W44A}$ construct which is proposed to be in the "cap-off" state reduced significantly more slowly than all three "cap-on" constructs. This suggests that W44 does play a role in substrate specificity, as the "cap-off" $CusF_{W44A}$ construct is more stable in the Cu(II) form. Together this data suggests that the Cu(I)-W44 cation-π interaction functions to both protect the Cu(I)-binding from exogenous ligands and increase selectivity for Cu(I) ions, allowing for finely tuned metal delivery with the cell.

Chapter 6: Conclusions and future directions

6.1 Modeling the M-center of PHM

Peptidylglycine monooxygenase (PHM) and dopamine β-monooxygenase (DβM), both of which are mononuclear copper monooxygenases, catalyze the hydroxylation of high energy C-H bonds utilizing a pair of chemically distinct copper sites (referred to as the M- and H- centers) separated by 11 Å. The Blackburn lab has previously constructed single-site PHM variants, designed to allow study of the M- and H-centers independently, in order to place their reactivity sequentially along the catalytic pathway. More recent crystallographic studies suggest that these single-site variants may not be truly representative of the individual active sites.

In Chapter 3 we described the use of rational design to construct an artificial PHM model using a small metallochaperone scaffold that mimics the M-center of PHM. The results show that the model accurately reproduces the chemical and spectroscopic properties of the M-center, including Met(S) coordination, and the properties of Cu(I) and Cu(II) states in the presence of endogenous ligands such as CO and azide. The rate of reduction of the Cu(II) form of the model by the chromophoric reductant N,N'-dimethyl phenylenediamine (DMPD) has been compared with that of the PHM M-center, and the reaction chemistry of the reduced forms with molecular oxygen has also been explored, revealing an unusually low reactivity towards molecular oxygen.

In Chapter 4 we used selenomethionine labeling and a Met-to-His mutation to investigate many unusual attributes of the PHM M site, including an His_2Met ligand set, a fluxional Cu(I)-S(Met) bond, tight binding of exogenous ligands CO and N_3^-, and complete coupling of oxygen reduction to substrate hydroxylation even at extremely low turnover rates. In particular, mutation of the Met ligand to His completely eliminates the catalytic activity despite the propensity of Cu(I)-His_3 centers to bind and activate dioxygen in other metalloenzyme systems. We examined the effects on coordinate structure and exogenous ligand binding via XAS and EPR, and probed the consequences of mutations on redox chemistry through studies of the reduction by ascorbate and oxidation via molecular oxygen. We found that the M-site model is three-coordinate in the Cu(I) state and binds CO to form a four-coordinate carbonyl. In the oxidized forms, the coordination changes to tetragonal five-coordinate with a long axial Met ligand that, like the enzymes, is undetectable at either the Cu or Se K edges. The EXAFS data at the Se K edge of the selenomethionine labeled variant provides unique information about the nature of the Cu-methionine bond, that is likewise weak and fluxional. Kinetic studies document the sluggish reactivity of the Cu(I) complexes with molecular oxygen and rapid rates of reduction of the Cu(II) complexes by ascorbate, indicating a remarkable stability of the Cu(I) state in all three derivatives. The results show little difference between the Met ligand and its Se-Met and His congeners, and suggest that the Met contributes to catalysis in ways that are more complex than simple perturbation of the redox chemistry. Together, Chapters 3 and 4 emphasize the importance of substrate triggering of oxygen reactivity, and imply that the His_2Met ligand set, while necessary, is insufficient on its own to activate oxygen in these enzyme systems. A critical re-examination of the canonical reaction mechanisms of the mononuclear copper monooxygenases may be necessary.

6.2 Function of Cu(I)-Trp cation-π interaction in CusF

In Chapter 5 we shifted our focus to understanding the molecular basis of cuprous transport and export in the bacterial periplasmic efflux pump CusCBA and its metallochaperone CusF, which are vital to the detoxification of copper ions in the periplasm of *E. coli*. CusF has been structurally characterized and found to bind a single Cu(I) ion in a Met_2His binding environment with a unique Cu(I)–π interaction between the metal ion and W44, a nearby tryptophan. The Blackburn lab has previously used selenomethionine labeling in combination with X-ray absorption spectroscopy to show that CusF directly transfers Cu(I) ions to CusB and is required for CusCBA export of Cu(I) ions. However, the function of the Cu(I)–π interaction remains elusive, with suggestions including protection of the Cu(I) from O_2 oxidation and/or increase in selectivity for Cu(I)/Ag(I), although a role in assisting metal transfer reactivity is also possible. In order to understand the function of the tryptophan ligand (W44) we performed a mutagenesis study, described in Chapter 5, to characterize changes to structure, site accessibility, and reactivity in response to changes in the capping ligand. We also used selenomethionine labeling combined with rapid freeze quench sample preparation to compare rates of transfer between CusF and CusB. The results, monitored by FTIR show that the Cu(I)-W44 cation- π interaction in the metal binding site of CusF functions to protect the site from exogenous ligands, with the presence of the capping ligands in position 44 blocking the formation of a Cu(I)carbonyl.

Additionally, the removal the of W44 capping ligand resulted in a significantly slower rate of reduction, indicating that W44 may function to increase Cu(I) selectivity. The Cu(I)-W44 interaction may be also important for Cu(I) transfer between CusF and CusB. While this study was useful in understanding the function of the Cu(I)–π interaction, we lacked a direct probe for the ligand at position 44.

As the final part of this dissertation I have produced CusF with an unnatural amino acid incorporated at position 44 in order to add a unique spectroscopic probe for W44. Site-specific genetic incorporation of unnatural amino acids (UAAs) has been shown to be useful in providing new probes for spectroscopic studies of proteins (Berry et al., 2003; Miyake-Stoner et al., 2009). The incorporation of a UAA requires engineered plasmids expressing an orthogonal aminoacyl-tRNA synthetase (aaRS)/tRNA pair with specificity for the UAA. I have used the *M. jannaschii* TyrRS/tRNAtyr pair (Miyake-Stoner et al., 2009) to incorporate L-4-bromophenylalanine (Phe_{Br}) and L-4-cyanophenylalanine (Phe_{CN}) at position 44 of CusF. While Phe_{Br} has not been well characterized we hope to use the Br atom at the para position of the Phe_{Br} as a heavy atom for XAS, providing a direct probe for the capping ligand at position 44. On the other hand, Phe_{CN} has been used widely as a site-specific spectroscopic reporter of protein conformational changes, folding, and hydration states of proteins. Due to the sensitivity of its stretching frequency to solvation and electric field effects, the CN group of Phe_{CN} can serve as a reporter of the local environment. For example, in H_2O, Phe_{CN} has a CN band centered at 2237.2 cm^{-1} with a width of 9.8 cm^{-1}, whereas in THF this band shifts to 2228.5 cm^{-1} and concomitantly narrows its width to 5.0 cm^{-1} (Getahun et al., 2003). This shift has been attributed to the sensitivity of the CN group to hydrogen bonding (Huang et al., 2003) and local electric fields (Dalosto et al., 2004; Suydam & Boxer, 2003).

Studies from the Gai Lab (Tucker et al., 2004) have employed the CN absorbance band of Phe_{CN} to study the conformation as well as the orientation of a peptide embedded in a membrane environment. Phe_{CN} has also been shown to have unique fluorescence properties and can be selectively excited at 240 nm with an emission maximum at 290 nm; its fluorescence quantum yield depends on hydrogen bonding interactions involving the CN group (Tucker et al., 2006). The authors also showed that, like FTIR, the fluorescence of the CN group was sensitive to solvent, with the fluorescence intensity of Phe_{CN} in acetonitrile measuring about 10 times lower than in water. Studies from the Gai Lab (Getahun et al., 2003) monitored the binding of calmodulin (CaM) to a peptide derived from the CaM-binding domain of skeletal muscle myosin light chain kinase (MLCK) to determine the effect of CaM binding on Phe_{CN} fluorescence. Previous structure studies have shown that upon binding to CaM, Trp581 is sequestered into a hydrophobic pocket within the C-terminal lobe of CaM (Ikura et al., 1992). Both studies confirmed that upon binding of CaM to the peptide, the Phe_{CN} fluorescence at 290 nm significantly decreased. Additionally, the authors expected that if Phe_{CN} was substituted for Trp581, the nitrile stretching of the $\text{MLCK}_{3\text{CN}}$–CaM complex would occur at a position similar to that observed in THF. In the absence of CaM, $\text{MLCK}_{3\text{CN}}$ showed a peak at 2235.2 cm^{-1}, similar to the value of 2237.2 cm^{-1} for the free amino acid in H_2O. Upon addition of approximately 1.0 equivalent of CaM, the peak shifted to 2228.4 cm^{-1}, consistent with free amino acid in THF. Together, these results suggest that Phe_{CN} can be substituted for Trp residues and used as a probe to monitor the local environment of the amino acid using both FTIR and fluorescence. We expect the CN absorbance band to shift to a lower wave number as copper is bound to the metal binding site of CusF, resulting from the weakening of the CN bond. We also expect that copper binding should quench the observed fluorescence at 290 nm.

We have successfully produced $\text{CusF}_{\text{W44amb}}$ with a Phe_{Br} at position 44 and shown its ability to bind Cu(I) at 1:1 when compared to both protein and Br concentration. Lane 2 of the SDS-PAGE gel (Figure 6.1) shows that cell-free extract has both full-length (~10 kDa) and truncated (~4 kDa) $\text{CusF}_{\text{W44PheBr}}$ suggesting successful Phe_{Br} incorporation, as some truncated protein is expected. Lane 3 shows the expected mix of both H_6-$\text{CusF}_{\text{W44PheBr}}$ and untagged $\text{CusF}_{\text{W44PheBr}}$, produced by autocleavage. Lane 4 shows the pure full-length $\text{CusF}_{\text{W44PheBr}}$ at the expected 10 kDa.

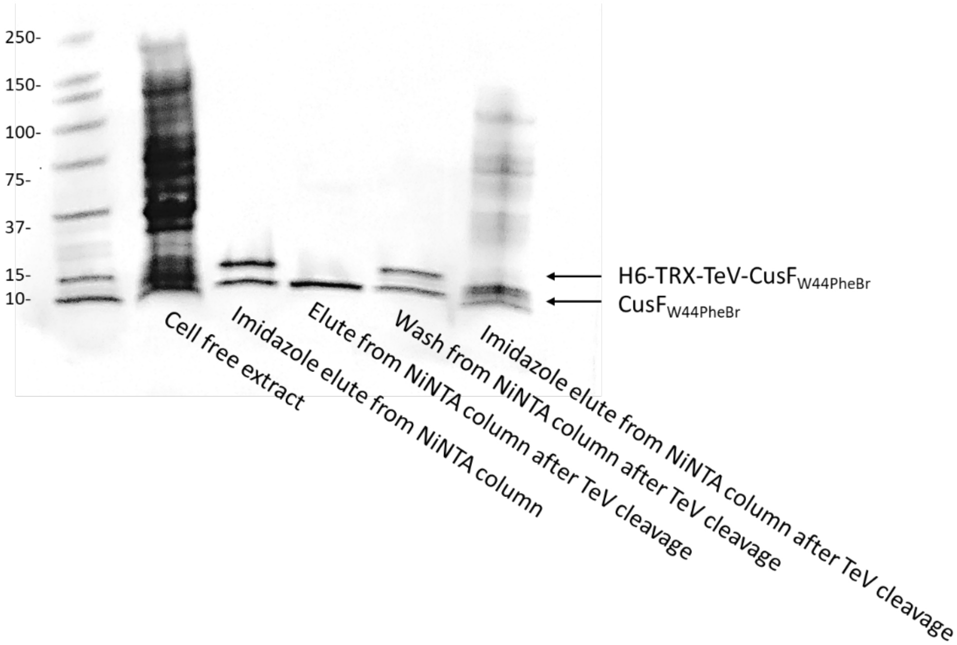

Figure 6.1 SDS-PAGE of purified CusF$_{W44PheBr}$

We then loaded CusF$_{W44BRphe}$ with Cu(I) using the protocol described in Section 5.2 and verified the Cu(I) to protein ratio using ICP-OES and BCA, respectively. The results showed the expected 1:1 Cu(I) to protein ratio. The bromine content of CusF$_{W44PheBr}$ was verified using ICP-MS, which also showed the expected 1:1 Br to protein and Br to Cu ratios (Table 6.1). We also verified the Phe$_{Br}$ incorporation via mass spectroscopy (Figure 6.2). Apo-CusF$_{WT}$ produced a single peak at the expected 9220 Da. Apo-CusF$_{W44BRphe}$ produced the expected 9619 Da. The nearly 400 Da increase can be attributed to the changes in the CusF sequence in order to add the c-terminal Strep tag and the additional Br atom.

Sample Name	Br [uM]	Cu [uM]	Protein [uM]
1. Apo-CusF$_{W44PheBr}$	70.13	---	74.2
2. Apo-CusF$_{W44PheBr}$	69.82	---	74.2
1. Cu(I)-CusF$_{W44PheBr}$	130.10	124.4	126.1
2. Cu(I)-CusF$_{W44PheBr}$	129.37	124.4	126.1

Table 6.1 Characterization of apo- and Cu(I)- loaded CusF$_{W44PheBR}$.

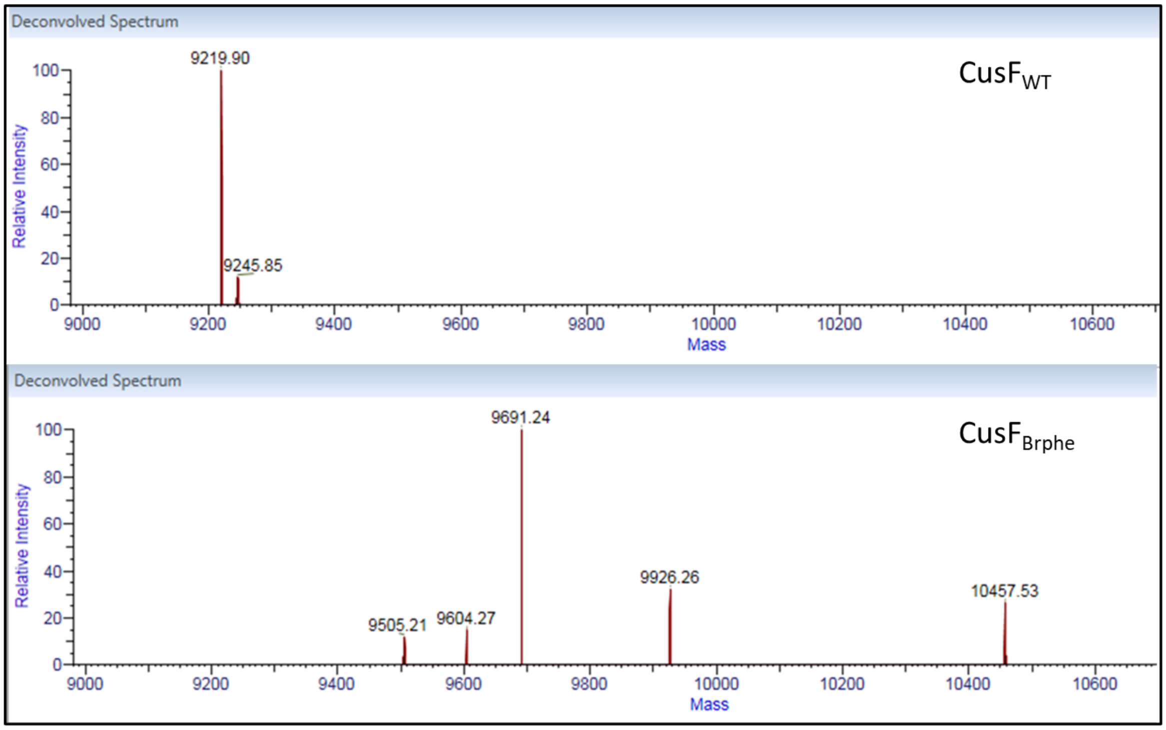

Figure 6.2 Mass spectroscopy of CusF$_{\mathrm{WT}}$ (top) and CusF$_{\mathrm{Brphe}}$ (bottom).

6.3 Future Directions

As described above, I confirmed the incorporation and metalation of CusF$_{\mathrm{W44PheBr}}$. I have also prepared apo- and Cu(I)-loaded CusF$_{\mathrm{W44PheBR}}$ XAS samples to be run at the Br and Cu K edges, to confirm the use of Phe$_{\mathrm{BR}}$ as a heavy atom for XAS. Others in the lab are also in the process of preparing CusF with Phe$_{\mathrm{CN}}$ with the hope of using CusF$_{\mathrm{W44\ PheCN}}$ in FTIR experiments, as it is IR-active and can serve as a reporter for the metal binding environment of CusF as discussed above (Miyake-Stoner et al., 2009).

Literature Cited

Aboelella, N. W., Gherman, B. F., Hill, L. M. R., York, J. T., Holm, N., Young, V. G., Cramer, C. J., & Tolman, W. B. (2006). Effects of thioether substituents on the O2 reactivity of beta-diketiminate-Cu(I) complexes: Probing the role of the methionine ligand in copper monooxygenases. *Journal of the American Chemical Society*, *128*(10), 3445–3458. https://doi.org/10.1021/ja057745v

Abriata, L. A., Banci, L., Bertini, I., Ciofi-Baffoni, S., Gkazonis, P., Spyroulias, G. A., Vila, A. J., & Wang, S. (2008). Mechanism of Cu(A) assembly. *Nature Chemical Biology*, *4*(10), 599–601. https://doi.org/10.1038/nchembio.110

Achard, M. E. S., Stafford, S. L., Bokil, N. J., Chartres, J., Bernhardt, P. V., Schembri, M. A., Sweet, M. J., & McEwan, A. G. (2012). Copper redistribution in murine macrophages in response to Salmonella infection. *The Biochemical Journal*, *444*(1), 51–57. https://doi.org/10.1042/BJ20112180

Alwan, K. B., Welch, E. F., Arias, R. J., Gambill, B. F., & Blackburn, N. J. (2019). Rational Design of a Histidine-Methionine Site Modeling the M-center of Copper Monooxygenases in a Small Metallochaperone Scaffold. *Biochemistry*, *58*(28), 3097–3108. https://doi.org/10.1021/acs.biochem.9b00312

Alwan, K. B., Welch, E. F., & Blackburn, N. J. (2019). Catalytic M Center of Copper Monooxygenases Probed by Rational Design. Effects of Selenomethionine and Histidine Substitution on Structure and Reactivity. *Biochemistry*, *58*(44), 4436–4446. https://doi.org/10.1021/acs.biochem.9b00823

Andreini, C., Banci, L., Bertini, I., & Rosato, A. (2008). Occurrence of Copper Proteins through the Three Domains of Life: A Bioinformatic Approach. *Journal of Proteome Research*, *7*(1), 209–216. https://doi.org/10.1021/pr070480u

Bagai, I., Liu, W., Rensing, C., Blackburn, N. J., & McEvoy, M. M. (2007). Substrate-linked conformational change in the periplasmic component of a Cu(I)/Ag(I) efflux system. *The Journal of Biological Chemistry*, *282*(49), 35695–35702. https://doi.org/10.1074/jbc.M703937200

Bagai, I., Rensing, C., Blackburn, N. J., & McEvoy, M. M. (2008). Direct metal transfer between periplasmic proteins identifies a bacterial copper chaperone. *Biochemistry*, *47*(44), 11408–11414. https://doi.org/10.1021/bi801638m

Banci, L., Bertini, I., Cantini, F., Felli, I. C., Gonnelli, L., Hadjiliadis, N., Pierattelli, R., Rosato, A., & Voulgaris, P. (2006). The Atx1-Ccc2 complex is a metal-mediated protein-protein interaction. *Nature Chemical Biology*, *2*(7), 367–368. https://doi.org/10.1038/nchembio797

Bauman, A. T., Broers, B. A., kline, C. D., & Blackburn, N. J. (2011). A Copper-Methionine Interaction Controls the pH-Dependent Activation of Peptidylglycine Monooxygenase. *Biochemistry*, *50*(50), 10819–10828. https://doi.org/10.1021/bi201193j

Bauman, A. T., Jaron, S., Yukl, E. T., Burchfiel, J. R., & Blackburn, N. J. (2006). pH Dependence of peptidylglycine monooxygenase. Mechanistic implications of Cu-methionine binding dynamics. *Biochemistry*, *45*(37), 11140–11150. https://doi.org/10.1021/bi060905a

Bauman, A. T., Yukl, E. T., Alkevich, K., McCormack, A. L., & Blackburn, N. J. (2006). The hydrogen peroxide reactivity of peptidylglycine monooxygenase supports a Cu(II)-superoxo catalytic intermediate. *The Journal of Biological Chemistry*, *281*(7), 4190–4198. https://doi.org/10.1074/jbc.M511199200

Berry, S. M., Ralle, M., Low, D. W., Blackburn, N. J., & Lu, Y. (2003). Probing the Role of Axial Methionine in the Blue Copper Center of Azurin with Unnatural Amino Acids. *Journal of the American Chemical Society*, *125*(29), 8760–8768. https://doi.org/10.1021/ja029699u

Bhadra, M., Lee, J. Y. C., Cowley, R. E., Kim, S., Siegler, M. A., Solomon, E. I., & Karlin, K. D. (2018). Intramolecular Hydrogen Bonding Enhances Stability and Reactivity of Mononuclear Cupric Superoxide Complexes. *Journal of the American Chemical Society*, *140*(29), 9042–9045. https://doi.org/10.1021/jacs.8b04671

Bhagi-Damodaran, A., Reed, J. H., Zhu, Q., Shi, Y., Hosseinzadeh, P., Sandoval, B. A., Harnden, K. A., Wang, S., Sponholtz, M. R., Mirts, E. N., Dwaraknath, S., Zhang, Y., Moënne-Loccoz, P., & Lu, Y. (2018). Heme redox potentials hold the key to reactivity differences between nitric oxide reductase and heme-copper oxidase. *Proceedings of the National Academy of Sciences of the United States of America*, *115*(24), 6195–6200. https://doi.org/10.1073/pnas.1720298115

Black, J. R., Champness, N. R., Levason, W., & Reid, G. (1996). Homoleptic Copper(I) and Silver(I) Complexes with o-Phenylene-Backboned Bis(thioethers), Bis(selenoethers), and Bis(telluroethers): Synthesis, Multinuclear NMR Studies, and Crystal Structures of [Cu{o-C6H4(SeMe)2}2]PF6, [Cu{o-C6H4(TeMe)2}2]PF6, and [Agn{μ-o-C6H4(SeMe)2}n{o-C6H4(SeMe)2}n][BF4]n·nCH2Cl2. *Inorganic Chemistry*, *35*(7), 1820–1824. https://doi.org/10.1021/ic951139r

Blackburn, N. J., Collison, D., Sutton, J., & Mabbs, F. E. (1984). Kinetic and e.p.r. Studies of cyanide and azide binding to the copper sites of dopamine (3,4-dihydroxyphenethylamine) beta-mono-oxygenase. *The Biochemical Journal*, *220*(2), 447–454. https://doi.org/10.1042/bj2200447

Blackburn, N. J., Hasnain, S. S., Pettingill, T. M., & Strange, R. W. (1991). Copper K-extended x-ray absorption fine structure studies of oxidized and reduced dopamine beta-hydroxylase. Confirmation of a sulfur ligand to copper(I) in the reduced enzyme. *The Journal of Biological Chemistry*, *266*(34), 23120–23127.

Blackburn, N. J., Pettingill, T. M., Seagraves, K. S., & Shigeta, R. T. (1990). Characterization of a carbon monoxide complex of reduced dopamine beta-hydroxylase. Evidence for inequivalence of the Cu(I) centers. *The Journal of Biological Chemistry*, *265*(26), 15383–15386.

Blackburn, Ninian J., Ralle, M., Gomez, E., Hill, M. G., Pastuszyn, A., Sanders, D., & Fee, J. A. (1999). Selenomethionine-Substituted Thermus thermophilus Cytochrome ba3: Characterization of the CuA Site by Se and Cu K-EXAFS. *Biochemistry*, *38*(22), 7075–7084. https://doi.org/10.1021/bi982500z

Blackburn, Ninian J., Rhames, F. C., Ralle, M., & Jaron, S. (2000). Major changes in copper coordination accompany reduction of peptidylglycine monooxygenase: Implications for electron transfer and the catalytic mechanism. *Journal of Biological Inorganic Chemistry*, *5*(3), 341–353. https://doi.org/10.1007/PL00010663

Boal, A. K., & Rosenzweig, A. C. (2009). Structural biology of copper trafficking. *Chemical Reviews*, *109*(10), 4760–4779. https://doi.org/10.1021/cr900104z

Borkow, G., & Gabbay, J. (2005). Copper as a biocidal tool. *Current Medicinal Chemistry*, *12*(18), 2163–2175. https://doi.org/10.2174/0929867054637617

Boswell, J. S., Reedy, B. J., Kulathila, R., Merkler, D., & Blackburn, N. J. (1996). Structural investigations on the coordination environment of the active- site copper centers of recombinant bifunctional peptidylglycine α-amidating enzyme. *Biochemistry*, *35*(38), 12241–12250. https://doi.org/10.1021/bi960742y

Bray, R. C. (1961). Sudden freezing as a technique for the study of rapid reactions. *Biochemical Journal*, *81*(1), 189–195.

Bruska, M. K., Stiebritz, M. T., & Reiher, M. (2015). Binding of Reactive Oxygen Species at Fe⍰S Cubane Clusters. *Chemistry – A European Journal*, *21*(52), 19081–19089. https://doi.org/10.1002/chem.201503008

Bryson, J. W., O’Halloran, T. V., Rouch, D. A., Brown, N. L., Camakaris, J., & Lee, B. T. (1993). Chemical and Genetic Studies of Copper Resistance in E. coli. *Bioinorganic Chemistry of Copper*, 101–109.

Caldararu, O., Oksanen, E., Ryde, U., & Hedegård, E. D. (2019). Mechanism of hydrogen peroxide formation by lytic polysaccharide monooxygenase. *Chemical Science*, *10*(2), 576–586. https://doi.org/10.1039/c8sc03980a

Carreira, C., Pauleta, S. R., & Moura, I. (2017). The catalytic cycle of nitrous oxide reductase—The enzyme that catalyzes the last step of denitrification. *Journal of Inorganic Biochemistry*, *177*, 423–434. https://doi.org/10.1016/j.jinorgbio.2017.09.007

Casey, A. L., Adams, D., Karpanen, T. J., Lambert, P. A., Cookson, B. D., Nightingale, P., Miruszenko, L., Shillam, R., Christian, P., & Elliott, T. S. J. (2010). Role of copper in reducing hospital environment contamination. *The Journal of Hospital Infection*, *74*(1), 72–77. https://doi.org/10.1016/j.jhin.2009.08.018

Cavet, J. S. (2014). Copper as a magic bullet for targeted microbial killing. *Chemistry & Biology*, *21*(8), 921–922. https://doi.org/10.1016/j.chembiol.2014.07.011

Cha, J. S., & Cooksey, D. A. (1991). Copper resistance in Pseudomonas syringae mediated by periplasmic and outer membrane proteins. *Proceedings of the National Academy of Sciences of the United States of America*, *88*(20), 8915–8919. https://doi.org/10.1073/pnas.88.20.8915

Chacón, K. N., & Blackburn, N. J. (2012). Stable Cu(II) and Cu(I) Mononuclear Intermediates in the Assembly of the CuA Center of Thermus thermophilus Cytochrome Oxidase. *Journal of the American Chemical Society*, *134*(39), 16401–16412. https://doi.org/10.1021/ja307276z

Chacón, K. N., Mealman, T. D., McEvoy, M. M., & Blackburn, N. J. (2014a). Tracking metal ions through a Cu/Ag efflux pump assigns the functional roles of the periplasmic proteins. *Proceedings of the National Academy of Sciences of the United States of America*, *111*(43), 15373–15378. https://doi.org/10.1073/pnas.1411475111

Chacón, K. N., Mealman, T. D., McEvoy, M. M., & Blackburn, N. J. (2014b). Tracking metal ions through a Cu/Ag efflux pump assigns the functional roles of the periplasmic proteins. *Proceedings of the National Academy of Sciences*, *111*(43), 15373–15378. https://doi.org/10.1073/pnas.1411475111

Chacón, K. N., Perkins, J., Mathe, Z., Alwan, K., Ho, E. N., Ucisik, M. N., Merz, K. M., & Blackburn, N. J. (2018). Trapping intermediates in metal transfer reactions of the CusCBAF export pump of Escherichia coli. *Communications Biology*, *1*, 192. https://doi.org/10.1038/s42003-018-0181-9

Chakraborty, S., Polen, M. J., Chacón, K. N., Wilson, T. D., Yu, Y., Reed, J., Nilges, M. J., Blackburn, N. J., & Lu, Y. (2015). Binuclear CuA Formation in Biosynthetic Models of CuA in Azurin Proceeds via a Novel Cu(Cys)2His Mononuclear Copper Intermediate. *Biochemistry*, *54*(39), 6071–6081. https://doi.org/10.1021/acs.biochem.5b00659

Chakravorty, D. K., Li, P., Tran, T. T., Bayse, C. A., & Merz, K. M. (2016). Metal Ion Capture Mechanism of a Copper Metallochaperone. *Biochemistry*, *55*(3), 501–509. https://doi.org/10.1021/acs.biochem.5b01217

Changela, A., Chen, K., Xue, Y., Holschen, J., Outten, C. E., O'Halloran, T. V., & Mondragón, A. (2003). Molecular Basis of Metal-Ion Selectivity and Zeptomolar Sensitivity by CueR. *Science*, *301*(5638), 1383–1387. https://doi.org/10.1126/science.1085950

Chaturvedi, K. S., & Henderson, J. P. (2014). Pathogenic adaptations to host-derived antibacterial copper. *Frontiers in Cellular and Infection Microbiology*, *4*. https://doi.org/10.3389/fcimb.2014.00003

Chauhan, S., Hosseinzadeh, P., Lu, Y., & Blackburn, N. J. (2016). Stopped-Flow Studies of the Reduction of the Copper Centers Suggest a Bifurcated Electron Transfer Pathway in Peptidylglycine Monooxygenase. *Biochemistry*, *55*(13), 2008–2021. https://doi.org/10.1021/acs.biochem.6b00061

Chauhan, S., Kline, C. D., Mayfield, M., & Blackburn, N. J. (2014). Binding of Copper and Silver to Single-Site Variants of Peptidylglycine Monooxygenase Reveals the Structure and Chemistry of the Individual Metal Centers. *Biochemistry*, *53*(6), 1069–1080. https://doi.org/10.1021/bi4015264

Chen, K., Yuldasheva, S., Penner-Hahn, J. E., & O'Halloran, T. V. (2003). An Atypical Linear Cu(I)−S2 Center Constitutes the High-Affinity Metal-Sensing Site in the CueR Metalloregulatory Protein. *Journal of the American Chemical Society*, *125*(40), 12088–12089. https://doi.org/10.1021/ja036070y

Chen, P., Bell, J., Eipper, B. A., & Solomon, E. I. (2004). Oxygen activation by the noncoupled binuclear copper site in peptidylglycine alpha-hydroxylating monooxygenase. Spectroscopic definition of the resting sites and the putative CuIIM-OOH intermediate. *Biochemistry*, *43*(19), 5735–5747. https://doi.org/10.1021/bi0362830

Chen, P., Root, D. E., Campochiaro, C., Fujisawa, K., & Solomon, E. I. (2003). Spectroscopic and Electronic Structure Studies of the Diamagnetic Side-On CuII-Superoxo Complex Cu(O2)[HB(3-R-5-iPrpz)3]: Antiferromagnetic Coupling versus Covalent Delocalization. *Journal of the American Chemical Society*, *125*(2), 466–474. https://doi.org/10.1021/ja020969i

Chen, P., & Solomon, E. I. (2004). O2 activation by binuclear Cu sites: Noncoupled versus exchange coupled reaction mechanisms. *Proceedings of the National Academy of Sciences*, *101*(36), 13105–13110. https://doi.org/10.1073/pnas.0402114101

Chufán, E. E., De, M., Eipper, B. A., Mains, R. E., & Amzel, L. M. (2009). Amidation of Bioactive Peptides: The Structure of the Lyase Domain of the Amidating Enzyme. *Structure*, *17*(7), 965–973. https://doi.org/10.1016/j.str.2009.05.008

Chufán, E. E., Prigge, S. T., Siebert, X., Eipper, B. A., Mains, R. E., & Amzel, L. M. (2010). Differential reactivity between two copper sites in peptidylglycine α-hydroxylating monooxygenase. *Journal of the American Chemical Society*, *132*(44), 15565–15572. https://doi.org/10.1021/ja103117r

Clark, K. M., Yu, Y., Marshall, N. M., Sieracki, N. A., Nilges, M. J., Blackburn, N. J., van der Donk, W., & Lu, Y. (2010). Transforming a Blue Copper into a Red Copper Protein: Engineering Cysteine and Homocysteine into the Axial Position of Azurin using Site-Directed Mutagenesis and Expressed Protein Ligation. *Journal of the American Chemical Society*, *132*(29), 10093–10101. https://doi.org/10.1021/ja102632p

Cowley, R. E., Tian, L., & Solomon, E. I. (2016). Mechanism of O2 activation and substrate hydroxylation in noncoupled binuclear copper monooxygenases. *Proceedings of the National Academy of Sciences of the United States of America*, *113*(43), 12035–12040. https://doi.org/10.1073/pnas.1614807113

Crespo, A., Martí, M. A., Roitberg, A. E., Amzel, L. M., & Estrin, D. A. (2006). The catalytic mechanism of peptidylglycine alpha-hydroxylating monooxygenase investigated by computer simulation. *Journal of the American Chemical Society*, *128*(39), 12817–12828. https://doi.org/10.1021/ja062876x

Dalosto, S. D., Vanderkooi, J. M., & Sharp, K. A. (2004). Vibrational Stark Effects on Carbonyl, Nitrile, and Nitrosyl Compounds Including Heme Ligands, CO, CN, and NO, Studied with Density Functional Theory. *The Journal of Physical Chemistry B*, *108*(20), 6450–6457. https://doi.org/10.1021/jp0310697

Davis, A. V., & O'Halloran, T. V. (2008). A place for thioether chemistry in cellular copper ion recognition and trafficking. *Nature Chemical Biology*, *4*(3), 148–151. https://doi.org/10.1038/nchembio0308-148

De Feo, C. J., Aller, S. G., Siluvai, G. S., Blackburn, N. J., & Unger, V. M. (2009). Three-dimensional structure of the human copper transporter hCTR1. *Proceedings of the National Academy of Sciences of the United States of America*, *106*(11), 4237–4242. https://doi.org/10.1073/pnas.0810286106

DeGrado, W. F., Summa, C. M., Pavone, V., Nastri, F., & Lombardi, A. (1999). De novo design and structural characterization of proteins and metalloproteins. *Annual Review of Biochemistry*, *68*, 779–819. https://doi.org/10.1146/annurev.biochem.68.1.779

Dieckmann, G. R., McRorie, D. K., Lear, J. D., Sharp, K. A., DeGrado, W. F., & Pecoraro, V. L. (1998). The role of protonation and metal chelation preferences in defining the properties of mercury-binding coiled coils. *Journal of Molecular Biology*, *280*(5), 897–912. https://doi.org/10.1006/jmbi.1998.1891

Ding, C., Festa, R. A., Chen, Y.-L., Espart, A., Palacios, Ò., Espín, J., Capdevila, M., Atrian, S., Heitman, J., & Thiele, D. J. (2013). Cryptococcus neoformans copper detoxification machinery is critical for fungal virulence. *Cell Host & Microbe*, *13*(3), 265–276. https://doi.org/10.1016/j.chom.2013.02.002

Djoko, K. Y., Xiao, Z., Huffman, D. L., & Wedd, A. G. (2007). Conserved Mechanism of Copper Binding and Transfer. A Comparison of the Copper-Resistance Proteins PcoC from Escherichia coli and CopC from Pseudomonas syringae. *Inorganic Chemistry*, *46*(11), 4560–4568. https://doi.org/10.1021/ic070107o

Dollwet, H., and Sorenson, J. R. J. (1985). Historic uses of copper compounds in medicine. *Trace Elem. Med.*, *2*, 80–88.

Dooley, D. M., & Golnik, K. C. (1983). Spectroscopic and kinetics studies of the inhibition of pig kidney diamine oxidase by anions. *The Journal of Biological Chemistry*, *258*(7), 4245–4248.

Douglas, L. M., Wang, H. X., Keppler-Ross, S., Dean, N., & Konopka, J. B. (2012). Sur7 Promotes Plasma Membrane Organization and Is Needed for Resistance to Stressful Conditions and to the Invasive Growth and Virulence of Candida albicans. *MBio*, *3*(1). https://doi.org/10.1128/mBio.00254-11

Dupont, C. L., Grass, G., & Rensing, C. (2011). Copper toxicity and the origin of bacterial resistance—New insights and applications. *Metallomics*, *3*(11), 1109–1118. https://doi.org/10.1039/C1MT00107H

Eipper, B. A., Quon, A. S., Mains, R. E., Boswell, J. S., & Blackburn, N. J. (1995). The catalytic core of peptidylglycine alpha-hydroxylating monooxygenase: Investigation by site-directed mutagenesis, Cu X-ray absorption spectroscopy, and electron paramagnetic resonance. *Biochemistry*, *34*(9), 2857–2865. https://doi.org/10.1021/bi00009a016

Elwell, C. E., Gagnon, N. L., Neisen, B. D., Dhar, D., Spaeth, A. D., Yee, G. M., & Tolman, W. B. (2017). Copper-Oxygen Complexes Revisited: Structures, Spectroscopy, and Reactivity. *Chemical Reviews*, *117*(3), 2059–2107. https://doi.org/10.1021/acs.chemrev.6b00636

Evans, J. P., Ahn, K., & Klinman, J. P. (2003). Evidence that dioxygen and substrate activation are tightly coupled in dopamine beta-monooxygenase. Implications for the reactive oxygen species. *The Journal of Biological Chemistry*, *278*(50), 49691–49698. https://doi.org/10.1074/jbc.M300797200

Evans, J. P., Blackburn, N. J., & Klinman, J. P. (2006). The catalytic role of the copper ligand H172 of peptidylglycine alpha-hydroxylating monooxygenase: A kinetic study of the H172A mutant. *Biochemistry*, *45*(51), 15419–15429. https://doi.org/10.1021/bi061734c

Fager, L. Y., & Alben, J. O. (1972). Structure of the carbon monoxide binding site of hemocyanins studied by Fourier transform infrared spectroscopy. *Biochemistry*, *11*(25), 4786–4792. https://doi.org/10.1021/bi00775a023

Fan, B., & Rosen, B. P. (2002). Biochemical Characterization of CopA, the Escherichia coli Cu(I)-translocating P-type ATPase. *Journal of Biological Chemistry*, *277*(49), 46987–46992. https://doi.org/10.1074/jbc.M208490200

Fee, J. A., & Gaber, B. P. (1972). Anion binding to bovine erythrocyte superoxide dismutase. Evidence for multiple binding sites with qualitatively different properties. *The Journal of Biological Chemistry*, *247*(1), 60–65.

Ferguson-Miller, S., & Babcock, G. T. (1996). Heme/Copper Terminal Oxidases. *Chemical Reviews*, *96*(7), 2889–2908. https://doi.org/10.1021/cr950051s

Festa, R. A., Helsel, M. E., Franz, K. J., & Thiele, D. J. (2014). Exploiting innate immune cell activation of a copper-dependent antimicrobial agent during infection. *Chemistry & Biology*, *21*(8), 977–987. https://doi.org/10.1016/j.chembiol.2014.06.009

Finazzi-Agro, A., Zolla, L., Flamigni, L., Kuiper, H. A., & Brunori, M. (1982). Spectroscopy of carbon monoxide-hemocyanins. Phosphorescence of the binuclear carbonylated copper centers. *Biochemistry*, *21*(2), 415–418. https://doi.org/10.1021/bi00531a032

Finney, L. A., & O'Halloran, T. V. (2003). Transition metal speciation in the cell: Insights from the chemistry of metal ion receptors. *Science (New York, N.Y.)*, *300*(5621), 931–936. https://doi.org/10.1126/science.1085049

Fisher, O. S., Kenney, G. E., Ross, M. O., Ro, S. Y., Lemma, B. E., Batelu, S., Thomas, P. M., Sosnowski, V. C., DeHart, C. J., Kelleher, N. L., Stemmler, T. L., Hoffman, B. M., & Rosenzweig, A. C. (2018). Characterization of a long overlooked copper protein from methane- and ammonia-oxidizing bacteria. *Nature Communications*, *9*(1), 4276. https://doi.org/10.1038/s41467-018-06681-5

Francisco, W. A., Merkler, D. J., Blackburn, N. J., & Klinman, J. P. (1998). Kinetic mechanism and intrinsic isotope effects for the peptidylglycine alpha-amidating enzyme reaction. *Biochemistry*, *37*(22), 8244–8252. https://doi.org/10.1021/bi973004y

Francisco, Wilson A., Knapp, M. J., Blackburn, N. J., & Klinman, J. P. (2002). Hydrogen tunneling in peptidylglycine alpha-hydroxylating monooxygenase. *Journal of the American Chemical Society*, *124*(28), 8194–8195. https://doi.org/10.1021/ja025758s

Franke, S., Grass, G., & Nies, D. H. (2001). The product of the ybdE gene of the Escherichia coli chromosome is involved in detoxification of silver ions. *Microbiology (Reading, England)*, *147*(Pt 4), 965–972. https://doi.org/10.1099/00221287-147-4-965

Franke, S., Grass, G., Rensing, C., & Nies, D. H. (2003). Molecular Analysis of the Copper-Transporting Efflux System CusCFBA of Escherichia coli. *Journal of Bacteriology*, *185*(13), 3804–3812. https://doi.org/10.1128/JB.185.13.3804-3812.2003

Fu, Y., Chang, F.-M. J., & Giedroc, D. P. (2014). Copper Transport and Trafficking at the Host–Bacterial Pathogen Interface. *Accounts of Chemical Research*, *47*(12), 3605–3613. https://doi.org/10.1021/ar500300n

Fujisawa, K., Tanaka, M., Moro-oka, Y., & Kitajima, N. (1994). A Monomeric Side-On Superoxocopper(II) Complex: Cu(O2)(HB(3-tBu-5-iPrpz)3). *Journal of the American Chemical Society*, *116*(26), 12079–12080. https://doi.org/10.1021/ja00105a069

George, G. N., Bray, R. C., & Cramer, S. P. (1986). Extended X-ray absorption fine structure studies of transient species during xanthine oxidase turnover by using rapid freezing. *Biochemical Society Transactions*, *14*(3), 651–652. https://doi.org/10.1042/bst0140651

Getahun, Z., Huang, C.-Y., Wang, T., De León, B., DeGrado, W. F., & Gai, F. (2003). Using Nitrile-Derivatized Amino Acids as Infrared Probes of Local Environment. *Journal of the American Chemical Society*, *125*(2), 405–411. https://doi.org/10.1021/ja0285262

Ginsbach, J. W., Peterson, R. L., Cowley, R. E., Karlin, K. D., & Solomon, E. I. (2013). Correlation of the electronic and geometric structures in mononuclear copper(II) superoxide complexes. *Inorganic Chemistry*, *52*(22), 12872–12874. https://doi.org/10.1021/ic402357u

Gourdon, P., Liu, X.-Y., Skjørringe, T., Morth, J. P., Møller, L. B., Pedersen, B. P., & Nissen, P. (2011a). Crystal structure of a copper-transporting PIB-type ATPase. *Nature*, *475*(7354), 59–64. https://doi.org/10.1038/nature10191

Gourdon, P., Liu, X.-Y., Skjørringe, T., Morth, J. P., Møller, L. B., Pedersen, B. P., & Nissen, P. (2011b). Crystal structure of a copper-transporting PIB-type ATPase. *Nature*, *475*(7354), 59–64. https://doi.org/10.1038/nature10191

Grass, G., & Rensing, C. (2001). CueO is a multi-copper oxidase that confers copper tolerance in Escherichia coli. *Biochemical and Biophysical Research Communications*, *286*(5), 902–908. https://doi.org/10.1006/bbrc.2001.5474

Grass, Gregor, Rensing, C., & Solioz, M. (2011). Metallic copper as an antimicrobial surface. *Applied and Environmental Microbiology*, *77*(5), 1541–1547. https://doi.org/10.1128/AEM.02766-10

Halliwell, B., & Gutteridge, J. M. (1984). Oxygen toxicity, oxygen radicals, transition metals and disease. *Biochemical Journal*, *219*(1), 1–14.

Hangasky, J. A., Taabazuing, C. Y., Martin, C. B., Eron, S. J., & Knapp, M. J. (2017). The facial triad in the α-ketoglutarate dependent oxygenase FIH: A role for sterics in linking substrate binding to O2 activation. *Journal of Inorganic Biochemistry*, *166*, 26–33. https://doi.org/10.1016/j.jinorgbio.2016.10.007

Hay, M., Richards, J. H., & Lu, Y. (1996). Construction and characterization of an azurin analog for the purple copper site in cytochrome c oxidase. *Proceedings of the National Academy of Sciences*, *93*(1), 461–464. https://doi.org/10.1073/pnas.93.1.461

Hess, C. R., Klinman, J. P., & Blackburn, N. J. (2010). The copper centers of tyramine β-monooxygenase and its catalytic-site methionine variants: An X-ray absorption study. *Journal of Biological Inorganic Chemistry: JBIC: A Publication of the Society of Biological Inorganic Chemistry*, *15*(8), 1195–1207. https://doi.org/10.1007/s00775-010-0677-3

Hess, C. R., McGuirl, M. M., & Klinman, J. P. (2008). Mechanism of the insect enzyme, tyramine beta-monooxygenase, reveals differences from the mammalian enzyme, dopamine beta-monooxygenase. *The Journal of Biological Chemistry*, *283*(6), 3042–3049. https://doi.org/10.1074/jbc.M705911200

Hess, C. R., Wu, Z., Ng, A., Gray, E. E., McGuirl, M. A., & Klinman, J. P. (2008). Hydroxylase activity of Met471Cys tyramine beta-monooxygenase. *Journal of the American Chemical Society*, *130*(36), 11939–11944. https://doi.org/10.1021/ja800408h

Hong, R., Kang, T. Y., Michels, C. A., & Gadura, N. (2012). Membrane lipid peroxidation in copper alloy-mediated contact killing of Escherichia coli. *Applied and Environmental Microbiology*, *78*(6), 1776–1784. https://doi.org/10.1128/AEM.07068-11

Hosseinzadeh, P., Marshall, N. M., Chacón, K. N., Yu, Y., Nilges, M. J., New, S. Y., Tashkov, S. A., Blackburn, N. J., & Lu, Y. (2016). Design of a single protein that spans the entire 2-V range of physiological redox potentials. *Proceedings of the National Academy of Sciences of the United States of America*, *113*(2), 262–267. https://doi.org/10.1073/pnas.1515897112

Huang, C.-Y., Wang, T., & Gai, F. (2003). Temperature dependence of the CN stretching vibration of a nitrile-derivatized phenylalanine in water. *Chemical Physics Letters*, *371*(5), 731–738. https://doi.org/10.1016/S0009-2614(03)00353-1

Huffman, D. L., & O’Halloran, T. V. (2000). Energetics of copper trafficking between the Atx1 metallochaperone and the intracellular copper transporter, Ccc2. *The Journal of Biological Chemistry*, *275*(25), 18611–18614. https://doi.org/10.1074/jbc.C000172200

I, B. (1998, May). *Manifestations of copper excess*. The American Journal of Clinical Nutrition; Am J Clin Nutr. https://doi.org/10.1093/ajcn/67.5.1069S

Ikura, M., Barbato, G., Klee, C. B., & Bax, A. (1992). Solution structure of calmodulin and its complex with a myosin light chain kinase fragment. *Cell Calcium*, *13*(6–7), 391–400. https://doi.org/10.1016/0143-4160(92)90052-t

Imlay, J. A. (2014). The Mismetallation of Enzymes during Oxidative Stress. *Journal of Biological Chemistry*, *289*(41), 28121–28128. https://doi.org/10.1074/jbc.R114.588814

Irving, H., & Williams, R. J. P. (1953). 637. The stability of transition-metal complexes. *Journal of the Chemical Society (Resumed)*, *0*, 3192–3210. https://doi.org/10.1039/JR9530003192

Itoh, S. (2015). Developing Mononuclear Copper–Active-Oxygen Complexes Relevant to Reactive Intermediates of Biological Oxidation Reactions. *Accounts of Chemical Research*, *48*(7), 2066–2074. https://doi.org/10.1021/acs.accounts.5b00140

Jaron, S., & Blackburn, N. J. (1999). Does superoxide channel between the copper centers in peptidylglycine monooxygenase? A new mechanism based on carbon monoxide reactivity. *Biochemistry*, *38*(46), 15086–15096. https://doi.org/10.1021/bi991341w

Jaron, S., & Blackburn, N. J. (2001). Characterization of a half-apo derivative of peptidylglycine monooxygenase. Insight into the reactivity of each active site copper. *Biochemistry*, *40*(23), 6867–6875. https://doi.org/10.1021/bi002849y

Jiang, J., Nadas, I. A., Kim, M. A., & Franz, K. J. (2005). A Mets motif peptide found in copper transport proteins selectively binds Cu(I) with methionine-only coordination. *Inorganic Chemistry*, *44*(26), 9787–9794. https://doi.org/10.1021/ic051180m

Kadiiska, M. B., & Mason, R. P. (2002). In vivo copper-mediated free radical production: An ESR spin-trapping study. *Spectrochimica Acta. Part A, Molecular and Biomolecular Spectroscopy*, *58*(6), 1227–1239. https://doi.org/10.1016/s1386-1425(01)00713-2

Kazuo Nakamoto. (2008). *Infrared and Raman Spectra of Inorganic and Coordination Compounds. Hand book of vibrational spetroscopy.* John Wiley & Sons, Inc.

Kertess, L., Wittkamp, F., Sommer, C., Esselborn, J., Rüdiger, O., Reijerse, E. J., Hofmann, E., Lubitz, W., Winkler, M., Happe, T., & Apfel, U.-P. (2017). Chalcogenide substitution in the [2Fe] cluster of [FeFe]-hydrogenases conserves high enzymatic activity. *Dalton Transactions (Cambridge, England: 2003)*, *46*(48), 16947–16958. https://doi.org/10.1039/c7dt03785f

Keyer, K., & Imlay, J. A. (1996). Superoxide accelerates DNA damage by elevating free-iron levels. *Proceedings of the National Academy of Sciences of the United States of America*, *93*(24), 13635–13640.

Kim, B.-E., Nevitt, T., & Thiele, D. J. (2008). Mechanisms for copper acquisition, distribution and regulation. *Nature Chemical Biology*, *4*(3), 176–185. https://doi.org/10.1038/nchembio.72

Kim, E.-H., Nies, D. H., McEvoy, M. M., & Rensing, C. (2011). Switch or Funnel: How RND-Type Transport Systems Control Periplasmic Metal Homeostasis ▿. *Journal of Bacteriology*, *193*(10), 2381–2387. https://doi.org/10.1128/JB.01323-10

Kim, S., Lee, J. Y., Cowley, R. E., Ginsbach, J. W., Siegler, M. A., Solomon, E. I., & Karlin, K. D. (2015). A N3S(thioether)-ligated Cu(II)-superoxo with enhanced reactivity. *Journal of the American Chemical Society*, *137*(8), 2796–2799. https://doi.org/10.1021/ja511504n

Kittleson, J. T., Loftin, I. R., Hausrath, A. C., Engelhardt, K. P., Rensing, C., & McEvoy, M. M. (2006). Periplasmic metal-resistance protein CusF exhibits high affinity and specificity for both CuI and AgI. *Biochemistry*, *45*(37), 11096–11102. https://doi.org/10.1021/bi0612622

Kjaergaard, C. H., Qayyum, M. F., Wong, S. D., Xu, F., Hemsworth, G. R., Walton, D. J., Young, N. A., Davies, G. J., Walton, P. H., Johansen, K. S., Hodgson, K. O., Hedman, B., & Solomon, E. I. (2014). Spectroscopic and computational insight into the activation of O2 by the mononuclear Cu center in polysaccharide monooxygenases. *Proceedings of the National Academy of Sciences of the United States of America*, *111*(24), 8797–8802. https://doi.org/10.1073/pnas.1408115111

Kline, C. D., & Blackburn, N. J. (2016). Substrate-Induced Carbon Monoxide Reactivity Suggests Multiple Enzyme Conformations at the Catalytic Copper M-Center of Peptidylglycine Monooxygenase. *Biochemistry*, *55*(48), 6652–6661. https://doi.org/10.1021/acs.biochem.6b00845

Kline, C. D., Mayfield, M., & Blackburn, N. J. (2013). HHM Motif at the CuH-Site of Peptidylglycine Monooxygenase is a pH-Dependent Conformational Switch. *Biochemistry*, *52*(15), 2586–2596. https://doi.org/10.1021/bi4002248

Klinman, J. P. (1996). Mechanisms Whereby Mononuclear Copper Proteins Functionalize Organic Substrates. *Chemical Reviews*, *96*(7), 2541–2562. https://doi.org/10.1021/cr950047g

Klinman, J. P. (2006a). The copper-enzyme family of dopamine beta-monooxygenase and peptidylglycine alpha-hydroxylating monooxygenase: Resolving the chemical pathway for substrate hydroxylation. *The Journal of Biological Chemistry*, *281*(6), 3013–3016. https://doi.org/10.1074/jbc.R500011200

Klinman, J. P. (2006b). The copper-enzyme family of dopamine beta-monooxygenase and peptidylglycine alpha-hydroxylating monooxygenase: Resolving the chemical pathway for substrate hydroxylation. *The Journal of Biological Chemistry*, *281*(6), 3013–3016. https://doi.org/10.1074/jbc.R500011200

Koebke, K. J., & Pecoraro, V. L. (2018). Development of de Novo Copper Nitrite Reductases: Where We Are and Where We Need To Go. *ACS Catalysis*, *8*(9), 8046–8057. https://doi.org/10.1021/acscatal.8b02153

Kolhekar, A. S., Keutmann, H. T., Mains, R. E., Quon, A. S., & Eipper, B. A. (1997). Peptidylglycine alpha-hydroxylating monooxygenase: Active site residues, disulfide linkages, and a two-domain model of the catalytic core. *Biochemistry*, *36*(36), 10901–10909. https://doi.org/10.1021/bi9708747

Kroneck, P. M. H. (2018). Walking the seven lines: Binuclear copper A in cytochrome c oxidase and nitrous oxide reductase. *Journal of Biological Inorganic Chemistry: JBIC: A Publication of the Society of Biological Inorganic Chemistry*, *23*(1), 27–39. https://doi.org/10.1007/s00775-017-1510-z

Kuchenreuther, J. M., George, S. J., Grady-Smith, C. S., Cramer, S. P., & Swartz, J. R. (2011). Cell-free H-cluster Synthesis and [FeFe] Hydrogenase Activation: All Five CO and CN− Ligands Derive from Tyrosine. *PLoS ONE*, *6*(5). https://doi.org/10.1371/journal.pone.0020346

Kulathila, R., Kulathila, R., Indic, M., & Berg, B. van den. (2011). Crystal Structure of Escherichia coli CusC, the Outer Membrane Component of a Heavy Metal Efflux Pump. *PLOS ONE*, *6*(1), e15610. https://doi.org/10.1371/journal.pone.0015610

Kumar, D., Mains, R. E., & Eipper, B. A. (2016). 60 YEARS OF POMC: From POMC and α-MSH to PAM, molecular oxygen, copper, and vitamin C. *Journal of Molecular Endocrinology*, *56*(4), T63-76. https://doi.org/10.1530/JME-15-0266

Kunishita, A., Ertem, M. Z., Okubo, Y., Tano, T., Sugimoto, H., Ohkubo, K., Fujieda, N., Fukuzumi, S., Cramer, C. J., & Itoh, S. (2012). Active site models for the Cu(A) site of peptidylglycine α-hydroxylating monooxygenase and dopamine β-monooxygenase. *Inorganic Chemistry*, *51*(17), 9465–9480. https://doi.org/10.1021/ic301272h

Kunishita, A., Kubo, M., Sugimoto, H., Ogura, T., Sato, K., Takui, T., & Itoh, S. (2009). Mononuclear copper(II)-superoxo complexes that mimic the structure and reactivity of the active centers of PHM and DbetaM. *Journal of the American Chemical Society*, *131*(8), 2788–2789. https://doi.org/10.1021/ja809464e

Kuzmic, P. (1996). Program DYNAFIT for the analysis of enzyme kinetic data: Application to HIV proteinase. *Analytical Biochemistry*, *237*(2), 260–273. https://doi.org/10.1006/abio.1996.0238

Lanci, M. P., Smirnov, V. V., Cramer, C. J., Gauchenova, E. V., Sundermeyer, J., & Roth, J. P. (2007). Isotopic probing of molecular oxygen activation at copper(I) sites. *Journal of the American Chemical Society*, *129*(47), 14697–14709. https://doi.org/10.1021/ja074620c

Lee, D.-H., Hatcher, L. Q., Vance, M. A., Sarangi, R., Milligan, A. E., Sarjeant, A. A. N., Incarvito, C. D., Rheingold, A. L., Hodgson, K. O., Hedman, B., Solomon, E. I., & Karlin, K. D. (2007). Copper(I) complex O(2)-reactivity with a N(3)S thioether ligand: A copper-dioxygen adduct including sulfur ligation, ligand oxygenation, and comparisons with all nitrogen ligand analogues. *Inorganic Chemistry*, *46*(15), 6056–6068. https://doi.org/10.1021/ic700541k

Lee, J. Y., & Karlin, K. D. (2015). Elaboration of copper-oxygen mediated C-H activation chemistry in consideration of future fuel and feedstock generation. *Current Opinion in Chemical Biology*, *25*, 184–193. https://doi.org/10.1016/j.cbpa.2015.02.014

Leisle, L., Valiyaveetil, F., Mehl, R. A., & Ahern, C. A. (2015). Incorporation of Non-Canonical Amino Acids. *Advances in Experimental Medicine and Biology*, *869*, 119–151. https://doi.org/10.1007/978-1-4939-2845-3_7

Li, C., Oldham, C. D., & May, S. W. (1994). NN-dimethyl-1,4-phenylenediamine as an alternative reductant for peptidylglycine alpha-amidating mono-oxygenase catalysis. *The Biochemical Journal*, *300 (Pt 1)*, 31–36. https://doi.org/10.1042/bj3000031

Liu, J., Chakraborty, S., Hosseinzadeh, P., Yu, Y., Tian, S., Petrik, I., Bhagi, A., & Lu, Y. (2014). Metalloproteins Containing Cytochrome, Iron–Sulfur, or Copper Redox Centers. *Chemical Reviews*, *114*(8), 4366–4469. https://doi.org/10.1021/cr400479b

Loftin, I. R., Blackburn, N. J., & McEvoy, M. M. (2009). Tryptophan Cu(I)-pi interaction fine-tunes the metal binding properties of the bacterial metallochaperone CusF. *Journal of Biological Inorganic Chemistry: JBIC: A Publication of the Society of Biological Inorganic Chemistry*, *14*(6), 905–912. https://doi.org/10.1007/s00775-009-0503-y

Loftin, I. R., Franke, S., Blackburn, N. J., & McEvoy, M. M. (2007). Unusual Cu(I)/Ag(I) coordination of Escherichia coli CusF as revealed by atomic resolution crystallography and X-ray absorption spectroscopy. *Protein Science : A Publication of the Protein Society*, *16*(10), 2287–2293. https://doi.org/10.1110/ps.073021307

Long, F., Su, C.-C., Zimmermann, M. T., Boyken, S. E., Rajashankar, K. R., Jernigan, R. L., & Yu, E. W. (2010). Crystal structures of the CusA efflux pump suggest methionine-mediated metal transport. *Nature*, *467*(7314), 484–488. https://doi.org/10.1038/nature09395

Lu, Y., Berry, S. M., & Pfister, T. D. (2001). Engineering Novel Metalloproteins: Design of Metal-Binding Sites into Native Protein Scaffolds. *Chemical Reviews*, *101*(10), 3047–3080. https://doi.org/10.1021/cr0000574

Lucas, H. R., & Karlin, K. D. (2009). Copper-Carbon Bonds in Mechanistic and Structural Probing of Proteins as well as in Situations where Copper is a Catalytic or Receptor Site. *Metal Ions in Life Sciences*, *6*, 295–361. https://doi.org/10.1039/BK9781847559159-00295

Macomber, L., & Imlay, J. A. (2009). The iron-sulfur clusters of dehydratases are primary intracellular targets of copper toxicity. *Proceedings of the National Academy of Sciences*, *106*(20), 8344–8349. https://doi.org/10.1073/pnas.0812808106

Maheshwari, S., Shimokawa, C., Rudzka, K., Kline, C. D., Eipper, B. A., Mains, R. E., Gabelli, S. B., Blackburn, N., & Amzel, L. M. (2018). Effects of copper occupancy on the conformational landscape of peptidylglycine α-hydroxylating monooxygenase. *Communications Biology*, *1*, 74. https://doi.org/10.1038/s42003-018-0082-y

Maiti, D., Fry, H. C., Woertink, J. S., Vance, M. A., Solomon, E. I., & Karlin, K. D. (2007). A 1:1 copper-dioxygen adduct is an end-on bound superoxo copper(II) complex which undergoes oxygenation reactions with phenols. *Journal of the American Chemical Society*, *129*(2), 264–265. https://doi.org/10.1021/ja067411l

Mann, S. I., Heinisch, T., Ward, T. R., & Borovik, A. S. (2017). Peroxide Activation Regulated by Hydrogen Bonds within Artificial Cu Proteins. *Journal of the American Chemical Society*, *139*(48), 17289–17292. https://doi.org/10.1021/jacs.7b10452

Mann, S. I., Heinisch, T., Ward, T. R., & Borovik, A. S. (2018). Coordination chemistry within a protein host: Regulation of the secondary coordination sphere. *Chemical Communications (Cambridge, England)*, *54*(35), 4413–4416. https://doi.org/10.1039/c8cc01931b

Mann, S. I., Heinisch, T., Weitz, A. C., Hendrich, M. P., Ward, T. R., & Borovik, A. S. (2016). Modular Artificial Cupredoxins. *Journal of the American Chemical Society*, *138*(29), 9073–9076. https://doi.org/10.1021/jacs.6b05428

Matsumura, H., Hayashi, T., Chakraborty, S., Lu, Y., & Moënne-Loccoz, P. (2014). The Production of Nitrous Oxide by the Heme/Nonheme Diiron Center of Engineered Myoglobins (Fe $_B$ Mbs) Proceeds through a *trans* -Iron-Nitrosyl Dimer. *Journal of the American Chemical Society*, *136*(6), 2420–2431. https://doi.org/10.1021/ja410542z

Mattle, D., Zhang, L., Sitsel, O., Pedersen, L. T., Moncelli, M. R., Tadini-Buoninsegni, F., Gourdon, P., Rees, D. C., Nissen, P., & Meloni, G. (2015). A sulfur-based transport pathway in Cu+-ATPases. *EMBO Reports*, *16*(6), 728–740. https://doi.org/10.15252/embr.201439927

Mealman, T. D., Blackburn, N. J., & McEvoy, M. M. (2012). Metal export by CusCFBA, the periplasmic Cu(I)/Ag(I) transport system of Escherichia coli. *Current Topics in Membranes*, *69*, 163–196. https://doi.org/10.1016/B978-0-12-394390-3.00007-0

Mealman, T. D., Zhou, M., Affandi, T., Chacón, K. N., Aranguren, M. E., Blackburn, N. J., Wysocki, V. H., & McEvoy, M. M. (2012). N-Terminal Region of CusB Is Sufficient for Metal Binding and Metal Transfer with the Metallochaperone CusF. *Biochemistry*, *51*(34), 6767–6775. https://doi.org/10.1021/bi300596a

Mercer, J. F. (2001). The molecular basis of copper-transport diseases. *Trends in Molecular Medicine*, *7*(2), 64–69. https://doi.org/10.1016/s1471-4914(01)01920-7

Miarzlou, D. A., Leisinger, F., Joss, D., Häussinger, D., & Seebeck, F. P. (2019). Structure of formylglycine-generating enzyme in complex with copper and a substrate reveals an acidic pocket for binding and activation of molecular oxygen. *Chemical Science*, *10*(29), 7049–7058. https://doi.org/10.1039/c9sc01723b

Michels, H. T., Keevil, C. W., Salgado, C. D., & Schmidt, M. G. (2015). From Laboratory Research to a Clinical Trial: Copper Alloy Surfaces Kill Bacteria and Reduce Hospital-Acquired Infections. *HERD*, *9*(1), 64–79. https://doi.org/10.1177/1937586715592650

Miyake-Stoner, S. J., Miller, A. M., Hammill, J. T., Peeler, J. C., Hess, K. R., Mehl, R. A., & Brewer, S. H. (2009). Probing protein folding using site-specifically encoded unnatural amino acids as FRET donors with tryptophan. *Biochemistry*, *48*(25), 5953–5962. https://doi.org/10.1021/bi900426d

Mocny, C. S., & Pecoraro, V. L. (2015). De novo protein design as a methodology for synthetic bioinorganic chemistry. *Accounts of Chemical Research*, *48*(8), 2388–2396. https://doi.org/10.1021/acs.accounts.5b00175

Munson, G. P., Lam, D. L., Outten, F. W., & O’Halloran, T. V. (2000). Identification of a Copper-Responsive Two-Component System on the Chromosome of Escherichia coli K-12. *Journal of Bacteriology*, *182*(20), 5864–5871.

Murakami, K., & Yoshino, M. (1997). Inactivation of aconitase in yeast exposed to oxidative stress. *IUBMB Life*, *41*(3), 481–486. https://doi.org/10.1080/15216549700201501

Nevitt, T., Öhrvik, H., & Thiele, D. J. (2012). Charting the travels of copper in eukaryotes from yeast to mammals. *Biochimica et Biophysica Acta (BBA) - Molecular Cell Research*, *1823*(9), 1580–1593. https://doi.org/10.1016/j.bbamcr.2012.02.011

Osborne, R. L., Zhu, H., Iavarone, A. T., Blackburn, N. J., & Kilnman, J. P. (2013). The Interdomain Long-Range Electron Transfer Becomes Rate-Limiting in the Y216A Variant of Tyramine β-Monooxygenase. *Biochemistry*, *52*(7), 1179–1191. https://doi.org/10.1021/bi3013609

Osman, D., Waldron, K. J., Denton, H., Taylor, C. M., Grant, A. J., Mastroeni, P., Robinson, N. J., & Cavet, J. S. (2010). Copper homeostasis in Salmonella is atypical and copper-CueP is a major periplasmic metal complex. *The Journal of Biological Chemistry*, *285*(33), 25259–25268. https://doi.org/10.1074/jbc.M110.145953

Outten, F. W., Outten, C. E., Hale, J., & O’Halloran, T. V. (2000). Transcriptional Activation of an *Escherichia coli* Copper Efflux Regulon by the Chromosomal MerR Homologue, CueR. *Journal of Biological Chemistry*, *275*(40), 31024–31029. https://doi.org/10.1074/jbc.M006508200

Padilla-Benavides, T., George Thompson, A. M., McEvoy, M. M., & Argüello, J. M. (2014). Mechanism of ATPase-mediated Cu $^+$ Export and Delivery to Periplasmic Chaperones: THE INTERACTION OF ESCHERICHIA COLI CopA AND CusF. *Journal of Biological Chemistry*, *289*(30), 20492–20501. https://doi.org/10.1074/jbc.M114.577668

Park, G. Y., Lee, J. Y., Himes, R. A., Thomas, G. S., Blackburn, N. J., & Karlin, K. D. (2014). Copper-peptide complex structure and reactivity when found in conserved His-X(aa)-His sequences. *Journal of the American Chemical Society*, *136*(36), 12532–12535. https://doi.org/10.1021/ja505098v

Pasquali & Floriani. (1983). Cu(I)-carbon monoxide chemistry: Recent advances and perspectives. *Recent Advances and Perspectives. In Copper Coordination Chemistry, Biochemical and Inorganic Perspectives*, pp 311−330.

Peariso, K., Huffman, D. L., Penner-Hahn, J. E., & O’Halloran, T. V. (2003). The PcoC Copper Resistance Protein Coordinates Cu(I) via Novel S-Methionine Interactions. *Journal of the American Chemical Society*, *125*(2), 342–343. https://doi.org/10.1021/ja028935y

Peña, M. M. O., Lee, J., & Thiele, D. J. (1999). A Delicate Balance: Homeostatic Control of Copper Uptake and Distribution. *The Journal of Nutrition*, *129*(7), 1251–1260. https://doi.org/10.1093/jn/129.7.1251

Petersen, C., & Møller, L. B. (2000). Control of copper homeostasis in Escherichia coli by a P-type ATPase, CopA, and a MerR-like transcriptional activator, CopR. *Gene*, *261*(2), 289–298. https://doi.org/10.1016/s0378-1119(00)00509-6

Peterson, R. L., Ginsbach, J. W., Cowley, R. E., Qayyum, M. F., Himes, R. A., Siegler, M. A., Moore, C. D., Hedman, B., Hodgson, K. O., Fukuzumi, S., Solomon, E. I., & Karlin, K. D. (2013). Stepwise protonation and electron-transfer reduction of a primary copper-dioxygen adduct. *Journal of the American Chemical Society*, *135*(44), 16454–16467. https://doi.org/10.1021/ja4065377

Peterson, R. L., Himes, R. A., Kotani, H., Suenobu, T., Tian, L., Siegler, M. A., Solomon, E. I., Fukuzumi, S., & Karlin, K. D. (2011). Cupric superoxo-mediated intermolecular C-H activation chemistry. *Journal of the American Chemical Society*, *133*(6), 1702–1705. https://doi.org/10.1021/ja110466q

Pike, R. D. (2012). Structure and Bonding in Copper(I) Carbonyl and Cyanide Complexes. *Organometallics*, *31*(22), 7647–7660. https://doi.org/10.1021/om3004459

Prigge, S. T., Kolhekar, A. S., Eipper, B. A., Mains, R. E., & Amzel, L. M. (1997). Amidation of bioactive peptides: The structure of peptidylglycine alpha-hydroxylating monooxygenase. *Science (New York, N.Y.)*, *278*(5341), 1300–1305. https://doi.org/10.1126/science.278.5341.1300

Prigge, S. T., Kolhekar, A. S., Eipper, B. A., Mains, R. E., & Amzel, L. M. (1999). Substrate-mediated electron transfer in peptidylglycine alpha-hydroxylating monooxygenase. *Nature Structural Biology*, *6*(10), 976–983. https://doi.org/10.1038/13351

Prigge, S. T., Mains, R. E., Eipper, B. A., & Amzel, L. M. (2000). New insights into copper monooxygenases and peptide amidation: Structure, mechanism and function. *Cellular and Molecular Life Sciences: CMLS*, *57*(8–9), 1236–1259. https://doi.org/10.1007/pl00000763

Prigge, Sean T., Eipper, B. A., Mains, R. E., & Amzel, L. M. (2004). Dioxygen binds end-on to mononuclear copper in a precatalytic enzyme complex. *Science (New York, N.Y.)*, *304*(5672), 864–867. https://doi.org/10.1126/science.1094583

Prohaska, J. R., & Lukasewycz, O. A. (1990). Effects of Copper Deficiency on the Immune System. In A. Bendich, M. Phillips, & R. P. Tengerdy (Eds.), *Antioxidant Nutrients and Immune Functions* (pp. 123–143). Springer US. https://doi.org/10.1007/978-1-4613-0553-8_11

Quist, D. A., Diaz, D. E., Liu, J. J., & Karlin, K. D. (2017). Activation of dioxygen by copper metalloproteins and insights from model complexes. *Journal of Biological Inorganic Chemistry: JBIC: A Publication of the Society of Biological Inorganic Chemistry*, *22*(2–3), 253–288. https://doi.org/10.1007/s00775-016-1415-2

Rensing, C., Fan, B., Sharma, R., Mitra, B., & Rosen, B. P. (2000). CopA: An Escherichia coli Cu(I)-translocating P-type ATPase. *Proceedings of the National Academy of Sciences of the United States of America*, *97*(2), 652–656.

Ross, M. O., Fisher, O. S., Morgada, M. N., Krzyaniak, M. D., Wasielewski, M. R., Vila, A. J., Hoffman, B. M., & Rosenzweig, A. C. (2019). Formation and Electronic Structure of an Atypical CuA Site. *Journal of the American Chemical Society*, *141*(11), 4678–4686. https://doi.org/10.1021/jacs.8b13610

Ross, M. O., & Rosenzweig, A. C. (2017). A tale of two methane monooxygenases. *Journal of Biological Inorganic Chemistry: JBIC: A Publication of the Society of Biological Inorganic Chemistry*, *22*(2–3), 307–319. https://doi.org/10.1007/s00775-016-1419-y

Rouch, D. A., & Brown, N. L. (1997). Copper-inducible transcriptional regulation at two promoters in the Escherichia coli copper resistance determinant pco. *Microbiology, 143*(4), 1191–1202. https://doi.org/10.1099/00221287-143-4-1191

Rubino, J. T., Riggs-Gelasco, P., & Franz, K. J. (2010). Methionine motifs of copper transport proteins provide general and flexible thioether-only binding sites for Cu(I) and Ag(I). *Journal of Biological Inorganic Chemistry: JBIC: A Publication of the Society of Biological Inorganic Chemistry*, *15*(7), 1033–1049. https://doi.org/10.1007/s00775-010-0663-9

Santiago, A. G., Chen, T.-Y., Genova, L. A., Jung, W., George Thompson, A. M., McEvoy, M. M., & Chen, P. (2017). Adaptor protein mediates dynamic pump assembly for bacterial metal efflux. *Proceedings of the National Academy of Sciences of the United States of America*, *114*(26), 6694–6699. https://doi.org/10.1073/pnas.1704729114

Sanyal, I., Karlin, K. D., Strange, R. W., & Blackburn, N. J. (1993). Chemistry and structural studies on the dioxygen-binding copper-1,2-dimethylimidazole system. *Journal of the American Chemical Society*, *115*(24), 11259–11270. https://doi.org/10.1021/ja00077a027

Schatz, M., Raab, V., Foxon, S. P., Brehm, G., Schneider, S., Reiher, M., Holthausen, M. C., Sundermeyer, J., & Schindler, S. (2004). Combined spectroscopic and theoretical evidence for a persistent end-on copper superoxo complex. *Angewandte Chemie (International Ed. in English)*, *43*(33), 4360–4363. https://doi.org/10.1002/anie.200454125

Schnepf, R., Haehnel, W., Wieghardt, K., & Hildebrandt, P. (2004). Spectroscopic identification of different types of copper centers generated in synthetic four-helix bundle proteins. *Journal of the American Chemical Society*, *126*(44), 14389–14399. https://doi.org/10.1021/ja0484294

Schultz, K. C., Supekova, L., Ryu, Y., Xie, J., Perera, R., & Schultz, P. G. (2006). A genetically encoded infrared probe. *Journal of the American Chemical Society*, *128*(43), 13984–13985. https://doi.org/10.1021/ja0636690

Siebert, X., Eipper, B. A., Mains, R. E., Prigge, S. T., Blackburn, N. J., & Amzel, L. M. (2005). The catalytic copper of peptidylglycine alpha-hydroxylating monooxygenase also plays a critical structural role. *Biophysical Journal*, *89*(5), 3312–3319. https://doi.org/10.1529/biophysj.105.066100

Solomon, E. I., Sundaram, U. M., & Machonkin, T. E. (1996). Multicopper Oxidases and Oxygenases. *Chemical Reviews*, *96*(7), 2563–2606. https://doi.org/10.1021/cr950046o

Solomon, E. I., Tuczek, F., Root, D. E., & Brown, C. A. (1994). Spectroscopy of Binuclear Dioxygen Complexes. *Chemical Reviews*, *94*(3), 827–856. https://doi.org/10.1021/cr00027a013

Sorrell, T. N., & Borovik, A. S. (n.d.). *Luminescence behavior of copper(I)-imidazole complexes. A spectroscopic model for the carbonyl derivative of hemocyanin*. 3.

Sorrell, T. N., & Borovik, A. S. (1987). Absorption, emission, and photophysical properties of copper(I) pyrazole complexes and their carbonyl adducts. *Inorganic Chemistry*, *26*(12), 1957–1964. https://doi.org/10.1021/ic00259a029

Stadtman, E. R., & Levine, R. L. (2003). Free radical-mediated oxidation of free amino acids and amino acid residues in proteins. *Amino Acids*, *25*(3–4), 207–218. https://doi.org/10.1007/s00726-003-0011-2

Stewart, E. J., Aslund, F., & Beckwith, J. (1998). Disulfide bond formation in the Escherichia coli cytoplasm: An in vivo role reversal for the thioredoxins. *The EMBO Journal*, *17*(19), 5543–5550. https://doi.org/10.1093/emboj/17.19.5543

Stohs, S. J., & Bagchi, D. (1995). Oxidative mechanisms in the toxicity of metal ions. *Free Radical Biology & Medicine*, *18*(2), 321–336. https://doi.org/10.1016/0891-5849(94)00159-h

Stoll, S., & Schweiger, A. (2006). EasySpin, a comprehensive software package for spectral simulation and analysis in EPR. *Journal of Magnetic Resonance (San Diego, Calif.: 1997)*, *178*(1), 42–55. https://doi.org/10.1016/j.jmr.2005.08.013

Su, C.-C., Long, F., & Yu, E. W. (2011). The Cus efflux system removes toxic ions via a methionine shuttle. *Protein Science: A Publication of the Protein Society*, *20*(1), 6–18. https://doi.org/10.1002/pro.532

Su, C.-C., Long, F., Zimmermann, M. T., Rajashankar, K. R., Jernigan, R. L., & Yu, E. W. (2011). Crystal structure of the CusBA heavy-metal efflux complex of Escherichia coli. *Nature*, *470*(7335), 558–562. https://doi.org/10.1038/nature09743

Sullivan, J. L., & Ochs, H. D. (1978). COPPER DEFICIENCY AND THE IMMUNE SYSTEM. *The Lancet*, *312*(8091), 686. https://doi.org/10.1016/S0140-6736(78)92806-4

Suydam, I. T., & Boxer, S. G. (2003). Vibrational Stark Effects Calibrate the Sensitivity of Vibrational Probes for Electric Fields in Proteins. *Biochemistry*, *42*(41), 12050–12055. https://doi.org/10.1021/bi0352926

Symmons, M. F., Bokma, E., Koronakis, E., Hughes, C., & Koronakis, V. (2009). The assembled structure of a complete tripartite bacterial multidrug efflux pump. *Proceedings of the National Academy of Sciences of the United States of America*, *106*(17), 7173–7178. https://doi.org/10.1073/pnas.0900693106

Tano, T., Okubo, Y., Kunishita, A., Kubo, M., Sugimoto, H., Fujieda, N., Ogura, T., & Itoh, S. (2013). Redox properties of a mononuclear copper(II)-superoxide complex. *Inorganic Chemistry*, *52*(18), 10431–10437. https://doi.org/10.1021/ic401261z

Tegoni, M., Yu, F., Bersellini, M., Penner-Hahn, J. E., & Pecoraro, V. L. (2012). Designing a functional type 2 copper center that has nitrite reductase activity within α-helical coiled coils. *Proceedings of the National Academy of Sciences of the United States of America*, *109*(52), 21234–21239. https://doi.org/10.1073/pnas.1212893110

Tetaz, T. J., & Luke, R. K. (1983). Plasmid-controlled resistance to copper in Escherichia coli. *Journal of Bacteriology*, *154*(3), 1263–1268.

Tucker, M. J., Getahun, Z., Nanda, V., DeGrado, W. F., & Gai, F. (2004). A New Method for Determining the Local Environment and Orientation of Individual Side Chains of Membrane-Binding Peptides. *Journal of the American Chemical Society*, *126*(16), 5078–5079. https://doi.org/10.1021/ja032015d

Ucisik, M. N., Chakravorty, D. K., & Merz, K. M. (2013). Structure and Dynamics of the N-Terminal Domain of the Cu(I) Binding Protein CusB. *Biochemistry*, *52*(39), 6911–6923. https://doi.org/10.1021/bi400606b

Ucisik, M. N., Chakravorty, D. K., & Merz, K. M. (2015). Models for the Metal Transfer Complex of the N-Terminal Region of CusB and CusF. *Biochemistry*, *54*(27), 4226–4235. https://doi.org/10.1021/acs.biochem.5b00195

Vendelboe, T. V., Harris, P., Zhao, Y., Walter, T. S., Harlos, K., El Omari, K., & Christensen, H. E. M. (2016). The crystal structure of human dopamine β-hydroxylase at 2.9 Å resolution. *Science Advances*, *2*(4). https://doi.org/10.1126/sciadv.1500980

Wagner, D., Maser, J., Lai, B., Cai, Z., Barry, C. E., Höner Zu Bentrup, K., Russell, D. G., & Bermudez, L. E. (2005). Elemental analysis of Mycobacterium avium-, Mycobacterium tuberculosis-, and Mycobacterium smegmatis-containing phagosomes indicates pathogen-induced microenvironments within the host cell's endosomal system. *Journal of Immunology (Baltimore, Md.: 1950)*, *174*(3), 1491–1500. https://doi.org/10.4049/jimmunol.174.3.1491

Waldron, K. J., & Robinson, N. J. (2009). How do bacterial cells ensure that metalloproteins get the correct metal? *Nature Reviews. Microbiology*, *7*(1), 25–35. https://doi.org/10.1038/nrmicro2057

Walton, P. H., & Davies, G. J. (2016). On the catalytic mechanisms of lytic polysaccharide monooxygenases. *Current Opinion in Chemical Biology*, *31*, 195–207. https://doi.org/10.1016/j.cbpa.2016.04.001

Wang, H. C., Riahi, M., Pothen, J., Bayse, C. A., Riggs-Gelasco, P., & Brumaghim, J. L. (2011). Interactions of Cu(I) with Selenium-Containing Amino Acids Determined by NMR, XAS, and DFT Studies. *Inorganic Chemistry*, *50*(21), 10893–10900. https://doi.org/10.1021/ic201440j

Wang, L., & Schultz, P. G. (2005). Expanding the Genetic Code. *Angewandte Chemie International Edition*, *44*(1), 34–66. https://doi.org/10.1002/anie.200460627

Wang, L., Xie, J., & Schultz, P. G. (2006). Expanding the genetic code. *Annual Review of Biophysics and Biomolecular Structure*, *35*, 225–249. https://doi.org/10.1146/annurev.biophys.35.101105.121507

White, C., Lee, J., Kambe, T., Fritsche, K., & Petris, M. J. (2009). A Role for the ATP7A Copper-transporting ATPase in Macrophage Bactericidal Activity. *The Journal of Biological Chemistry*, *284*(49), 33949–33956. https://doi.org/10.1074/jbc.M109.070201

Williams, P. A., Blackburn, N. J., Sanders, D., Bellamy, H., Stura, E. A., Fee, J. A., & McRee, D. E. (1999). The CuA domain of Thermus thermophilus ba3-type cytochrome c oxidase at 1.6 A resolution. *Nature Structural Biology*, *6*(6), 509–516. https://doi.org/10.1038/9274

Woertink, J. S., Tian, L., Maiti, D., Lucas, H. R., Himes, R. A., Karlin, K. D., Neese, F., Würtele, C., Holthausen, M. C., Bill, E., Sundermeyer, J., Schindler, S., & Solomon, E. I. (2010). Spectroscopic and computational studies of an end-on bound superoxo-Cu(II) complex: Geometric and electronic factors that determine the ground state. *Inorganic Chemistry*, *49*(20), 9450–9459. https://doi.org/10.1021/ic101138u

Xiao, Z., Brose, J., Schimo, S., Ackland, S. M., La Fontaine, S., & Wedd, A. G. (2011). Unification of the copper(I) binding affinities of the metallo-chaperones Atx1, Atox1, and related proteins: Detection probes and affinity standards. *The Journal of Biological Chemistry*, *286*(13), 11047–11055. https://doi.org/10.1074/jbc.M110.213074

Xue, Y., Davis, A. V., Balakrishnan, G., Stasser, J. P., Staehlin, B. M., Focia, P., Spiro, T. G., Penner-Hahn, J. E., & O'Halloran, T. V. (2008). Cu(I) recognition via cation-pi and methionine interactions in CusF. *Nature Chemical Biology*, *4*(2), 107–109. https://doi.org/10.1038/nchembio.2007.57

Yeung, N., Lin, Y.-W., Gao, Y.-G., Zhao, X., Russell, B. S., Lei, L., Miner, K. D., Robinson, H., & Lu, Y. (2009). Rational design of a structural and functional nitric oxide reductase. *Nature*, *462*(7276), 1079–1082. https://doi.org/10.1038/nature08620

Zanni, G., & Bertini, E. (2018). Chapter 11—X-linked ataxias. In M. Manto & T. A. G. M. Huisman (Eds.), *Handbook of Clinical Neurology* (Vol. 155, pp. 175–189). Elsevier. https://doi.org/10.1016/B978-0-444-64189-2.00011-1

BIOGRAPHICAL SKETCH

Katherine Brannen Alwan was born on September 26, 1992, in Sudbury, Massachusetts. In 2014 she received a B. A. degree in Molecular Biology from Skidmore College, in Saratoga Springs, NY. In the fall of 2014, she graduated with her M.S. degree from the Institute of Environmental Health within the School of Medicine at Oregon Health and Science University. In 2016 she continued her graduate education pursueing a Ph.D. in the Blackburn Lab at Oregon Health and Science University.

Publications:

Grasso, M., Bond, GJ., Kim, Y., Alwan, KB., Boyd, S., Dzebo, MM, Valenzuela, S, Tsang, T., Schibrowsky, NA., Burslem, GM., Wittung-Stafshede, P., Winkler, DD., Blackburn, NJ., Marmorstein, R., and Brady, CD. "Structural and molecular determinants of CCS-mediated copper activation of MEK1/2." Nature Chemical Biology. Submitted. (2020)

Alwan, KB., Welch, EF., Blackburn, NJ. Catalytic M Center of Copper Monooxygenases Probed by Rational Design. Effects of Selenomethionine and Histidine Substitution on Structure and Reactivity." Biochemistry 58(44), 4436-4446. (2019)

Rao, G., Pattenaude, SA., Alwan, K., Blackburn, NJ., Britt, RD. and Rauchfuss, TB.The binuclear cluster of [FeFe] hydrogenase is formed with sulfur donated by cysteine of an [Fe (Cys)(CO) 2 (CN)] organometallic precursor. PNAS, 116(42), 20850-20855. (2019)

Rao, G., Alwan KB., Blackburn, NJ., Britt, RD. Incorporation of Ni2+, Co2+ and selenocysteine into the auxiliary Fe-S cluster of the radical SAM enzyme HydG. Inorganic Chemistry. 58(19), 12601-12608. (2019)

Alwan, KB., Welch, EF., Arias, RJ., Blackburn, NJ. Rational Design of a Histidine-Methionine Site Modeling the M-center of Copper Monooxygenases in a Small Metallochaperone Scaffold. Biochemistry. 58(28), 3097-3108. (2019)

Chacón, KN., Perkins, J., Mathe, Z., Alwan, K., Ho, EN., Ucisik, M., Blackburn, NJ. Trapping intermediates in metal transfer reactions of the CusCBAF export pump of Escherichia coli. Communications biology. 1(1), 192. (2018)